technische universität
dortmund

ALMA MATER STUDIORUM
UNIVERSITÀ DI BOLOGNA

Arbeit zur Erlangung des akademischen Grades
Doktor der Naturwissenschaften

Search for same-charge top-quark pair production in proton–proton collisions with the ATLAS detector

Aaron van der Graaf
geboren in Lüdinghausen

2025

AG Kröninger
Technische Universität Dortmund

und

Alma Mater Studiorum
Università di Bologna

Erstgutachter:	Prof. Dr. Kevin Kröninger
Zweitgutachter:	Prof. Dr. Angelo Carbone
Abgabedatum:	28.02.2025

Abstract

In this thesis, the search for same-charge top-quark pair production within the Standard Model Effective Field Theory (SMEFT) is presented. The analysis is performed within the ATLAS Collaboration using the proton–proton collision data collected with the ATLAS detector during Run 2 at the Large Hadron Collider. The data correspond to an integrated luminosity of $140\,\text{fb}^{-1}$ at a center-of-mass energy of $\sqrt{s} = 13\,\text{TeV}$. Same-charge top-quark pair production, which is strongly suppressed in the Standard Model, provides a rare and sensitive probe for potential physics beyond the Standard Model. Three SMEFT operators that can lead to the production of same-charge top-quark pairs are considered in this search, namely $\mathcal{O}_{tu}^{(1)}$, $\mathcal{O}_{Qu}^{(1)}$, and $\mathcal{O}_{Qu}^{(8)}$. The search is performed in the dilepton final state. Deep neural networks are employed to create regions sensitive to the different SMEFT operators and to separate signal from background. A profile likelihood is performed across all analysis regions to extract the signal strength. The fit results show good agreement with Standard Model predictions, with no significant deviations observed. Observed upper limits are set on the Wilson coefficients of the SMEFT operators at the 95 % confidence level (CL) of $|c_{tu}^{(1)}| < 0.0068$, $|c_{Qu}^{(1)}| < 0.020$, and $|c_{Qu}^{(8)}| < 0.041$ ($[\text{TeV}/\Lambda]^2$). This corresponds to an observed limit on the cross-section for the same-charge top-quark pair production of $\sigma(pp \to tt) < 1.6\,\text{fb}$ at 95 % CL. This analysis provides the most stringent constraints to date on these SMEFT operators, improving upon previous limits by a factor of approximately 10.

Zusammenfassung

In dieser Arbeit wird die Suche nach der Produktion von Top-Quark-Paaren gleicher Ladung im Rahmen der Standardmodell-Effektiven-Feldtheorie (SMEFT) vorgestellt. Die Analyse wurde innerhalb der ATLAS-Kollaboration durchgeführt, wobei Proton-Proton-Kollisionsdaten verwendet werden, die während des Run 2 des Large Hadron Colliders mit dem ATLAS-Detektor aufgezeichnet wurden. Die Daten entsprechen einer integrierten Luminosität von $140\,\text{fb}^{-1}$ bei einer Schwerpunktsenergie von $\sqrt{s} = 13\,\text{TeV}$. Die Produktion gleich geladener Top-Quark-Paare ist im Standardmodell stark unterdrückt. Daher bietet diese Suche eine seltene und zugleich sensitive Methode, nach Physik jenseits des Standardmodells zu suchen. In dieser Analyse werden drei SMEFT-Operatoren berücksichtigt, die zur Produktion gleich geladener Top-Quark-Paare beitragen können, namentlich $\mathcal{O}_{tu}^{(1)}$, $\mathcal{O}_{Qu}^{(1)}$ und $\mathcal{O}_{Qu}^{(8)}$. Die Suche erfolgt im Dilepton-Endzustand. Tiefe neuronale Netze werden eingesetzt, um Regionen zu definieren, die empfindlich auf die verschiedenen SMEFT-Operatoren reagieren, und um eine Signal-Untergrund-Trennung durchzuführen. Eine Profil-Likelihood-Analyse wird über alle Analyseregionen durchgeführt, um die Stärke des Signals zu extrahieren. Die Ergebnisse der Analyse stimmen gut mit den Vorhersagen des Standardmodells überein, ohne dass signifikante Abweichungen beobachtet wurden. Beobachtete obere Grenzen werden für die Wilson-Koeffizienten der SMEFT-Operatoren auf einem Konfidenzniveau von 95 % gesetzt: $|c_{tu}^{(1)}| < 0.0068$, $|c_{Qu}^{(1)}| < 0.020$ und $|c_{Qu}^{(8)}| < 0.041$ ($[\text{TeV}/\Lambda]^2$). Dies entspricht einer beobachteten oberen Grenze für den Wirkungsquerschnitt der Produktion gleich geladenen Top-Quark-Paaren von $\sigma(pp \to tt) < 1.6\,\text{fb}$ bei einem Konfidenzniveau von 95 %. Diese Analyse liefert die bisher strengsten Grenzen für diese SMEFT-Operatoren und verbessert frühere Grenzen um einen Faktor von etwa 10.

Contents

1 Introduction

The goal in physics is to understand and describe the fundamental principles that underlie the universe. In particular, particle physics is dedicated to studying elementary particles and the interactions among them, which together constitute all visible matter in the cosmos. The Standard Model (SM) is the most successful theory in particle physics, offering a comprehensive description of interactions among elementary particles. Developed through joint efforts of theorists and experimentalists over several decades, the SM is a relativistic quantum field theory describing electromagnetic, weak, and strong interactions. For over a decade, the SM has been probed at CERN's Large Hadron Collider (LHC), the world's largest and most powerful particle accelerator. At the LHC, precision measurements consistently show remarkable agreement with SM predictions.

However, numerous phenomena remain unexplained by the SM. For instance, the SM does not include a description of gravity, it does not explain the existence of dark matter, the baryon asymmetry in the universe, or provide a mechanism for neutrino masses. To address these gaps, researchers explore new physic theories beyond the SM (BSM). BSM theories often introduce high-mass particles not yet observed, expected to form at high energies. Given its immense success, the SM is considered a low-energy approximation of a more fundamental theory. Consequently, searches for BSM particles are an important part of the LHC physics program. The top quark plays a crucial role in BSM searches. Being the heaviest particle in the SM, the top quark is strongly connected to the Higgs sector as it has the largest Yukawa coupling and is expected to be sensitive to BSM physics. One approach to searching for BSM particles is to assume a certain BSM theory, such as Supersymmetry, and simulate a specific process within that model. Another common approach is to use the framework of SM Effective Field Theory (SMEFT) to search for new physics indirectly, by interpreting deviations from the SM predictions. SMEFT provides a systematic, model-independent approach to parameterize potential new physics effects by extending the SM Lagrangian with higher-dimensional operators. These operators effectively introduce or modify interaction vertices, without assuming a specific BSM theory. As a result, SMEFT operators can give rise to processes that are highly suppressed or entirely forbidden in the Standard Model, as well as alter existing Standard Model processes.

This thesis presents a search for same-charge top-quark pair production using the ATLAS detector. The analysis exploits data collected during Run 2 of the LHC (2015-2018) at a center-of-mass energy of $\sqrt{s} = 13\,\text{TeV}$, corresponding to an integrated luminosity of $140\,\text{fb}^{-1}$. Since the production of same-charge top-quark pairs is highly suppressed in the SM, an observation would constitute a clear indication of BSM physics. The same-charge top-pair production can be described in the

SMEFT framework. Several SM processes can mimic the signature of the same-charge top-quark pairs due to detector effects or misreconstruction of physics objects. Consequently, a detailed understanding of the SM background processes is crucial in order to be sensitive to the same-charge top-quark pair signal. The analysis uses a binned profile likelihood fit and makes use of mutually exclusive regions enriched in signal and background events. The expected background contributions are estimated by using Monte Carlo simulations and data-driven methods. Many sources of systematic uncertainties are considered to cover limitations, such as the limited precision of the Monte Carlo simulations or inaccuracies of the detector. Regions enriched in signal events are created using machine learning. Two sets of Deep Neural Networks (DNNs) are employed. The first set of DNNs is used to separate the same-charge top pairs that originate from different EFT operators and create separate analysis regions for them. The second set of DNNs is deployed to separate the signal from the background events in each region separately. Additionally, various regions enriched in background events are defined to control the major background processes and to validate the background estimation. The signal strength is extracted by performing the profile likelihood fit in all analysis regions. The results are interpreted in the framework of the SMEFT and are used to set upper limits on the dimension-6 operators and the cross-section for same-charge top-quark pair production. This is the first search for same-charge top-pair production within the ATLAS Collaboration using SMEFT.

This analysis was developed in close collaboration with ATLAS members from Technische Universität Dortmund, Università di Bologna, Institut de Física d'Altes Energies (IFAE), and CERN. The project began in June 2021. I joined the analysis in November 2021, and in July 2023 I began serving as the main analyzer and leader of the analysis team. My contributions include developing machine learning techniques to define regions enriched with signal, refining the overall analysis strategy, performing the statistical analysis, implementing systematic uncertainties, and reinterpreting the results using the direct EFT implementation. I also finalized the analysis for publication by performing extensive cross-checks, validating the results, contributing significantly to the writing of the paper, and leading the internal review process for the analysis team. The outcomes of this analysis were published in Reference [1].

The thesis is structured as follows: In Chapter 2, an introduction to the SM is given, with a focus on the top quark and the limitations of the SM. Chapter 3 provides an overview of SMEFT and the same-charge top-quark pair production within SMEFT. In Chapter 4, the LHC and the ATLAS detector are described. The dataset and the simulated samples used in the analysis are presented in Chapter 5. Chapter 6 describes the event reconstruction and the object identification. Chapter 7 outlines the analysis strategy, including event selection, machine learning-based signal region definition, background estimation, and likelihood fit setup. The systematic uncertainties are presented in Chapter 8. The statistical analysis and its results are presented in Chapter 9. The thesis concludes with a summary in Chapter 10.

2 Overview of the Standard Model of particle physics

The Standard Model of Particle Physics (SM) is a theory that describes all known fundamental particles and their interactions. Although the Standard Model (SM) is known to be incomplete, as it fails to fully explain several fundamental observations — such as gravity and dark matter — it has nevertheless been remarkably successful in predicting experimental measurements for decades. To this day, predictions from the Standard Model (SM) continue to be confirmed by various high-energy particle experiments worldwide. In Figure 2.1 an overview of all elementary particles described by the SM is shown.

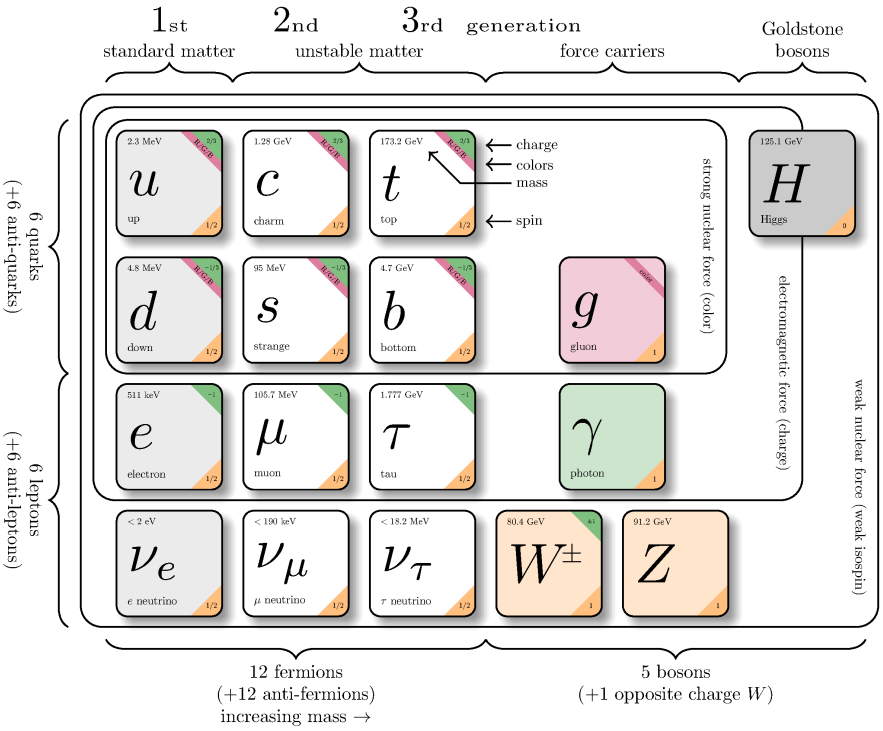

Figure 2.1: An overview of all elementary particles described by the Standard Model of Particle Physics [2]. For each particle the mass, charge, and spin is shown.

The SM is a combination of relativistic quantum theories that describe the interactions between elementary particles. It incorporates three of the four fundamental forces:

the electromagnetic, weak, and strong interactions, which are mediated by gauge bosons. The fourth fundamental force, gravity, is not included in the SM. The electromagnetic force is mediated by the photon (γ), the weak force by the $W^{\pm}$ and Z bosons, and the strong force by gluons (g). While gauge bosons mediate these forces, the Standard Model also includes other fundamental interactions, such as the Yukawa interaction, which describes how particles acquire mass through the Higgs mechanism.

The Lagrange formalism is used to describe the dynamics of particles. The Standard Model (SM) is a gauge theory, meaning it remains unchanged under local gauge transformations. The gauge group of the SM is $SU(3)_C \times SU(2)_L \times U(1)_Y$, where $SU(3)_C$ corresponds to the strong force, $SU(2)_L$ governs the weak force, and $U(1)_Y$ is associated with the electromagnetic force. Each gauge group corresponds to a symmetry that leads to a conserved quantity [3]. The $SU(3)_C$ symmetry ensures the conservation of color charge, the $SU(2)_L$ symmetry ensures the conservation of weak isospin, and the $U(1)_Y$ symmetry ensures the conservation of hypercharge Y. The interactions among all SM particles are described by the Lagrangian of the SM, which can be written as [4–6]:

$$\begin{aligned} L_{\mathrm{SM}} = & -\frac{1}{4}B_{\mu\nu}B^{\mu\nu} - \frac{1}{4}G^A_{\mu\nu}G^{A\,\mu\nu} - \frac{1}{4}W^I_{\mu\nu}W^{I\,\mu\nu} \\ & + (D_\mu\phi)^\dagger(D^\mu\phi) + \mu^2\phi^\dagger\phi - \lambda(\phi^\dagger\phi)^2 \\ & + i(\bar{u}_R \not{D} u_R + \bar{d}_R \not{D} d_R + \bar{e}_R \not{D} e_R) \\ & + i(\bar{l}_L \not{D} l_L + \bar{q}_L \not{D} q_L) \\ & - (Y^u \bar{q}_L \tilde{\phi} u_R + Y^d \bar{q}_L \phi d_R + Y^e \bar{l}_L \phi e_R + \mathrm{h.c.}). \end{aligned} \tag{2.1}$$

The field strength tensors of SM gauge group $\mathrm{SU}(3)_C \times \mathrm{SU}(2)_L \times \mathrm{U}(1)_Y$ are represented by $B_{\mu\nu}$, $W^I_{\mu\nu}$, and $G^A_{\mu\nu}$. The Higgs field is denoted by ϕ, and the covariant derivative is written as D_μ. The quark doublets of $\mathrm{SU}(2)_L$ are represented by q_L, while the lepton doublets are represented by l_L. The singlet fields for the up- and down-type quarks are denoted by u_R and d_R, respectively, and the charged lepton singlet is represented by e_R. The Yukawa couplings are encoded in the matrices Y^u, Y^d, and Y^e. In this notation, the summation over all generations of particles is implicit.

The strong interaction is described by Quantum Chromodynamics (QCD) and corresponds to the gauge group $SU(3)_C$. The gauge bosons of QCD are the gluons, which are massless and carry both a color and an anti-color charge. The structure of the $SU(3)_C$ group results in eight gluons, each with a distinct combination of color and anti-color charge. Gluons interact exclusively with particles that carry color charge, including other gluons, leading to gluon self-interactions. Quarks are fermionic, spin-1/2 particles that carry a color charge. In the SM, there are six

different quarks, divided into three generations with increasing mass. The first generation consists of the up and down quarks (u, d), the second generation consists of the charm and strange quarks (c, s), and the third generation consists of the top and bottom quarks (t, b). Each quark has an associated anti-quark with opposite quantum numbers, denoted by a bar (e.g., $\bar{u}$). Quarks are also classified into up-type (u, c, t) and down-type (d, s, b) quarks. Up-type quarks carry an electric charge of $+2/3e$, while down-type quarks carry a charge of $-1/3e$. All visible matter in the universe consists of color-neutral states due to a phenomenon known as *confinement*, which prevents the existence of free color-charged particles. In QCD, confinement refers to the property that quarks and gluons are permanently bound inside hadrons due to the strong force. Unlike other forces, the QCD potential grows with distance, meaning that attempting to separate a quark-antiquark pair only leads to the creation of new quark-antiquark pairs rather than isolated quarks.

The interactions among electrically charged particles are described by electromagnetic interactions within the theory of Quantum Electrodynamics (QED). The mediator boson of the electromagnetic force is the massless photon γ. In addition to the quarks, there are three generations of leptons in the SM: (e, ν_e), (μ, ν_μ), and (τ, ν_τ). Like the quarks, leptons are fermions, and their generations are ordered by their masses, starting with the lightest charged lepton, the electron e, followed by the muon μ, and ending with the tau lepton τ. In the SM, the three generations of neutrinos ν are assumed to be massless. The massive leptons (e, μ, τ) carry an electric charge of $-e$, while neutrinos ν are electrically neutral. As for the quarks, each lepton has an associated anti-lepton with opposite quantum numbers. Together, quarks and leptons constitute the fermionic sector of the Standard Model.

The weak interaction is mediated by the charged $W^\pm$ bosons and the electrically neutral Z boson. The $W^\pm$ bosons interact only with particles that carry a weak isospin. A particle's weak isospin depends on its chirality: left-handed fermions and right-handed antifermions have a weak isospin of $\pm\frac{1}{2}$, while right-handed fermions and left-handed antifermions have a weak isospin of zero. As a result, $W^\pm$ bosons interact exclusively with left-handed fermions and right-handed antifermions. In contrast, the neutral Z boson does not have this restriction and interacts with both left- and right-handed particles. Unlike the other fundamental interactions, the weak interaction allows parity to be violated and enables quark flavors to change via the CKM matrix [7, 8]. Additionally, due to the coupling of the weak interaction mediators varying with chirality, mass terms in the Lagrangian are forbidden, as they would violate the $\mathrm{SU}(2)_L$ symmetry of the weak interaction.

The solution to these shortcomings was introduced by the Brout-Englert-Higgs mechanism [9, 10], which postulates the Spontaneous Symmetry Breaking (SSB) of the $\mathrm{SU}(2)_L \times \mathrm{U}(1)_Y$ symmetry. SSB explains how the three massive gauge bosons Z, W^+, and W^- acquire their masses while preserving local gauge invariance. Furthermore, the electromagnetic and weak interactions are unified into the electroweak (EW)

interaction. The Higgs mechanism also introduces a new massive scalar particle with spin zero into the SM: the Higgs boson H. The Higgs boson links the Higgs field ϕ to the massive fermions through Yukawa couplings. The Yukawa coupling for each massive fermion determines its mass. However, these couplings are free parameters in the SM and must be determined experimentally. The Brout-Englert-Higgs mechanism was confirmed in 2012 with the discovery of the Higgs boson [11, 12], completing the Standard Model.

2.1 Top Quark properties and production

The top quark t was first observed in 1995 by the CDF and D0 experiments [13, 14]. Its discovery completed the quark family and revealed the most massive elementary particle in the SM. Since then, the top quark has been studied extensively, with its properties measured to high precision. As of today, the top quark has a measured mass of $m_t = (172.69 \pm 0.30)\,\text{GeV}$ [15], making it approximately 35 times heavier than the next heaviest quark, the bottom quark b. Due to its high mass, the top quark has an extremely short lifetime of $\tau = 3.29^{+0.90}_{-0.63} \cdot 10^{-25}\,\text{s}$ [15]. The extremely short lifetime of the top quark makes the formation of stable bound states highly unlikely, as it typically decays before hadronization can occur. However, recent measurements have provided initial indications of bound top-quark states, such as toponium [16], suggesting that such states might be possible under certain conditions. Nevertheless, no published observation of toponium exists to date. The top quark decays almost exclusively into a W boson and a b quark. Since it decays via the weak interaction, there is a possibility of quark flavor change according to the CKM matrix.

Although the top quark has been extensively studied in the past, it remains important to measure its properties with high precision due to its unique characteristics. As the heaviest known elementary particle, the top quark has the largest Yukawa coupling, approximately 1, making it strongly linked to the Higgs sector and EW symmetry breaking. Hence, the top quark is highly sensitive to various free parameters in the SM. Therefore, precision measurements of the top quark are used to validate and test the predictions of the SM, while any observed deviations could provide insights into physics beyond the Standard Model (BSM). This makes the top quark a very interesting candidate in today's high-energy physics research.

In proton–proton (pp) collisions at the LHC, top quarks are predominantly produced in top-quark pairs ($t\bar{t}$) via the strong interaction through gluon-gluon fusion. Single top-quark production is also possible via the weak interaction but contributes significantly less to the total number of top quarks produced at the LHC. The corresponding leading order feynman diagrams are shown in Figure 2.2a and Figure 2.2b, respectively. In Figure 2.3 the different top-quark related production cross-section measurements are shown, compared to the corresponding theoretical expectations [17].

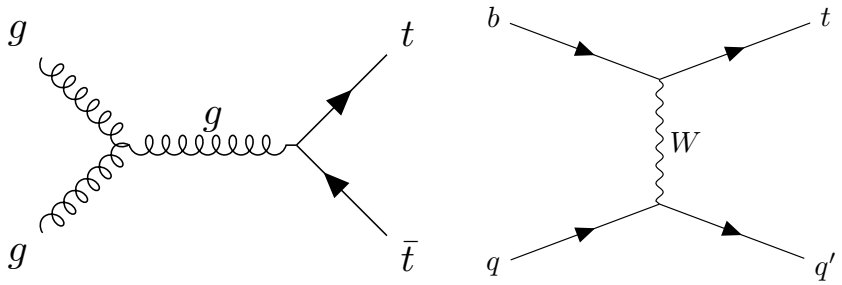

(a) **(b)**

Figure 2.2: Leading order feynman diagrams for $t\bar{t}$ production via gluon-gluon fusion (a) and single top-quark production in the t-channel (b) via the weak interaction.

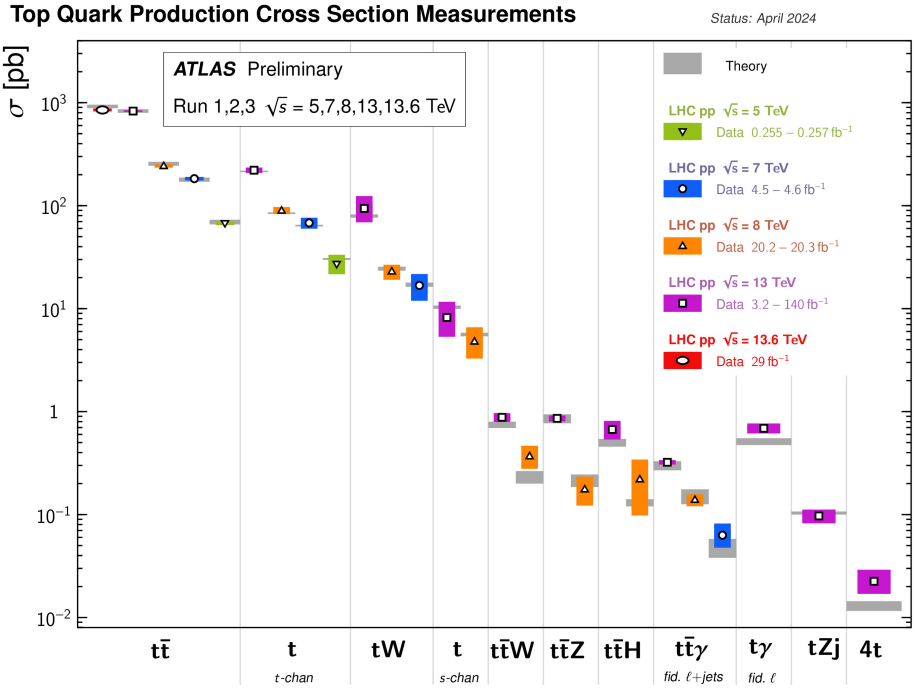

Figure 2.3: Summary of several top-quark related production cross-section measurements, compared to the corresponding theoretical expectations. All theoretical expectations were calculated at next-to-leading order or higher [17].

In this analysis, a search for same-charge top-pair production ($tt/\bar{t}\bar{t}$) is performed. According to the SM, same-charge top-pair production is not expected to occur at measurable levels at the LHC, as it is heavily suppressed by the GIM mechanism [18].

However, several BSM theories predict the production of same-charge top pairs, so an observation of this process would provide clear evidence of new physics. The production of same-sign top pairs is discussed in detail in Section 3.1.

2.2 Motivation to search for physics beyond the Standard Model

Despite the success of the SM in predicting experimental observations and providing a theoretical framework for elementary particles and their interactions, there are many reasons to believe that the SM is not the final theory of particle physics. Various fundamental observations are not properly explained by the SM, highlighting its limitations. Several significant unexplained phenomena, which motivate the search for BSM physics, are discussed in the following.

The observed asymmetry between matter and antimatter [19] in the universe remains one of the most fundamental questions not addressed by the SM. The existence of a universe dominated by baryonic matter, with negligible antimatter, suggests that many criteria must be fulfilled [20]. These include violations of baryon number symmetry, charge symmetry (C), and charge-parity symmetry (CP). While the SM incorporates CP-violating processes in weak interactions, their magnitude is insufficient to explain the observed imbalance [15]. To explain the large matter-antimatter asymmetry, extensions to the SM propose additional sources of CP violation [21]. These BSM theories seek to uncover mechanisms capable of generating the observed asymmetry, and are a key focus of research in both particle physics and cosmology.

Dark Matter (DM) [22] is a non-luminous form of matter whose existence is supported by various cosmological and astrophysical observations, such as the dynamics of rotation velocities in spiral galaxies and gravitational lensing phenomena [23]. It is estimated to make up approximately 85 % [15] of the total matter content of the universe. Unlike ordinary matter, DM does not interact through electromagnetic forces, making it invisible to traditional observational methods. Within the SM, no known elementary particle can account for the properties of DM, including its non-luminous and weakly interacting nature. As a result, theories beyond the SM propose new DM particle candidates with diverse properties that could be observed in experiments at particle accelerators. These theoretical developments aim to address the limitations of the SM in explaining this elusive component of the universe.

In the SM, neutrinos are predicted to be massless; however, neutrino oscillation experiments have confirmed that neutrinos possess non-zero masses [15]. Neutrino oscillation describes the phenomenon that neutrinos can change their flavor as they propagate through space. The observation of neutrino oscillations has led to the

development of new physics models, such as the seesaw mechanism [24], which provides a theory for the smallness of neutrino masses and the observed mixing patterns. The discovery of neutrino masses has opened a new area of research in particle physics and has motivated the search for new phenomena to explain the unique properties of neutrinos.

While the experimental evidence mentioned above provides strong motivation to search for BSM physics, the SM also has several theoretical shortcomings. One such shortcoming is the large number of free parameters in the EW sector, particularly the Yukawa couplings to the fermions. The masses of the fermions follow a hierarchical structure determined by their Yukawa couplings, spanning a wide range of values. However, the origin of this structure remains unknown. Another significant issue is the vast disparity between the weak scale, characterized by the Higgs boson mass of approximately 125 GeV, and the Planck scale, which is on the order of 10^{19} GeV. The Higgs boson mass is highly sensitive to quantum corrections from the highest energy scales, requiring finely tuned cancellations to maintain its observed low value. This unnatural fine-tuning is known as the *hierarchy problem*.

3 Standard Model Effective Field Theory

The SM can be extended in many ways in order to solve some of its theoretical and experimental shortcomings. In this analysis, the Standard Model Effective Field Theory (SMEFT) is used as a framework to study the effects of BSM physics. In SMEFT, the SM is assumed to be a low-energy approximation to a more fundamental theory, with a new-physics energy scale Λ much larger than the SM electroweak scale. The effects of new physics are parametrized by higher-dimensional operators that are suppressed by powers of Λ in SMEFT. Each operator describes a point-like interaction similar to the well-known Effective Field Theory (EFT) in Fermi's theory of weak interactions [25]. Using SMEFT allows searching for BSM physics in a model-independent way, without assuming a specific new-physics model. This has the advantage of covering a wide range of possible new-physics scenarios and provides a general framework for interpreting experimental results. As the new-physics scale Λ is assumed to be outside the experimental reach of the LHC, it is not possible to directly probe new-physics particles. Instead, the effects of BSM physics effects may be measured indirectly in the form of deviations from the SM predictions. However, new physics theories may also introduce new final states, which are suppressed or forbidden in the SM. By measuring such a new final state, it is possible to directly probe BSM physics effects. In this analysis, this approach is used to search for the production of same-charge top-quark pairs, which is highly suppressed in the SM. Therefore, an observation of same-charge top-quark pairs at the LHC would be a clear indication of new physics.

The effective Lagrangian of the SMEFT is used to expand the SM Lagrangian given in Equation 2.1. The SMEFT Lagrangian is constructed as:

$$\mathcal{L}_{\text{SMEFT}} = \mathcal{L}_{\text{SM}} + \sum_{i, D\geq 5} \frac{c_i^{(D)}}{\Lambda^{D-4}} O_i^{(D)}, \tag{3.1}$$

where each operator $O_i^{(D)}$ of mass dimension D has a corresponding Wilson Coefficient C_i (WC). The operators $O_i^{(D)}$ are built from SM fields and constructed to be invariant under the SM gauge symmetries. The WCs are dimensionless and describe the strength of the coupling for a given operator.

In the following, only SMEFT operators up to six dimensions are considered, as the effect of higher-dimensional operators is expected to be negligible due to the even stronger suppression by powers of Λ. Furthermore, lepton and baryon number

conservation is imposed in the following, leading to all potential dimension-5 operators being rejected. There are several bases for describing the complete set of dimension-6 operators, such as the Warsaw basis [26] which is used in this work. The Warsaw basis is composed of 2499 operators, all of which fulfill the requirement of lepton and baryon number conservation.

In general, EFT operators only affect very specific processes or observables. In order to propagate the effect of the operators to a specific SM process, the SM matrix element $\mathcal{M}_{\mathrm{SM}}$ is modified by adding the EFT operators. The modified matrix element $\mathcal{M}$ is given as

$$\mathcal{M} = \mathcal{M}_{\mathrm{SM}} + \frac{1}{\Lambda^2} \sum_i C_i \mathcal{M}_i^{\mathrm{EFT}} + \mathcal{O}\left(\frac{1}{\Lambda^4}\right), \tag{3.2}$$

where the terms of the order Λ^{-4}, which arise from multiple operators' insertion, are not considered. The matrix element extension $\mathcal{M}_i^{\mathrm{EFT}}$ contains the modified couplings that originate from a given operator O_i. The cross-section σ or any other observable for a given process is then calculated by squaring the matrix element. The cross-section is then given in Equation 3.3.

$$\sigma = \sigma^{\mathrm{SM}} + \frac{1}{\Lambda^2} \sum_i c_i \sigma_i^{\mathrm{int}} + \frac{1}{\Lambda^4} \sum_{i,j} c_i c_j \sigma_{i,j}^{\mathrm{EFT}} \tag{3.3}$$

The equation for the total cross-section consists of three separate contributions, as highlighted schematically in Figure 3.1.

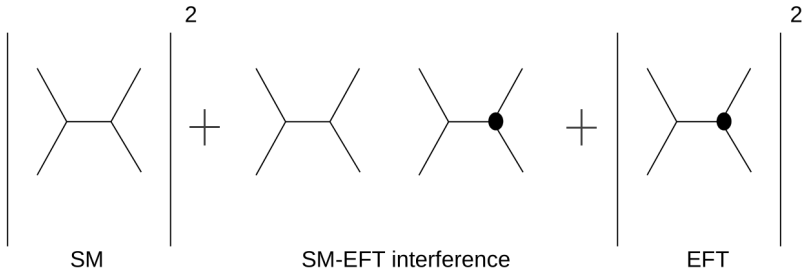

Figure 3.1: Schematic representation of the calculation of the total cross-section for any processes in the SMEFT framework, as given in Equation 3.3. The black dots present the EFT contributions in the calculation.

There is the pure SM contribution σ^{SM}, which is the cross-section calculated using the SM matrix element. The other two contributions are the interference term σ_i^{int} and the pure EFT term $\sigma_{i,j}^{\mathrm{EFT}}$. For the SM limit $c_i \to 0$ the total cross-section reduces to the SM cross-section, as the two EFT contributions vanish. The term with σ_i^{int} originates from the interference between the SM and the EFT contributions. It should be noted that for processes that are forbidden or that are strongly suppressed

in the SM, the interference term may vanish. The term $\sigma_{i,j}^{\mathrm{EFT}}$ contains the pure EFT contribution, which originates from the squared amplitudes of the operators and from the interference between the EFT operators themselves.

3.1 Same-charge top-quark pair production in the SMEFT

In the SM, the production of same-charge top-quark pairs is forbidden at leading order (LO) in perturbation theory. However, it is possible to produce same-charge top-quark pairs at the lowest perturbation order through the exchange of two W bosons, as shown in Figure 3.2a. Hence, this production process is strongly suppressed in the SM by the GIM mechanism [18], due to the larger b quark mass. The cross-section for the same-charge top-quark pair production in proton-proton collisions at $\sqrt{s} = 13\,\mathrm{TeV}$ within the SM is calculated to be $\sigma(pp \to tt)_{SM} \simeq 4 \cdot 10^{-15}\,\mathrm{pb}$ [27]. This cross-section is too small to be detectable at the Large Hadron Collider (LHC). Therefore, the observation of this process at the LHC would imply the existence of BSM physics processes.

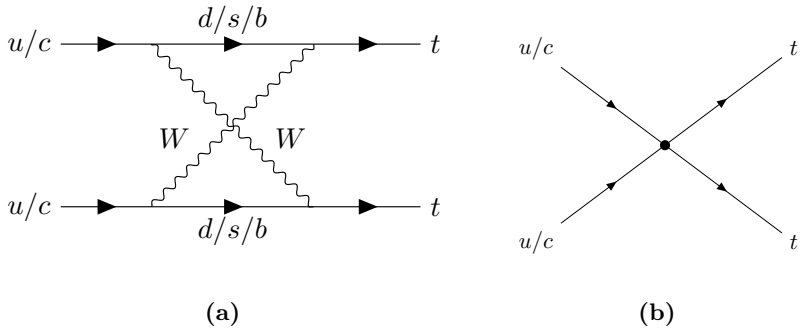

Figure 3.2: Lowest-order Feynman diagrams for same-charge top-quark pair production (a) in the SM and (b) as a point-like effective-field-theory (EFT) four-fermion interaction.

There are several BSM theories that predict the production of same-charge top-quark pairs, such as Two-Higgs-doublet models (2HDMs), Supersymmetry, or models with an extra $U(1)$ gauge group. However, instead of following one of the above-mentioned BSM models, a model-independent approach is conducted by using the SMEFT framework.

In the following, the production of same-charge top-quark pairs is described using the SMEFT framework. SMEFT introduces or modifies interaction vertices and describes them as point-like interactions. In Figure 3.2b, an example is given involving four up-type fermions with a point-like vertex. Among the all dimension-6 EFT operators expressed in the chosen Warsaw basis [26], only 15 can contribute to the production

of same-charge top-quark pairs [28]. For this thesis, a flavor universality assumption is imposed, specifically assuming universality for the initial state quark combinations uu, uc, cc. Consequently, the 15 operators are reduced to 5, by combining the different initial state quark combinations into a single operator. It should be noted that most of the sensitivity is expected to originate from the uu initial state. For the notation of the operators, the conventions of Ref. [28] are used. The five considered EFT operators are given in Equations 3.4.

$$\begin{aligned}
\mathcal{O}_{tu}^{(1)} &= [\bar{t}_{\mathrm{R}}\gamma^{\mu}u_{\mathrm{R}}][\bar{t}_{\mathrm{R}}\gamma_{\mu}u_{\mathrm{R}}] \\
\mathcal{O}_{Qq}^{(1)} &= [\overline{Q}_{\mathrm{L}}\gamma^{\mu}q_{\mathrm{L}}][\overline{Q}_{\mathrm{L}}\gamma_{\mu}q_{\mathrm{L}}] \\
\mathcal{O}_{Qq}^{(3)} &= [\overline{Q}_{\mathrm{L}}\gamma^{\mu}\sigma^{a}q_{\mathrm{L}}][\overline{Q}_{\mathrm{L}}\gamma_{\mu}\sigma^{a}q_{\mathrm{L}}] \\
\mathcal{O}_{Qu}^{(1)} &= [\overline{Q}_{\mathrm{L}}\gamma^{\mu}q_{\mathrm{L}}][\bar{t}_{\mathrm{R}}\gamma_{\mu}u_{\mathrm{R}}] \\
\mathcal{O}_{Qu}^{(8)} &= [\overline{Q}_{\mathrm{L}}\gamma^{\mu}T^{A}q_{\mathrm{L}}][\bar{t}_{\mathrm{R}}\gamma_{\mu}T^{A}u_{\mathrm{R}}]
\end{aligned} \tag{3.4}$$

Here, Q_{L} and t_{R} are the left-handed doublet and right-handed singlet of the third quark generation, q_{L} and u_{R} are related to the first two generations, and σ^a and T^A are the generators of $\mathrm{SU}(2)_{\mathrm{L}}$ and $\mathrm{SU}(3)_{\mathrm{C}}$, respectively. The operator $\mathcal{O}_{tu}^{(1)}$ describes the production of pairs of right-handed same-charge top quarks via the four-fermion interaction $u_{\mathrm{R}}u_{\mathrm{R}} \to t_{\mathrm{R}}t_{\mathrm{R}}$, where u_{R} can be either right-handed up- or charm-quark. As a consequence of assuming flavor universality, the three possible initial states uu, uc, cc are combined into a single operator. Hence, the total numbers of operators is reduced from 15 to 5. The two operators $\mathcal{O}_{Qq}^{(1)}$ and $\mathcal{O}_{Qq}^{(3)}$ describe the interaction of $u_{\mathrm{L}}u_{\mathrm{L}} \to t_{\mathrm{L}}t_{\mathrm{L}}$ and can lead to the production of a left-handed same-charge top-quark pair, with Pauli matrices σ^a entering the $\mathcal{O}_{Qq}^{(3)}$ definition. Interactions with mixed chiralities in the form of $u_{\mathrm{L}}u_{\mathrm{R}} \to t_{\mathrm{L}}t_{\mathrm{R}}$ are described by the operators $\mathcal{O}_{Qu}^{(1)}$ and $\mathcal{O}_{Qu}^{(8)}$, with the latter involving the $SU(3)_{\mathrm{C}}$ generators T^A.

All these five operators can contribute to the production of same-charge top-quark pairs. However, the operators $\mathcal{O}_{Qq}^{(1)}$ and $\mathcal{O}_{Qq}^{(3)}$ also affect B_d mixing and dijet production and were already strongly constrained by according measurements [29]. As the sensitivity of this analysis was expected to be lower than the current best constraints on these two operators, the two operators were neglected in the early phase of this analysis. Therefore, only the operators $\mathcal{O}_{tu}^{(1)}$, $\mathcal{O}_{Qu}^{(1)}$, and $\mathcal{O}_{Qu}^{(8)}$ are considered in the following. The effective Lagrangian for the production of same-charge top-quark pairs in this analysis is expressed as:

$$\mathcal{L}_{\mathrm{D=6}}^{qq\to tt} = \frac{1}{\Lambda^2}\left(c_{tu}^{(1)}\mathcal{O}_{tu}^{(1)} + c_{Qu}^{(1)}\mathcal{O}_{Qu}^{(1)} + c_{Qu}^{(8)}\mathcal{O}_{Qu}^{(8)}\right) + h.c. \tag{3.5}$$

where $c_{tu}^{(1)}$, $c_{Qu}^{(1)}$ and $c_{Qu}^{(8)}$ are the Wilson coefficients (WCs) related to the EFT operators. By following the same approach as in the Equations 3.2 and 3.3 the same-charge top-quark production Lagrangian is translated into the observable of interest, the production cross-section $\sigma(pp \to tt)$. The production cross-section is then given as

$$\sigma(pp \to tt) = \frac{1}{\Lambda^4}[(c_{tu}^{(1)})^2\sigma_{tu^{(1)}} + (c_{Qu}^{(1)})^2\sigma_{Qu^{(1)}} + (c_{Qu}^{(8)})^2\sigma_{Qu^{(8)}} + c_{Qu}^{(1)}c_{Qu}^{(8)}\sigma_{int}]. \quad (3.6)$$

It should be noted that due to the strong suppression of the production within the SM, the σ^{SM} and σ_i^{int} terms are neglected as these terms are of order $< 1 \cdot 10^{-15}$ pb. Therefore, the total cross-section is only composed of the quadratic EFT terms. Furthermore, the two interference terms between the $\mathcal{O}_{tu}^{(1)}$ operator and the $\mathcal{O}_{Qu}^{(1)}$ and $\mathcal{O}_{Qu}^{(8)}$ operators are also neglected, as no interference is expected due to their different chirality configurations. Hence, the interference term between the same chirality operators $\mathcal{O}_{Qu}^{(1)}$ and $\mathcal{O}_{Qu}^{(8)}$ is considered in the analysis.

Several other analyses have been performed to search for same-charge top-quark pair production in the past. These analyses covered a wide range of BSM models, from SUSY up to SMEFT interpretation. However, no significant excess has been observed so far. In context of the SMEFT, the best constraints on the WCs of the operators $\mathcal{O}_{tu}^{(1)}$, $\mathcal{O}_{Qu}^{(1)}$, and $\mathcal{O}_{Qu}^{(8)}$ have been set by a Run 1 analysis from the ATLAS collaboration [30]. The analysis used $20\,\mathrm{fb}^{-1}$ of pp collision data at $\sqrt{s} = 8\,\mathrm{TeV}$. It did set 95 % confidence level (CL) upper limits on $\sigma(pp \to tt)$ at 62, 51 and 38 fb for the left–left, left–right and right–right chirality of the same-charge top quarks, respectively, for the new-physics scale at $\Lambda = 1\,\mathrm{TeV}$. These cross-section limits can be translated into limits on the WCs of $|c|/\Lambda^2 < 0.053, 0.137$ and $0.042\,\mathrm{TeV}^{-2}$ [30].

3.2 SMEFT measurements in the top-quark sector

SMEFT interpretations are a very common approach to search for BSM physics in the top sector. Several SMEFT operators are sensitive to top processes, by either affecting the production or decay of top quarks. Due to the large mass, the top-quark is expected to be the most sensitive SM particle connected to BSM physics. Using the model-independent framework of SMEFT allows searching for a wide range of BSM physics scenarios, from top-flavor-changing neutral current (tFCNC) to new heavy particles. Therefore, many EFT reinterpretations of precision top quark measurements, such as mass or cross-section measurements, are carried out and used to constrain the WCs of relevant SMEFT operators. By reinterpreting already performed analyses within SMEFT, one makes use of the large number of top events

collected in the last years at the LHC to search for BSM physics with relatively small effort. Differential measurements in the top-quark sector are of special interest since they allow one to constrain several WCs at the same time, as each bin related to a kinematic distribution can be considered an observable.

In the last years, great efforts were made in attempting to constrain the whole set of EFT operators affecting top physics within one global fit. Therefore, the results of many EFT analyses performed by LHC experiments are planned to be combined. However, such an analysis introduces various challenging problems. First, the large number of EFT operators that impact the top sector complicates the analysis. In order to constrain all operators at once, many observables and various phase-space regions have to be included. Second, many analyses that are sensitive to specific operators were not designed with a SMEFT interpretation in mind and therefore do not provide the necessary information to reuse them for a global SMEFT fit analysis. To solve this shortcoming, recent analyses are often designed with a SMEFT interpretation in mind. For example, nowadays, it is common practice within the top group of the ATLAS Collaboration to publish the full likelihood information, which allows for reusing the analysis. This information is commonly published on the HEPData platform. The analysis presented in this thesis is also published on HEPData including the full likelihood, so that it can be reused for future global SMEFT fits [31]. Third, the SMEFT fit is a high-dimensional problem, which requires a large amount of computational resources. Additionally, the limits from such global fits are usually weaker compared to those of individual analyses. However, the obtained limits are more general and are therefore commonly used as a reference for designing new analyses.

In April 2024, the ATLAS Collaboration published several EFT summary plots within the top sector [32]. In these summary plots, many EFT analyses results from the ATLAS Collaboration and the CMS Collaboration were combined. The summary plots include most of SMEFT operators that affect the top sector, including operators that allow for tFCNC.

In 2020, a global fit in top-quark sector was published [33]. The global fit combines many measurements from both the ATLAS and the CMS Collaborations, including $t\bar{t}$, $t\bar{t}W$, $t\bar{t}Z$, single- and associated-top production measurements. All dim-6 SMEFT operators altering top physics are included in the fit. However, a flavor universality assumption is made in order to reduce the number of parameters. Specifically, a $U(2)_q \times U(2)_u \times U(2)_d$ flavor symmetry among quarks of the first and second generations is imposed. This flavor symmetry is motivated by the fact that top-quark observables at the LHC are largely blind to the flavor of light quarks with the same quantum numbers. Additionally, only CP-conserving extensions of the SM are considered. Lastly, operators that barely affect the top sector or that are strongly constrained by other non-top measurements are neglected. Using all these restrictions, the global fit ends up considering 22 independent SMEFT operators,

defined within the Warsaw basis. More information on the definition, notation, and relations of the operators is given in Ref. [33]. The results of the global EFT fit are presented in terms of limits on the WCs of the operators, as shown in Figure 3.3.

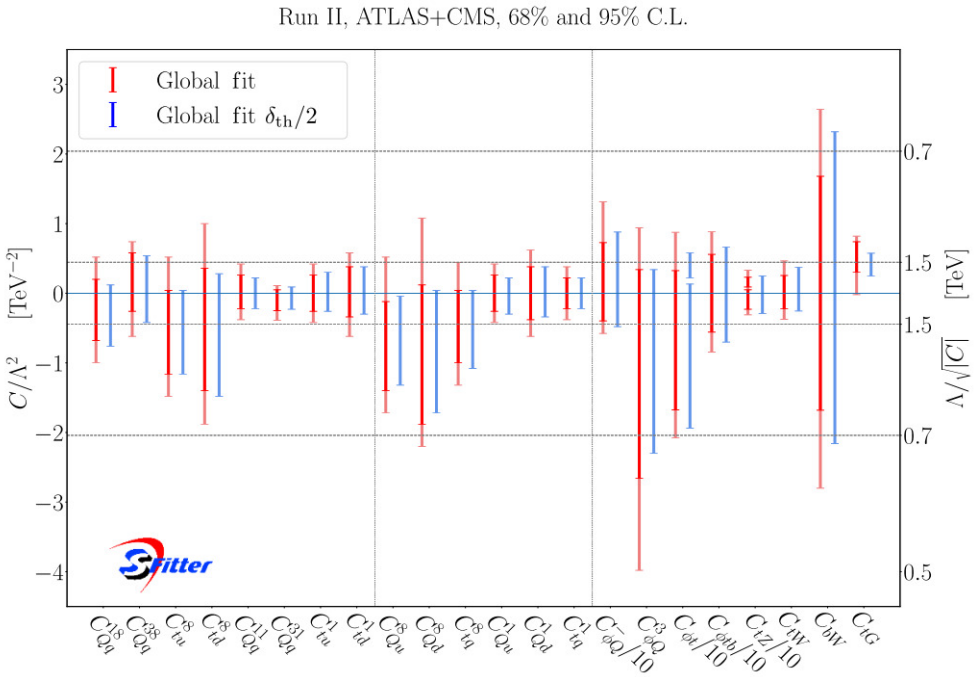

Figure 3.3: Limits on the WCs of the 22 independent SMEFT operators affecting the top sector from the global EFT fit [33].

Although this is a comprehensive result, there is still a lot of space for improvements for the future. In the upcoming years, more and more measurements will be performed at the LHC experiments with a global SMEFT fit in mind. Hence, the number of observables and phase-space regions is expected to increase, leading to a more precise and more complete global SMEFT fit, including more operators and fewer assumptions. Additionally, a global fit including other physics sectors, such as Higgs and B physics, looks very promising [34]. Including these sectors would allow constraining the WCs of the operators even further and in a more general fashion, by using the full power of the LHC data.

4 The ATLAS Detector at the Large Hadron Collider

4.1 The Large Hadron Collider

The Large Hadron Collider (LHC) [35] at the European Council for Nuclear Research (CERN) is the largest and most powerful particle accelerator in the world. The LHC is located in Geneva, Switzerland and has a circumference of 27 km and is located 100 m underground. It is designed to accelerate protons or heavy ions to very high energies, reaching up to 6.8 TeV per beam. Pre-accelerators are used to gradually increase the proton's energy from about 50 MeV after the first liner accelerator up to 450 GeV after the Super Proton Synchrotron before being injected into the LHC storage ring.

Inside the LHC, there are two tubes where the beams of protons travel in opposite directions. These beams are controlled by superconducting magnets, which guide them along the circular path. Once per turn, the beams are accelerated in superconducting cavities, either increasing their energy or keeping the particle beam at a given target energy. The LHC has four interaction points (IPs) where the beams can collide. Each IP is used by one of the four main experiments at the LHC: ATLAS, CMS, ALICE, and LHCb. The detectors for ATLAS [36] and CMS [37] are designed as multipurpose detectors, while ALICE [38] is designed to study heavy-ion collisions, and LHCb [39] is focused on studying the properties of B mesons.

The LHC began operating in 2008. During its first data-taking phase from 2009 to 2013 (Run 1), it reached center-of-mass energies of $\sqrt{s} = 7\,\text{TeV}$ and $\sqrt{s} = 8\,\text{TeV}$. Run 1 was followed by a long shutdown period, in which several upgrades were made to the accelerator and the detectors. The LHC resumed operation in 2015 and started a second data-taking phase from 2015 to 2018 (Run 2). During Run 2, the LHC reached a center-of-mass energy of $\sqrt{s} = 13\,\text{TeV}$ and a peak luminosity of $L = 2.1 \cdot 10^{34}\,\text{cm}^{-2}\,\text{s}^{-1}$ [40]. After Run 2, the LHC entered its second-long shutdown period, which was used for further upgrades. In 2022, the third data-taking phase (Run 3) started with a center-of-mass energy of $\sqrt{s} = 13.6\,\text{TeV}$ and is still ongoing. Run 3 is expected to provide an even larger dataset than Run 2.

4.2 The ATLAS Detector

The ATLAS detector [36] is a multipurpose particle detector designed to study a wide range of physics processes at the LHC. The ATLAS detector is a cylindrical detector with a forward-backward symmetrical geometry and covers nearly the full 4π solid angle around the collision point, excluding the beam pipe and the support structures of the detector. Figure 4.1 shows a sketch of the detector, measuring 46 m in length and 25 m in diameter.

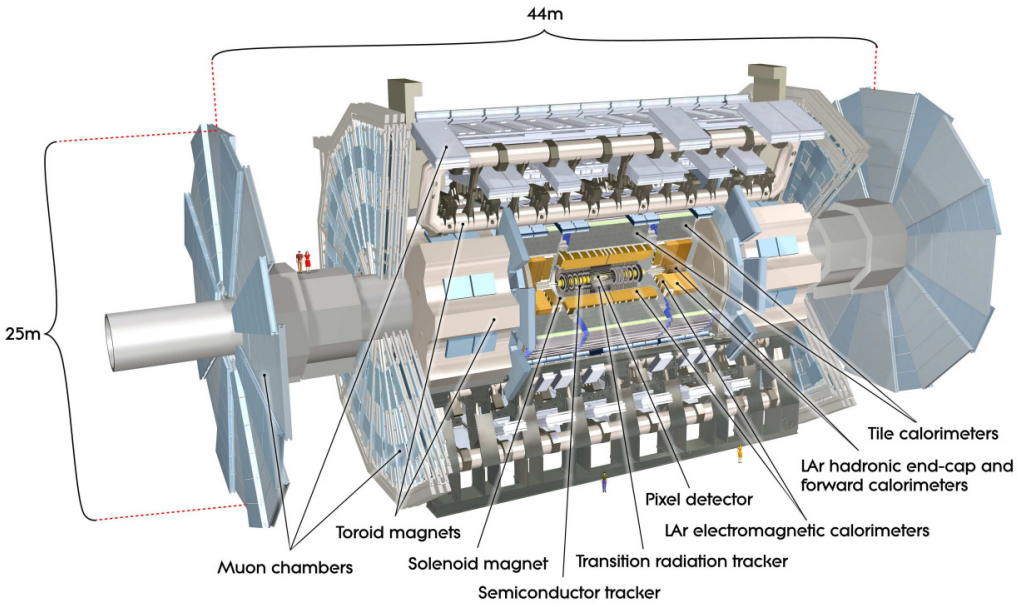

Figure 4.1: Schematic cut-away view of the ATLAS detector, showing the various sub-detectors during the Run 2 data-taking period [36].

Its geometry is described in a right-handed cylindrical coordinate system, with its origin at the center of the detector. The radial coordinate r and the azimuthal angle $\phi = [-\pi, \pi]$ define the transverse plane, where $\phi = 0$ points towards the center of the LHC ring. The pseudorapidity η is defined in terms of the polar angle θ as $\eta = -\ln\tan(\theta/2)$. Angular distances are measured in units of $\Delta R = \sqrt{(\Delta y)^2 + (\Delta\phi)^2}$ in the $\eta - \phi$ plane. The ATLAS detector is composed of several sub-detectors, each designed to measure different properties of the particles produced in the collisions. The sub-detectors are arranged in layers, starting from the innermost one to the outer ones, as described below. The given description is based on the status of the ATLAS detector during the Run 2 data-taking period, as the Run 2 data is used in this thesis. With the start of Run 3, the ATLAS detector has been further upgraded and improved [41].

The inner detector (ID) is the innermost sub-detector of the ATLAS detector and is used to measure the trajectories of charged particles. It is immersed in a 2 T axial magnetic field, which is generated by a superconducting solenoid. The magnetic field causes charged particles to curve in the transverse plane, allowing the measurement of the particle's momentum and its electric charge. The ID is composed of three sub-detectors: the pixel detector, the semiconductor tracker (SCT), and the transition radiation tracker (TRT). Each sub-detector consists of silicon sensors arranged in a cylindrical geometry around the IP. The pixel detector as the innermost sub-detector provides the highest tracking resolution in the range $|\eta| < 2.5$. For Run 2, the pixel detector was upgraded with the insertion of the insertable B-layer (IBL) [42, 43]. Its purpose is to improve tracking by providing additional measurements closer to the IP with finer granularity, allowing the measurement of track information of short-lived particles, crucial information for the flavor-tagging performance. In addition to the IBL, the pixel detector consists of three layers of pixel detectors with high granularity. The intrinsic resolution is 10 µm in the azimuthal and radial directions and 115 µm in the z (barrel) and radial directions (end-cap). Typically, four measurements are provided per track, one for each pixel detector layer. The SCT surrounds the pixel detector and is composed of four layers of silicon microstrip sensors. Each layer consists of small-angle stereo strips and tracks in the range $|\eta| < 2.5$. Five additional layers are placed as disks in each end-cap. The SCT typically provides four additional measurements per track and has a resolution of 17 µm in the transverse plane and 580 µm in the z direction and radial direction in the end-caps. The TRT is the outermost sub-detector of the ID and covers the region $|\eta| < 2$. The TRT is composed of straw tubes filled with a gas mixture to track traversing particles. Additionally, the TRT provides electron identification information based on the fraction of hits above a higher energy-deposit threshold corresponding to transition radiation.

Similar to the ID, the ATLAS calorimeter system consists of several sub-detectors. The general goal of the calorimeter system is to measure the energy of traversing particles. Alternating layers of absorber material and sensors are used to measure the energy of the particles. The absorber material causes the particles to interact and lose energy, which is then measured by the sensors. The interaction with the absorber material causes the particles to shower, producing secondary particles. This process repeats until the particles have lost all their energy. Therefore, measuring the energy of high-energy particles involves measuring the energy of all particles produced within their showers. Consequently, the measured energy of all particles allows for a precise determination of the missing transverse momentum E_T^{miss}. The precise measurement of E_T^{miss} is crucial, as neutrinos cannot be detected directly with the ATLAS detector due to their tiny interaction probability. Therefore, E_T^{miss} is used as a proxy for neutrino energy.

The calorimeter system is divided into two parts: the electromagnetic calorimeter (ECAL) and the hadronic calorimeter (HCAL). The ECAL is composed of a barrel

and two end-cap calorimeters. The interaction layers consist of lead and liquid argon (LAr), and the layers are arranged in an accordion-like shape. The ECAL covers the region $|\eta| < 3.2$ and is used to measure the energy of electrons and photons. The ECAL has finer granularity within the ID acceptance region $|\eta| < 2.5$. The energy of hadrons is measured using the HCAL, which consists of three calorimeters: the tile calorimeter (HTC), the end-cap calorimeter (HEC), and the forward calorimeter (FCal). The HTC is located outside the ECAL and consists of three barrel layers. It uses steel as the absorbing material and scintillating tiles as the active material. The HEC is made of copper plates and LAr and is arranged in two wheels on each end-cap. The FCal is placed in the forward region of the detector, covering the range $3.1 < |\eta| < 4.9$. It consists of three modules per end-cap, using liquid argon as the active material and copper or tungsten as the absorbing material.

The muon spectrometer (MS) forms the outermost part of the ATLAS detector and is specifically designed to track muons and measure their momenta, since the ID is insufficient for measuring muons due to their low interaction probability. The MS detects the bending of muon trajectories in the magnetic field created by barrel and end-cap toroid magnets. It includes two key types of chambers: high-precision tracking chambers, which monitor the bending of muons, and trigger chambers, which are responsible for identifying muons. The high-precision chambers cover the region $|\eta| < 2.7$, while the trigger chambers operate within $|\eta| < 2.4$. In the barrel region, high-precision tracking is performed using monitored drift tubes (MDTs), which achieve a resolution of about 80 µm per hit in the bending direction. These chambers are filled with a gas mixture of argon and carbon dioxide, ensuring stability over time. Each MDT provides six to eight measurements along the muon's trajectory. In the forward regions, where higher particle rates occur, cathode strip chambers (CSCs) are used instead of MDTs to cover the $|\eta|$ range from 2 to 2.7. These chambers employ multi-wire proportional designs and also utilize a mixture of argon and carbon dioxide. Each CSC simultaneously records both azimuthal (ϕ) and pseudorapidity (η) information, with resolutions of 60 µm and 5 mm , respectively. The trigger chambers include resistive plate chambers (RPCs) in the barrel, designed for rapid signal detection with a time resolution of about 2 ns. They are arranged in three concentric layers and cover $|\eta| < 1.05$. In the end-cap region ($1.05 < |\eta| < 2.4$), thin gap chambers (TGCs) are used instead. The TGCs handle high event rates and provide timing resolutions between 15 ns and 18 ns. Both RPCs and TGCs also contribute to position measurements, complementing the tracking capabilities of the MDTs and CSCs, with spatial resolutions ranging from 5 mm to 10 mm . To ensure accurate momentum measurements, the MS relies on an alignment system using optical sensors.

The high collision frequency of the LHC results in an enormous amount of data being produced by the ATLAS detector, far exceeding the direct storage rate. Hence, a trigger system is used to efficiently select and retain only the most relevant events for physics analyses. Events are selected by the first-level trigger (L1) system, followed

by the high-level trigger (HLT) [44] system. The L1 trigger primarily uses hardware-based information to process data rapidly and identify regions of interest in the detector. Information from sub-detectors such as the calorimeters and the MS is analyzed to determine whether an event is of interest for future physics analyses. This fast processing significantly reduces the event rate from the original LHC bunch crossing rate of 40 MHz to 100 kHz . The HLT refines this selection at the software level using more detailed information from the detectors, such as tracking data from the ID, fine-granularity calorimeter information, and precision muon measurements. By applying these additional requirements, the HLT further reduces the event rate to about 1 kHz, enabling events to be stored for offline analysis.

5 Data and Monte Carlo Simulation

5.1 Data

The data used in this thesis consists of the full Run 2 dataset collected by the ATLAS detector at the LHC. This dataset was acquired from proton–proton collisions between 2015 and 2018 at a center-of-mass energy of $\sqrt{s} = 13\,\text{TeV}$. It corresponds to an integrated luminosity of 140 fb^{-1}, with an uncertainty of 0.83 % [45]. Only events recorded during stable beam conditions and when all detector subsystems were operational are included in the analysis.

5.2 Monte Carlo Simulation

Monte Carlo (MC) simulations were used to model the signal and background processes in the analysis. The simulation of the MC samples was performed in three steps.

First, the processes were simulated at the parton level using matrix element (ME) calculations that determine their probabilities, accounting for the initial proton–proton collision conditions at 13 TeV as described by the parton distribution function (PDF). These calculations rely on the *factorization theorem*, which states that the cross-section of a high-energy process can be factorized into a perturbative and a non-perturbative component. The perturbative component describes the hard scattering of partons and can be computed using QCD at short distances, while the non-perturbative part encapsulates the long-distance effects, such as the proton structure, described by the PDFs. The factorization scale μ_f determines the energy threshold below which perturbative QCD is no longer applicable, requiring non-perturbative modeling. Next, the parton shower (PS) was simulated to model both the QCD radiation of partons and their hadronization into final-state particles. The parton shower accounts for additional soft and collinear QCD emissions, which are treated within *perturbative QCD*, while hadronization is governed by *non-perturbative QCD* mechanisms.

For each process, a detailed description of the employed ME generator, PDF, and PS algorithm is provided. Table 5.1 summarizes the MC samples used in this analysis along with all simulation settings.

The second step consists of simulating the detector response within the ATLAS detector using the GEANT4 package [46, 47]. For a few samples, a fast simulation of the detector was used, in which the calorimeter response was not fully simulated and instead was replaced by a parameterization of the shower shapes [48]. The fast simulation of the detector is a trade-off between the accuracy and computational cost of the simulation. It was used for the signal samples and the $t\bar{t}t\bar{t}$, tWH and $tHjb$ background samples. This step of simulating the detector response is referred to as *digitization*, as the simulated energy deposits are converted into detector signals that are read out as voltages or currents by the detector electronics. Additionally, in this step the effects of multiple collections during a single bunch crossing, referred to as pileup, are modeled by overlaying the simulated events with additional *minimum-bias* events. This is done to account for the additional proton–proton interactions that occur in the same or nearby bunch crossings as the hard-scatter interaction of interest. The used minimum-bias events were simulated using the event generator PYTHIA 8.186 [49] with the NNPDF2.3LO PDFs [50] and the A3 set of tunable parameters [51] for the PS simulation, referred to as *tune*.

In the third and last step, all simulated events are passed through the same reconstruction algorithms as the data. The description of the reconstruction algorithms is given in Section 6.

Unless otherwise specified, the MC samples share the following common settings: the masses of the top quark and the Higgs boson are set to 172.5 GeV and 125 GeV, respectively. The modeling of the decays of heavy-flavor (HF) hadrons is based on EVTGEN [52], except for samples produced with SHERPA. Events generated with MADGRAPH5_AMC@NLO [53] or POWHEG BOX [54–56] were interfaced with PYTHIA 8 [57] and used the A14 tune [58] with the NNPDF2.3LO PDF set to model the PS, underlying event (UE) and hadronization. Events interfaced with HERWIG 7 [59, 60] used the MMHT2014LO PDF set [61] and the corresponding tune provided by HERWIG, either H7.2-Default or H7-UE-MMHT. Events simulated with SHERPA [62] used the PS and hadronization model and the tune provided by the SHERPA authors.

5.2.1 Same-sign top-quark signal samples

The signal events are generated using MADGRAPH5_AMC@NLO [53] v2.9.3 together with the SMEFTSIM3.0 Feynrules package [63–65], using the m_W EW input scheme. The ME calculations are performed at leading order (LO) in QCD without the inclusion of additional jets, using the NNPDF30LO [66] PDF set. Next-to-leading order (NLO) accuracy is not supported by SMEFTSIM3.0 and was therefore omitted. As a consequence of the LO approximation, the jet multiplicity may be inaccurately modeled. To account for these higher-order effects, scale variations are applied to the jet multiplicity distribution and treated as a systematic uncertainty for the

Table 5.1: The samples used for event generation of signal and background processes. The samples used to estimate the systematic uncertainties are shown in parentheses. The production of an EW boson is denoted by V (W or Z/γ^*). The parton density function (PDF) shown in the table is the one used for the matrix element (ME). The tune is the set of tuned parameters of the parton-shower (PS) generator.

Process	Generator	ME order	PS	PDF (ME)	Tune
$tt/\overline{tt}$ EFT signal	MadGraph5	LO	Pythia 8	NNPDF3.0LO	A14
$t\bar{t}W$	Sherpa 2.2.10	NLO	Sherpa	NNPDF3.0NNLO	Sherpa default
	(MadGraph5)	(NLO)	(Pythia 8)	(NNPDF3.0NLO)	(A14)
	(Powheg Box)	(NLO)	(Pythia 8)	(NNPDF2.3LO)	(A14)
	(Powheg Box)	(NLO)	(Herwig 7.2)	(NNPDF3.0NLO)	(H7.2-Default)
$t\bar{t}Z/\gamma^*$	MadGraph5	NLO	Pythia 8	NNPDF3.0NNLO	A14
	(MadGraph5)	(NLO)	(Herwig 7.2)	(NNPDF3.0NLO)	(H7.2-Default)
	(MadGraph5)	(NLO)	(Pythia 8)	(NNPDF3.0NLO)	(A14 Var3c)
$t\bar{t}\ell\ell$	MadGraph5	NLO	Pythia 8	NNPDF3.0NLO	A14
$t\bar{t}H$	Powheg Box	NLO	Pythia 8	NNPDF3.0NLO	A14
	(Powheg Box)	(NLO)	(Herwig 7.04)	(NNPDF3.0NLO)	(H7UE-MMHT)
	(MadGraph5)	(NLO)	(Pythia 8)	(NNPDF3.0NLO)	(A14)
VV, $qqVV$, VVV	Sherpa 2.2.2	NLO	Sherpa	NNPDF3.0NNLO	Sherpa default
Four top	MadGraph5	NLO	Pythia 8	NNPDF3.1NLO	A14
$t\bar{t}$	Powheg Box	NLO	Pythia 8	NNPDF3.0NLO	A14
s-, t-channel, Wt single top	Powheg Box	NLO	Pythia 8	NNPDF3.0NLO	A14
$Z \to \ell^+\ell^-$ (Mat Conv)	Powheg Box	NLO	Pythia 8	CT10NLO	AZNLO
$Z \to \ell^+\ell^- + (\gamma*)$	Powheg Box	NLO	Pythia 8	CT10NLO	AZNLO
$Z \to \ell^+\ell^-$	Sherpa 2.2.1	NLO	Sherpa	NNPDF3.0NNLO	Sherpa default
W+jets	Sherpa 2.2.1	NLO	Sherpa	NNPDF3.0NNLO	Sherpa default
$V\gamma$	Sherpa 2.2.8	NLO	Sherpa	NNPDF3.0NNLO	Sherpa default
$t(Z/\gamma^*)$, $t\bar{t}t$, $t\bar{t}WH$	MadGraph5	LO	Pythia 8	NNPDF2.3LO	A14
$t\bar{t}W^+W^-$, $t\bar{t}ZZ$, $t\bar{t}HH$	MadGraph5	LO	Pythia 8	NNPDF2.3LO	A14
$tW(Z/\gamma^*)$, tWH, $tHqb$	MadGraph5	NLO	Pythia 8	NNPDF3.0NLO	A14
VH	Powheg Box	NLO	Pythia 8	NNPDF3.0NLO	A14

signal samples. Only the leptonic decay modes of the top quark are considered, in which the top quark decays into a W boson and a b-quark, with the W boson subsequently decaying into a charged lepton and a neutrino of the same flavor. The parton showering is simulated using Pythia 8.245 [57] with the A14 tune [58].

Only the three operators $\mathcal{O}_{tu}^{(1)}$, $\mathcal{O}_{Qu}^{(1)}$ and $\mathcal{O}_{Qu}^{(8)}$ of the five four-fermion operators that can produce same-sign top-quark pairs are considered in simulation. Furthermore, a quark flavor universality was imposed for the production of the same-sign top pairs. Consequently, the WCs for $uutt$, $uctt$, and $cctt$ vertices are bound to the same value regardless of the flavor of the quarks. More information on the SMEFT operators is given in Section 3.1.

A nominal sample was produced for tt and $\overline{tt}$, in which the WCs were set to $c_{tu}^{(1)} =$

0.04, $c_{Qu}^{(1)} = 0.1$ and $c_{Qu}^{(8)} = 0.1$. These samples correspond to cross-sections of $\sigma(pp \to tt) = 97.6\,\text{fb}$ and $\sigma(pp \to \overline{tt}) = 2.4\,\text{fb}$, assuming a new-physics scale of $\Lambda = 1\,\text{TeV}$. This highlights that the signal is highly charge-asymmetric, leading to a cross-section which is approximately 40 times larger for tt production compared to $\overline{tt}$ production. Different values are used for the three WCs in order to have similar contributions from the three operators to the total cross-section. Hence, $c_{tu}^{(1)}$ is set to a lower value, as it is the dominant operator in the production of same-charge top pairs. These nominal samples were used in the optimization of the analysis strategy and were used to generate alternative signal samples with different WC values via reweighting.

The MadGraph5_aMC@NLO reweighting tool [67, 68] is used to obtain the alternative signal predictions from the nominal sample. An event weight for a different set of WCs is obtained through the re-computation of the MEs and modifying the event weight according to the ratio of the squared nominal and recomputed MEs. The new event weight is given by

$$W_{\text{new}} = \frac{|M_{\text{new}}|^2}{|M_{\text{orig}}|^2} W_{\text{orig}} \tag{5.1}$$

where W_{orig} is the original event weight and M_{new}, M_{orig} are the re-computed and original MEs, respectively.

Following this procedure, four samples are produced for each of the three operators, while the other two operators are set to zero. For the three WCs the following values are used: $c_{tu}^{(1)} = [0.02, 0.03, 0.04, 0.05]$, $c_{Qu}^{(1)} = [0.05, 0.07, 0.10, 0.15]$, and $c_{Qu}^{(8)} = [0.1, 0.2, 0.25, 0.30]$. In addition to these 12 samples with a single WC set to a non-zero value, 20 samples are generated with two or three WCs set to non-zero values. All possible permutations of the following WC values are used for the *mixed* samples: $c_{tu}^{(1)} = [0, 0.01, 0.02]$, $c_{Qu}^{(1)} = [0, 0.05, 0.1]$, and $c_{Qu}^{(8)} = [0, 0.2, 0.3]$. Permutations where more than one WC is set to zero are not considered, leading to 20 unique *mixed* samples. Similar as for the nominal sample, the ranges of WCs for the different operators were chosen in order to balance the contribution to the total cross-section from the three operators. All 32 reweighted samples correspond to cross-sections between 10 fb and 100 fb and assumed a new-physics scale BackgroundOnlyFit $\Lambda = 1\,\text{TeV}$.

The reweighting procedure was validated by comparing reweighted samples to additional signal samples generated using the MadGraph5_aMC@NLO setup described above, employing the same WC configuration as used in the reweighted samples. For validation, the kinematic distributions of tt events were compared at the particle *truth level*, which is the stage of the simulation where final state particles are fully known and no detector simulation is applied, and at the *reconstruction level*, where the simulation of the detector response and geometry is taken into account. No

significant differences were observed between the samples at either level, confirming the validity of the reweighting procedure.

5.2.2 Background samples

SM processes such as $t\bar{t}W$, $t\bar{t}Z$, $t\bar{t}\gamma$, $t\bar{t}H$, $t\bar{t}t\bar{t}$, and other rare top processes can produce final states with two leptons of the same electric charge. These processes mimic the signal final state and are referred to as *irreducible backgrounds* in this analysis. In addition to these, other background events may mimic the searched final state signature due to detector inefficiencies or misreconstruction. These events are referred to as *reducible backgrounds*. For example, jets can be misidentified as leptons, or leptons can have their electric charge incorrectly assigned, allowing events that originally contain only one lepton or opposite-sign leptons to pass the signal selection criteria. The primary contribution to the reducible background, however, comes from events with non-prompt leptons. Non-prompt leptons do not originate from the primary vertex of the hard-scatter interaction, instead, they arise from hadron decays or from photon conversions ($\gamma/\gamma^* \to e^+e^-$). These leptons can be misreconstructed as prompt, thereby satisfying the signal selection criteria. The non-prompt lepton backgrounds are estimated using simulated samples of $t\bar{t}$, single top, and $Z \to \ell^+\ell^-$ events. The following paragraph describes the simulation setup for the various background samples, beginning with the reducible backgrounds.

The $t\bar{t}W$ production is the dominant background in the signal-dominated regions. The used simulation setup for $t\bar{t}W$ production follows the setup used in the $t\bar{t}W$ cross-section measurement in Ref. [69]. This setup provides the highest available precision within ATLAS and is based on Sherpa 2.2.10. Both the factorization and renormalization scales, μ_{F} and μ_{R}, were set to $H_T/2$, where H_T is the sum of the transverse masses $m_T = \sqrt{m^2 + p_T^2}$ of all particles generated in the ME calculation. The simulation was performed at next-to-leading order (NLO) QCD accuracy for MEs with up to one jet and leading order (LO) accuracy for up to two additional jets. Additional partons were matched and merged with the Sherpa PS using Catani–Seymour dipole factorization [70, 71] and the MEPS@NLO method [72–75] with a CKKW merging scale of 30 GeV. Virtual QCD corrections for MEs at NLO accuracy were provided by the OpenLoops 2 library [76–78]. The samples were simulated using the NNPDF3.0nnlo [66] PDF set. The LO EW contributions were obtained from a dedicated sample simulated with Sherpa 2.2.10 and were combined with the NLO QCD sample described above. The events were normalized using a cross-section of 722 fb, as calculated in Ref. [79]. Three alternative $t\bar{t}W$ samples are used to estimate systematic uncertainties and are listed in Table 5.1 (in parentheses). Further details on the use of these alternative samples for estimating systematic modeling uncertainties are provided in Section 8.2.

The production of $t\bar{t}Z/\gamma^*$ events was simulated using the MadGraph5_aMC@NLO generator. The factorization and renormalization scales, μ_{F} and μ_{R}, were set to $0.5 \times \sum_i \sqrt{m_i^2 + p_{\mathrm{T},i}^2}$, where the sum includes all particles generated in the ME calculation. The cross-sections were computed at NLO accuracy in both QCD and EW interactions using MadGraph5_aMC@NLO, as detailed in Ref. [80]. The cross-section for $t\bar{t}Z$ ($\ell\ell$) events with an off-shell Z boson, referred to as $t\bar{t}\ell\ell$, was scaled by an off-shell correction estimated at one-loop level in α_{s}. Two alternative $t\bar{t}Z/\gamma^*$ samples were simulated at NLO QCD with the MadGraph5_aMC@NLO generator and interfaced either to Pythia 8 or Herwig 7.2, which are used later on to define a proper PS and an initial-state radiation (ISR) uncertainty.

The production of $t\bar{t}H$ events was simulated using the Powheg Box v2 [54, 81–84] generator. The factorization and renormalization scales, μ_{F} and μ_{R}, were set to $\sqrt[3]{m_{\mathrm{T}}(t) \cdot m_{\mathrm{T}}(\bar{t}) \cdot m_{\mathrm{T}}(H)}$. The cross-section was calculated at NLO accuracy, as detailed in Ref. [80]. Two additional $t\bar{t}H$ samples were generated: one using the MadGraph5_aMC@NLO generator with Pythia 8 and another using the Powheg Box generator with Herwig 7.2. These alternative samples are used to estimate uncertainties for the ME generator matching and the PS.

Diboson final states (VV) were simulated using the Sherpa 2.2.2 generator with the NNPDF3.0nnlo PDF set, including off-shell effects. The MEs were calculated at NLO accuracy in QCD for up to one additional parton emission and at LO accuracy for up to three additional partons. Loop-induced processes were simulated at LO for up to one additional parton emission. The calculations were matched and merged with the Sherpa PS, which uses Catani–Seymour dipole factorization, following the MEPS@NLO approach. Virtual QCD corrections were provided by the OpenLoops library.

The production of $t\bar{t}t\bar{t}$ events was simulated using the MadGraph5_aMC@NLO generator with the NNPDF3.1nlo PDF set and interfaced with Pythia 8. Several rare processes were also included in the background estimation: tZ, VH, $t\bar{t}WW$, $t\bar{t}HH$, $t\bar{t}WH$, $t\bar{t}ZZ$, tWZ, tWH, $tHqb$, ttt, and VVV production. Processes involving at least one top quark were simulated with MadGraph5_aMC@NLO, while VVV events were generated using Sherpa 2.2.2, and VH production was simulated with Powheg Box v2.

The $t\bar{t}$ production process was simulated using Powheg Box v2 and normalized to the cross-section predicted at next-to-next-to-leading order (NNLO) in QCD. This prediction included the resummation of next-to-next-to-leading logarithmic (NNLL) soft-gluon terms, calculated with Top++ 2.0 [85–91]. The h_{damp} parameter, which regulates the transverse momentum of the first gluon emission beyond the Born configuration in Powheg Box, was set to 1.5 m_{top} [92].

The production of single top quarks together with W bosons (tW) was simulated using the POWHEG BOX v2 generator at NLO in QCD. To avoid interference and overlap with $t\bar{t}$ production, the diagram-removal method [93] was applied. The inclusive cross-section was adjusted to match the theoretical prediction, which was calculated at NLO in QCD with NNLL soft-gluon corrections [94]. Single top-quark production in the s-channel and t-channel was also modeled with the POWHEG BOX v2 generator at NLO in QCD, using the five-flavor and four-flavor schemes, respectively. For the single-top t-channel process, the inclusive cross-section was updated to align with the theory prediction calculated at NLO in QCD using HATHOR 2.1 [95, 96].

The contribution from material photon conversions (Mat Conv) and internal photon conversions (Int Conv) were estimated by using $Z \to \ell^+\ell^-$ events, simulated with the POWHEG BOX generator at NLO in QCD using the CT10NLO PDF set interfaced with PYTHIA 8 using the AZNLO tune [97].

The simulated events were normalized to cross-sections calculated at the highest available order in perturbation theory. Corrections were applied to ensure that the selection efficiencies, energy scales, and energy resolutions of reconstructed objects matched those derived from data control samples.

6 Event reconstruction and object identification

The event reconstruction and object identification are crucial steps in particle physics analyses. In these steps the raw data measured by the detector is used to define physical objects like electrons, muons and jets. The finale state signature targeted in this analysis is the fully leptonic decay of same-charge top-quark pairs. In detail, the final state signature consists of two same-charge leptons (e, μ), two jets containing b-hadrons and missing transverse momentum associated to the two neutrinos from the W boson decays.

First, the event preselection and triggers are described. Afterward, the different techniques and algorithms used to reconstruct and identify the physical objects are described in separate sections for electrons, muons and jets, respectively. All objects are reconstructed and calibrated with the default ATLAS methods using the ATLAS internal Analysis Top framework. In the end, the reconstruction of the missing transverse momentum is described, as well as the overlap removal procedure.

6.1 Event preselection and triggers

Triggers are used during the data taking at the LHC to select events that are of interest for the physics analysis and to be able to handle the huge amounts of data that are produced in the collisions. Therefore, the simulated events are also required to pass the same triggers as the data. In this analysis, all events are required to fire single leptons (e, μ) or dilepton ($e\mu$, ee, $\mu\mu$) triggers [98, 99]. Depending on the year of data taking, slightly different triggers are employed, which require specific p_{T} thresholds or identification requirements. Consequently, the simulated events for the 2015 data are required to pass the triggers for 2015, the simulated events for the 2016 data are required to pass the triggers for 2016 and so on. The complete list of lepton triggers used in this analysis is given in Table 6.1.

	Single lepton triggers (2015)
μ	HLT_mu20_iloose_L1MU15, HLT_mu50
e	HLT_e24_lhmedium_L1EM20VH, HLT_e60_lhmedium HLT_e120_lhloose

	Dilepton triggers (2015)
$\mu\mu$	HLT_mu18_mu8noL1
ee	HLT_2e12_lhloose_L12EM10VH
$e\mu, \mu e$	HLT_e17_lhloose_mu14

	Single lepton triggers (2016)
μ	HLT_mu26_ivarmedium, HLT_mu50
e	HLT_e26_lhtight_nod0_ivarloose, HLT_e60_lhmedium_nod0, HLT_e140_lhloose_nod0

	Dilepton triggers (2016)
$\mu\mu$	HLT_mu22_mu8noL1
ee	HLT_2e17_lhvloose_nod0
$e\mu, \mu e$	HLT_e17_lhloose_nod0_mu14

	Single lepton triggers (2017 / 2018)
μ	HLT_mu26_ivarmedium, HLT_mu50
e	HLT_e26_lhtight_nod0_ivarloose, HLT_e60_lhmedium_nod0, HLT_e140_lhloose_nod0

	Dilepton triggers (2017 / 2018)
$\mu\mu$	HLT_mu22_mu8noL1
ee	HLT_2e24_lhvloose_nod0
$e\mu, \mu e$	HLT_e17_lhloose_nod0_mu14

Table 6.1: List of single lepton and dilepton triggers used for 2015-2018 data taking.

In addition to the trigger requirements, events are preselected by requiring a successfully reconstructed primary vertex [100]. The primary vertex is defined as the vertex with the largest sum of squared transverse momenta of its associated tracks, $\sum p_{\mathrm{T}}^2$.

The primary vertex is additionally required to have at least two associated tracks, with each track satisfying $p_{\mathrm{T}} > 500\,\mathrm{MeV}$.

6.2 Electrons

The reconstruction, calibration and identification of electrons are described in detail in Ref. [101], a short summary is given in the following.

Electrons are reconstructed from tracks identified in the ID and the ECAL. The reconstruction process begins with the identification of clusters of energy deposition in the ECAL, matched to tracks in the ID. These clusters, known as *superclusters*, are dynamic, variable-size energy deposits in the ECAL. They are calibrated using complex algorithms, with the energy calibration performed using reconstructed $Z \to e^+e^-$ decays.

For this analysis, electrons are required to satisfy a transverse energy threshold of $E_T > 10\,\mathrm{GeV}$ and a pseudorapidity criterion of $|\eta| < 2.47$, excluding the calorimeter transition region between the barrel and end-cap components, $1.37 < |\eta| < 1.52$. Hence, the pseudorapidity requirement is also imposed on the electron superclusters. Electron candidates of interest should originate from the primary vertex of the proton-proton interaction. This is enforced by requiring the transverse impact parameter significance to fulfill $|d_0|/\sigma_{d_0} < 5$ and the longitudinal impact parameter to fulfill $|z_0 \sin\theta| < 0.5\,\mathrm{mm}$ for all electron candidates.

Identification criteria for electrons are categorized into two working points (WPs): Tight and Loose. The Tight WP is employed for the main analysis and includes stringent requirements on isolation to ensure high-quality electron reconstruction. The isolation criteria are applied to minimize contributions from nearby high-energy particles. The Loose WP is used for the data-driven estimation of fake electron contributions and the overlap removal. Both WPs are based on a likelihood approach to discriminate between real and fake electrons. The likelihood is constructed by using several low-level tracking and calorimeter-related input variables.

Electrons are additionally classified as prompt or non-prompt in this analysis. Non-prompt electrons are typically produced in the decay of hadrons, such as light-flavor or HF hadrons, hence, they do not directly originate from the primary vertex. To suppress non-prompt electrons, a boosted Decision Tree (BDT) is employed. The BDT is optimized to classify electrons as prompt or non-prompt, and the various WPs are used to define the final lepton categories. The final lepton categories, which are used throughout the analysis, are described in Section 6.4.

6.3 Muons

The reconstruction, calibration and identification of muons are described in detail in Ref. [102], a short summary is given in the following.

Muon reconstruction and identification is performed using information from the ID, calorimeters, and the MS. For this analysis, only combined (CB) muon candidates are considered. CB muons are reconstructed by matching MS tracks to ID tracks through a track-fitting process that accounts for energy loss in the calorimeters. This approach ensures high-quality reconstruction and precision, compared to ID or MS muons. Hence, CB muons are the most commonly used muon type in ATLAS physics analyses.

To ensure high efficiency and purity, specific WPs are defined for muon candidates. This analysis utilizes the Loose and Medium WPs. The Loose WP is designed to maximize selection efficiency by providing flexibility in regions where coverage gaps exist in the MS, such as $|\eta| < 0.1$ or low low-p_T muons. Hence, for low-p_T muons ($p_T < 7\,\text{GeV}$) only one MS station with at least three hits is required. The Medium WP, on the other hand, is optimized to balance efficiency and purity. It requires CB muons with at least two hits in the MDT or CSC chambers and three or more hits in other ID and MS layers. This WP is the most widely used for physics analyses, offering a good compromise between background rejection and signal efficiency.

All selected muon candidates must satisfy the transverse momentum requirement $p_T > 10\,\text{GeV}$ and are required to be within pseudorapidity range $|\eta| < 2.5$. Further cuts are applied on the impact parameters, ensuring $|d_0|/\sigma_{d_0} < 3$ and $|z_0 \sin\theta| < 0.5\,\text{mm}$ to maintain consistency with the primary vertex. Muons are preselected in this analysis by requiring them to fulfill the Loose WP. After passing the overlap removal algorithm, described in Section 6.7, muons candidates are required to satisfy the Medium identification WP. Similar to the electrons, the muons are then further split into the final lepton categories, to suppress non-prompt lepton backgrounds.

6.4 Leptons categories

The reconstructed muons and electrons are further classified via BDT WPs into four categories that are used throughout the analysis. The four BDT WPs are defined separately for electrons and muons, and are referred to as Loose inclusive (L_{inc}), Medium inclusive (M_{inc}), Medium (M), and Tight (T). Each lepton category is based on a combination of an identification WP and a non-prompt lepton BDT WP, which is described in detail in the following. For the electrons, the previously defined Loose identification WP is used for the L_{inc} category, while for the other three categories the electron is required to be identified as a Tight electron. For the muons, the

Medium identification WP is used for all four categories. Both electrons and muons are required to be isolated.

The goal of this BDT classification is to create categories that are optimized for the suppression of non-prompt leptons. The prompt leptons, in this analysis, originate from the decay of the W bosons, while the non-prompt leptons originate from the decay of light-flavor, HF hadrons, or photon conversions. Non-prompt leptons can be identified by tracing them back to their displaced decay vertices associated with the hadron decay. To suppress non-prompt leptons, a BDT discriminate was developed in Ref. [103]. The BDT makes use of several variables that are sensitive to non-prompt leptons, such as the lifetime, isolation, secondary vertex, or track information of the lepton candidate. The BDT is optimized separately for electrons and muons and will be referred to as the non-prompt lepton BDT is the following.

Two WPs, referred to as *Tight* and *VeryTight*, are defined based on the output score of non-prompt lepton BDT. The *Tight* WP achieves a prompt lepton efficiency for muons (barrel/endcap electrons) satisfying calorimeter- and track-based isolation criteria of approximately 60 % (60/70 %) at $p_{\mathrm{T}} \sim 20\,\mathrm{GeV}$, rising to a plateau of 95 % (95/90 %) at $p_{\mathrm{T}} \sim 40$ (40/65) GeV. The *VeryTight* WP, which is more stringent, provides a prompt lepton efficiency of around 55 % (55/60 %) for muons (barrel/endcap electrons) at $p_{\mathrm{T}} \sim 20\,\mathrm{GeV}$, reaching a plateau of 90 % (85/83 %) at $p_{\mathrm{T}} \sim 40$ (40/65) GeV. The rejection factor against muons (electrons) originating from b-hadron decays varies with p_{T} and $|\eta|$, and is enhanced by resolving ambiguities between overlapping reconstructed objects. For the *Tight* WP, the rejection factor ranges from 33 to 50 for muons and 20 to 50 for electrons. The *VeryTight* WP further improves these rejection factors, ranging from 50 to 100 for muons and 33 to 66 for electrons.

The BDT WPs *Tight* and *VeryTight* are used to define the lepton categories M_{inc} and T, while the lepton category M is defined by requiring the lepton candidate to satisfy the *Tight-not-VeryTight* BDT WP. As the name suggests, the *Tight-not-VeryTight* WP requires the lepton candidate to pass the *Tight* WP, but not the *VeryTight* WP. Consequently, the lepton categories M and T are mutually exclusive, while the M_{inc} category is the disjoint union of the M and T categories. The last lepton category L_{inc} is defined by requiring the lepton candidate to not pass any of the non-prompt lepton BDT WPs.

For electrons, two additional requirements are applied to suppress electrons with a charge misidentification (QmisID) and electrons that originate from photon conversions. These two requirements are requested by all lepton categories, except for the L_{inc} category. To suppress electrons reconstructed with an incorrect charge assignment, another BDT, referred to as ECIDS (ElectronChargeFlipTaggerTool), is deployed. The ECIDS is trained using six variables: p_T, η, the product of charge and transverse impact parameter (charge$\times d_0$), the ratio of cluster energy to track momentum (E/p), the angular difference between cluster position and extrapolated track ($\Delta\Phi$), and the weighted average charge of associated tracks. A minimum

BDT score of 0.7 is required, achieving a selection efficiency of 92.5 % for correctly charge-assigned electrons. The rejection efficiency for background electrons due to charge misassignment is approximately 96 % in the barrel region and 81 % in the endcaps, corresponding to rejection factors of 19 and 40, respectively.

To suppress non-prompt electrons originating from photon conversions occurring either in the detector material or at the IP, a selection is applied based on the invariant mass of the electron candidate and its closest opposite-charge track. Specifically, electron candidates associated with a displaced vertex at a radial distance from the IP ($r > 20\,\text{mm}$) and an invariant mass of the combination with the closest track with an energy smaller than 100 MeV are rejected. These electrons are classified as photon conversions in the detector material and are referred to as *MatCO*. Additionally, electrons with invariant masses in the range $0 < m_{\text{trk-trk,PV}} < 100\,\text{MeV}$ are classified as originating from photon conversions at the IP, referred to as *IntCO*, and are similarly vetoed. In order to enter any of the three lepton categories M_{inc}, M, or T, the electron candidate must pass the charge misassignment and conversion veto requirements. The L_{inc} category does not require these vetoes, as it is used for the data-driven estimation of the photon conversions and leptons that originate from HF hadron decays.

The definitions of the four leptons categories are summarized in Table 6.2, including all the requirements for electrons and muons.

Table 6.2: Summary of the definitions of the loose inclusive (L_{inc}), medium inclusive (M_{inc}), medium (M), and tight (T) leptons.

Lepton	e				μ			
Category	L_{inc}	M_{inc}	M	T	L_{inc}	M_{inc}	M	T
Isolation	Yes				Yes			
Non-prompt lepton BDT WP	No	*Tight*	*Tight-not-VeryTight*	*VeryTight*	No	*Tight*	*Tight-not-VeryTight*	*VeryTight*
Identification	Loose	Tight			Medium			
QmisID veto	No	Yes			Not applicable			
Photon conversion veto	No	Yes			Not applicable			
$\lvert d_0\rvert/\sigma_{d_0}$	< 5				< 3			
$\lvert z_0 \sin\theta\rvert$	< 0.5 mm							

6.5 Jets and *b*-tagging

Jets are the result of high-energy quarks or gluons hadronizing, due to confinement. Jets appear as clusters of energy deposits in the detector, due to the momentum conservation. They are reconstructed using these energy deposits registered in the ECAL and HCAL and tracking information from the ID, combined through

the particle-flow (PFlow) algorithm [104]. The reconstruction uses the anti-k_T algorithm [105, 106] with a radius parameter of $R = 0.4$, the jets are further calibrated using simulation-based corrections followed by *in situ* corrections [107]. Jet candidates are required to satisfy $p_{\mathrm{T}} > 25\,\mathrm{GeV}$ and $|\eta| < 2.5$. To mitigate pileup effects, the Jet Vertex Tagger (JVT) algorithm [108] is applied to jets with $p_{\mathrm{T}} < 60\,\mathrm{GeV}$ and $|\eta| < 2.4$, using the Tight JVT WP for pileup rejection.

Jets containing b-hadrons are identified using the DL1r algorithm [109], which makes use of track impact parameters and displaced vertices reconstructed in the ID to reconstruct additional decay vertices. This approach exploits both spatial and kinematic correlations associated with tracks that originate from the same b-hadron. Three b-tagging WPs are used in this analysis, corresponding to average b-tagging efficiencies of 60 %, 70 %, and 77 % for jets with $p_{\mathrm{T}} > 20\,\mathrm{GeV}$ and $|\eta| < 2.5$. The 77 % WP is used to define the 2ℓ regions, the 70 % WP is used for the overlap removal, while the 60 % WP is used to define the 3ℓ control regions. The rejection factors for light jets (jets without b or c-hadrons) are approximately 2500, 700, and 200 for the three WPs, respectively, while the charm-jet rejection factors are about 40, 12, and 6. The rejection factors and the average b-tagging efficiencies are determined for jets in simulated $t\bar{t}$ events and were taken from Ref. [109].

6.6 Missing transverse momentum

The cross-section of neutrino interaction is very small, hence, neutrinos can not be detected with ATLAS detector. However, the presence of neutrinos can be inferred from the imbalance in the transverse momentum of the visible particles in the event. The missing transverse momentum, $E_{\mathrm{T}}^{\mathrm{miss}}$, is calculated as the magnitude of the negative vector sum of the transverse momenta of all selected and calibrated objects in the event, including leptons and jets. Additionally, a term is included to account for soft particles not associated with these objects. This soft term is derived from ID tracks matched to the primary vertex, improving resilience against pileup contamination. $E_{\mathrm{T}}^{\mathrm{miss}}$ also considers energy deposits that are not linked to reconstructed physics objects [108], making it a crucial variable for identifying invisible particles like neutrinos or potential signals of new physics.

6.7 Overlap removal

To prevent the same energy deposits from being reconstructed multiple times as different objects in an event, a systematic overlap removal procedure is applied. The goal of this overlap removal procedure is to provide high efficiencies for the reconstruction of electrons, muons, and b-jets. Several overlap removal strategies

were investigated, and the following overlap removal was found to yield the highest expected signal sensitivity. This overlap removal procedure is commonly used in searches for BSM physics, e.g., in searches for super symmetry [110].

The overlap removal procedure starts with leptons, where, if two electrons are found within a separation of $\Delta R = 0.1$, only the one with the highest transverse momentum is kept. For cases where an electron and a muon are within $\Delta R = 0.1$, the muon is discarded if it is reconstructed solely from an ID track and corresponds to a calorimeter deposit resembling a minimum ionizing particle, otherwise the electron is removed. If an electron and a jet are within $\Delta R < 0.2$ of each other, the jet is removed unless the jet is considered b-tagged at the 70 % WP or has $p_{\mathrm{T}} > 200\,\mathrm{GeV}$, in which case the electron is discarded. Jets that are not b-tagged and have fewer than three associated tracks with $p_{\mathrm{T}} > 500\,\mathrm{MeV}$, found within $\Delta R < 0.4$ of a muon, are also removed, otherwise the muon is excluded. Finally, for each lepton satisfying these conditions, a variable-size cone of $\Delta R = 0.04 + 10\,\mathrm{GeV}/p_T^{\mathrm{lep}}$, extending up to a maximum $\Delta R = 0.4$, is defined. If any jet that survived previous steps falls within this cone, the lepton is rejected.

7 Analysis workflow

In this chapter, the analysis workflow is described. The analysis performs a maximum likelihood fit over four signal regions (SRs) and nine control regions (CRs). Additionally, four validation regions (VRs) are defined to validate the background estimation. The VRs are not included in the fit. All analysis region definitions are mutually exclusive and based on predictions from the simulation of signal and background events in the ATLAS detector. The analysis workflow is divided into four sections. The first section describes the definition of the SRs and VRs by using deep neural networks (DNNs). In the second section the background estimation for the reducible and irreducible background processes, utilizing CRs, is described. The third section describes the setup of the likelihood fit, which is used to extract the limits on the EFT operators. Finally the technical details for the parametrization of the EFT operators within the SRs are described.

7.1 Definition of signal and validation regions

In this analysis, four signal and four validations regions are defined by using a combination of machine-learning techniques and cut-based selection criteria. The regions are defined in several steps, as described in the flowchart in Figure 7.1. The flowchart starts with the selection of signal-like events in an initial event selection. The pre-selected events are then used to train a set of DNNs to separate the signal events from the different EFT operators, referred to as DNN^{SvsS}. The outputs of the DNNs are used to define separate preliminary regions enriched in signal events from the different considered operators. Afterward, each region is split by the total lepton charge into a $++$ and a $--$ region. A second set of DNNs, referred to as DNN^{SvsB}, is then trained to separate the signal from background events in each of the four regions. In a last step, the regions are split based on the $\Delta\phi_{\ell,\ell}$ variable to define the final SRs and VRs. The distribution of DNN^{SvsB} is used in the likelihood fits as a four bin distribution. Both set of DNNs use the same architecture and training setup, which is described in Section 7.1.2.

7.1.1 Initial same-charge lepton event selection

In this analysis, only the decay topology where both W bosons decay leptonically for the same-charge top-pair production is considered. The initial same-charge lepton event selection is summarized in Table 7.1. It requires the presence of two leptons $\ell = e, \mu$ with the same electric charge and transverse momentum of $p_{\text{T}} > 20\,\text{GeV}$ for both leptons. At least two jets are required with transverse momenta of $p_{\text{T}} > 25\,\text{GeV}$

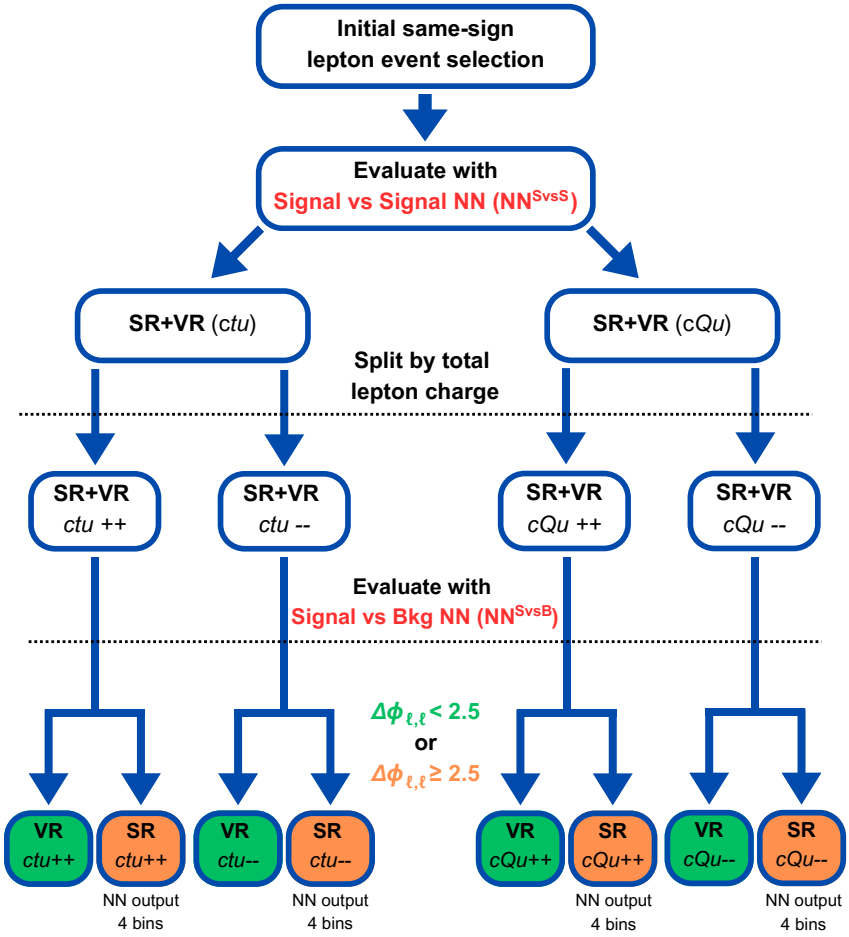

Figure 7.1: Flowchart representation of the definition of SRs and VRs. The first step is the selection of signal-like events. This is followed by the discrimination using a first set of deep neural networks, trained to separate signal events from the different EFT operators. The output of the NNs is used to define the SRs for $c_{tu}^{(1)}$ and c_{Qu}. Afterward, the regions are split by total lepton charge into ++ and −− regions. A second set of NNs is used to separate the signal from background contributions. As a last step, the regions are split based on the $\Delta\phi_{\ell,\ell}$ variable to define the final SRs and VRs. The output of this $\mathrm{NN}^{\mathrm{SvsB}}$ is split into four bins per SR. This plot was published in Ref. [1].

and pseudorapidities of $|\eta| < 2.5$. Either both leptons are required to be classified as M_{inc} and at least two jets have to satisfy the 77 % efficiency b-tagging WP, or both leptons are required to be classified as T and only one jet has to satisfy the 77 % efficiency b-tagging WP. This hybrid selection was found to yield a high signal efficiency while keeping the background contamination low.

The dominant background processes which fulfill this initial selection are the production of $t\bar{t}W$, $t\bar{t}Z$ and $t\bar{t}H$ and will be addressed in Section 7.2.1.

Table 7.1: Initial same-charge lepton event used for the selection of signal-like events.

Number of leptons	$N_\ell = 2$
Total lepton charge	+2 and -2
Lepton p_{T}	$p_{\mathrm{T}} > 20\,\mathrm{GeV}$
Lepton pseudorapidity	$e : \lvert\eta\rvert < 1.37$ && $1.52 < \lvert\eta\rvert < 2.47$ $\mu : \lvert\eta\rvert < 2.5$
Lepton ID	e :Tight μ :Medium
Number of jets	$N_{\mathrm{jets}} \geq 2$
Jet pseudorapidity	$\lvert\eta\rvert < 2.5$
Jet p_{T}	$p_{\mathrm{T}} > 25\,\mathrm{GeV}$
Lepton BDT WP and b-tag requirements	*Minc, Minc* with ≥ 2 b-tagged jets at 77 % WP OR *T, T* with ≥ 1 b-tagged jet at 77 % WP

7.1.2 Neural network architecture and training setup

The two sets of DNNs used for the signal discrimination and the signal to background discrimination are trained based on the Keras library [111] with Tensorflow as a backend [112]. The architecture of the DNNs was optimized by performing several hyperparameter scans. It was found that a simple DNN architecture with a small capacity reaches the same performance as very large and complex DNNs. This behavior is expected due to the relatively simple complexity of the input distribution for the classification task. Therefore, for simplicity, the same architecture is used for both sets of DNNs. The used architecture is a fully connected DNN with five hidden layers consisting of 128, 64, 32, 16, 8 nodes and a single node in the output layer. Depending on the number of input variables, this architecture yields a capacity of approximately 10,000 trainable parameters. The ReLU activation function [113] is used for all layers except the output layer, where a sigmoid activation function [114] is used to enforce and output between $[0, 1]$. Binary cross-entropy is used as the loss function with the Adam optimizer [115] and the learning rate is set to 10^{-4}. To prevent overtraining, a small L2-regularization [116] with $\lambda = 10^{-4}$ is applied to all hidden layers. The DNNs are trained with a batch size of 2000 and the training is interrupted once the validation loss has improved less than 10^{-3} within the last 100 epochs. The DNN weight snapshot that corresponds to the lowest validation loss is used for the final evaluation. The input variables are scaled with a standard scaler from Scikit-Learn [117] to improve the convergence and stability of the

DNN trainings. The scaler is fitted once on the full dataset, including all signal and background events, and is then used for all performed trainings. Furthermore, the weights used for the training are normalized to the same number of weighted events, to ensure that the DNNs are not biased by the different cross-sections.

In order to make use of all simulated events in the performed likelihood fit an odd-even cross-validation, also referred to as 2-fold cross-validation, is used for every DNN employed in this analysis. Hence, both data and simulated events are split into odd and even datasets according to their unique event number. Then instead of training a single DNN, two DNNs are trained, once using the odd dataset and once using the even dataset. In the training, the used odd or even datasets are further split by 80 % and 20 % into a training and validation dataset. For the final evaluation in this analysis, even events are evaluated with the DNN that is trained on the odd events and vice versa for the odd events are evaluated with the DNN that is trained on even events. This approach is common practice in the ATLAS Collaboration and allows using all simulated events in the performed statistical analysis, as each event is evaluated by a DNN that has not seen the event during training. However, the performance of the odd and even DNNs have to be checked carefully to ensure no bias is introduced by the odd-even cross-training. Furthermore, this approach has the disadvantage that the trainings only make use of 50 % of the available statistics, which can lead to worse separation power. By increasing the number of folds, the fraction of events used for the training can be increased, but increased computation cost and complexity of the general DNN setup. In the end, the 2-fold cross-validation was kept for this analysis in order to keep the setup as simple as possible and since enough events were available for the training.

7.1.3 Signal classification

In order to create preliminary SRs (SR+VR) enriched in events from the different EFT operators, a set of DNNs, referred as DNN^{SvsS}, is trained to discriminate same-charge top-pair events generated by different EFT operators. Events originating from either $\mathcal{O}_{Qu}^{(1)}$ or $\mathcal{O}_{Qu}^{(8)}$ have very similar kinematical properties and interfere with each other. Therefore, these events are grouped together into one preliminary SR, referred to as $\text{SR+VR}_{\text{cQu}}$. In contrast, events originating from $\mathcal{O}_{tu}^{(1)}$ are classified as $\text{SR+VR}_{\text{ctu}}$.

The training of the DNN^{SvsS} is performed by using two individual signal samples that are created by reweighting the nominal signal sample. The first signal sample only contains contributions from the $\mathcal{O}_{tu}^{(1)}$ operator with its WC set to $c_{tu}^{(1)} = 0.04$, while the two other WCs $c_{Qu}^{(1)}$ and $c_{Qu}^{(8)}$ set to 0. The second signal sample is reweighted to the following WCs values: $c_{tu}^{(1)} = 0$, $c_{Qu}^{(1)} = 0.1$, $c_{Qu}^{(8)} = 0.2$ and therefore contains only contributions from the $\mathcal{O}_{Qu}^{(1)}$ and $\mathcal{O}_{Qu}^{(8)}$ operators. These two signal samples were

selected for training because the largest kinematic differences were observed between them among the available 32 signal samples.

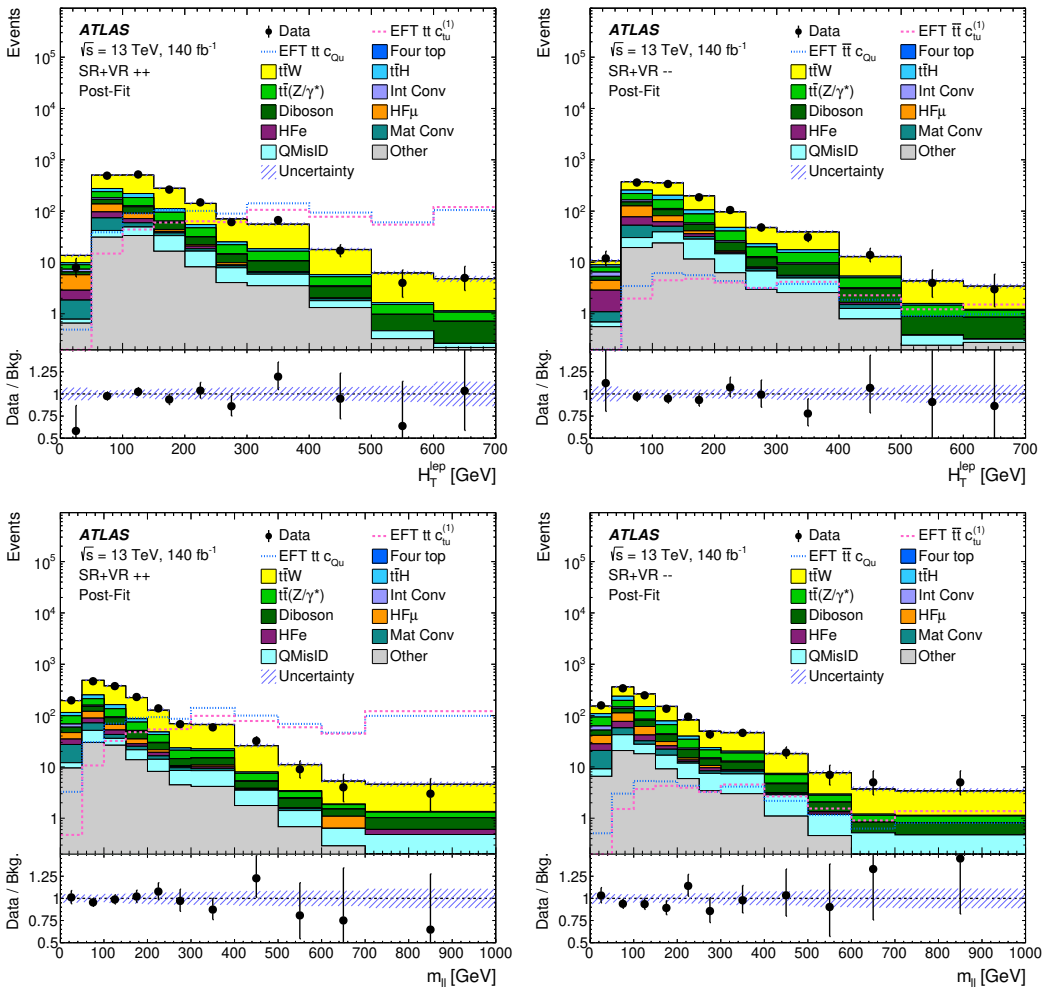

Figure 7.2: Comparison between data and the background expectation of the $H_{\mathrm{T}}^{\mathrm{lep}}$ and $m_{\ell\ell}$ distributions in the merged regions (SRs+VRs) split by lepton charge, shown after the background-only likelihood fit. Two signal samples using the Wilson coefficient values of $c_{tu}^{(1)} = 0.04$, $c_{Qu}^{(1)} = 0.0$, $c_{Qu}^{(8)} = 0.0$ and $c_{tu}^{(1)} = 0.0$, $c_{Qu}^{(1)} = 0.1$, $c_{Qu}^{(8)} = 0.2$ are shown as a dotted line and a dashed line, respectively. They are normalized to their respective predicted cross-sections. The ratio of the data to the total post-fit background is shown in the lower panel. The combined statistical and systematic uncertainty in the MC simulation is indicated by the hatched band, while the vertical error bars represent the statistical uncertainty in the data. These plots were published in Ref. [1].

For the training of the $\mathrm{DNN}^{\mathrm{SvsS}}$, the following nine kinematic quantities are used

as input variables. These include the angular variables $\Delta\phi_{\ell,\ell}$, $\Delta R_{\ell,\ell}$, and $\Delta\eta_{\ell,\ell}$ between the two leptons, as well as the invariant mass of the two-lepton system $m_{\ell,\ell}$. Additionally, the transverse momentum of the leading jet, $p_{\mathrm{T}}^{\mathrm{jet0}}$, the scalar sum of the transverse momenta of all jets, $H_{\mathrm{T}}^{\mathrm{jets}}$, and the scalar sum of the transverse momenta of all leptons, $H_{\mathrm{T}}^{\mathrm{lep}}$, are included. The missing transverse momentum $E_{\mathrm{T}}^{\mathrm{miss}}$ and the transverse mass of the combined lepton and $E_{\mathrm{T}}^{\mathrm{miss}}$ system $M_{\mathrm{T,lep\text{-}met}}$ are also used[1]. This set of input variables was optimized by rerunning the training with different sets of input variables and evaluating the performance between the different sets. Additionally, the importance of each input feature is carefully checked by using permutation feature importance [118]. The permutation feature importance is calculated by permuting the values of each feature and measuring the change in the loss function. The final set of input variables is the smallest possible set of input features that still yields the same performance as the full set of input features. The three most discriminating input variables are $m_{\ell\ell}$, $\Delta\phi_{\ell,\ell}$ and $H_{\mathrm{T}}^{\mathrm{lep}}$. The distributions for the nine used input variables and the feature importance ranking plot for the $\mathrm{DNN}^{\mathrm{SvsS}}$ are shown in the Appendix A.1.

In Figure 7.2 the distributions for the two input variables H_{T}^{lep} and $m_{\ell\,\ell}$ are shown for the preliminary regions SR+VR after applying the initial event selection, split by total lepton charge but before performing the separation with the $\mathrm{DNN}^{\mathrm{SvsS}}$. The lepton charge-split is already introduced for these plots to show the kinematic differences between the signals tt and $\overline{tt}$. Moreover, the minor kinematic differences between the two signal samples can be seen, highlighting the challenges in discriminating between the different EFT operators. The distributions are shown after performing the background-only likelihood fit to the CRs are first two bins of the SRs, which is described in Section 9.1, and show good data to MC agreement.

The training setup and DNN architecture described in Section 7.1.2 is used. In Figure 7.3 the loss and accuracy curves for the training and validation datasets are shown for the odd and even DNN respectively. The accuracy for a binary classification is defined as:

$$\text{Accuracy} = \frac{\mathrm{TP} + \mathrm{TN}}{\mathrm{TP} + \mathrm{TN} + \mathrm{FP} + \mathrm{FN}}, \tag{7.1}$$

where TP is the number of true positive events, FP the number of false positive events, TN the number of true negative events and FN the number of false negative events. Following the given equation, the accuracy is defined as the ratio of correctly classified events divided by the total number of events. The best epoch is marked with a vertical dashed line in Figure 7.3. No overtraining is observed, and the performance of the odd and even DNNs are in good agreement. Hence, the odd and even events are recombined in the next steps, by evaluating the odd events with the even DNN

[1]The transverse mass is defined as: $M_{\mathrm{T}} = \sqrt{E^2 - p_{\mathrm{z}}^2}$

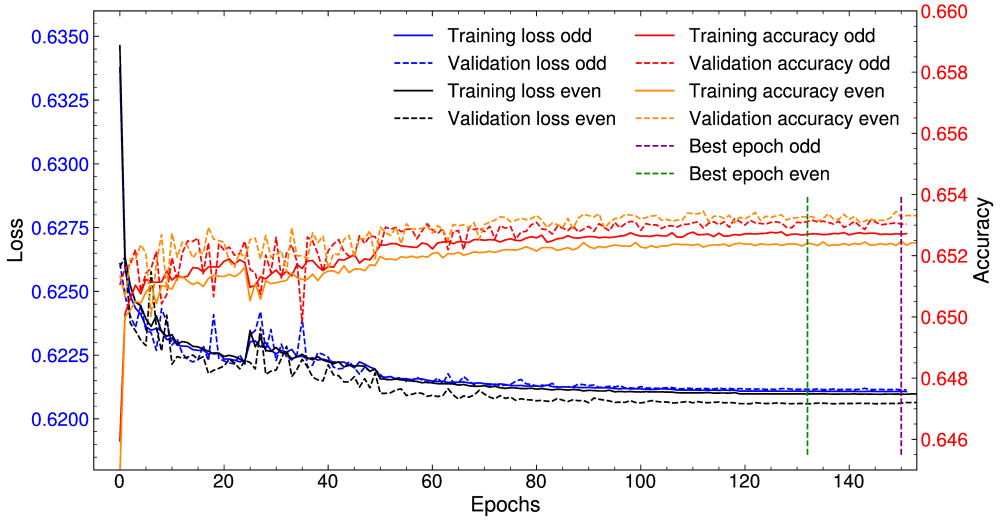

Figure 7.3: Loss and accuracy curves for the odd and even DNNs$^{\text{SvsS}}$ for the training and validation datasets per epoch. The best epoch is selected based on the lowest validation loss and is marked with a vertical dashed line.

and vice versa. For the next steps, the background is also evaluated with odd and even DNNs to also sort the background events into one of the preliminary SRs.

The selected best epochs for the odd and even DNNs$^{\text{SvsS}}$ correspond to validation accuracies of 65.31 % and 65.35 % respectively for the chosen cut-value of 0.538. The cut-value is used to decide if an event is classified into the SR+VR$_{\text{ctu}}$ or SR+VR$_{\text{cQu}}$ region. This value is optimized by scanning over the DNN output distribution in the range of $[0, 1]$ in $i = [0, 1000]$ steps following the equation:

$$\text{Cut-value} = \max_{i=[0,1000]}(\varepsilon_{\text{i},1} + \varepsilon_{\text{i},2} - \frac{\varepsilon_{\text{i},1} - \varepsilon_{\text{i},2}}{2}), \tag{7.2}$$

where $\varepsilon_{\text{i},1}$ and $\varepsilon_{\text{i},2}$ are the efficiencies for the correct classification of the $\mathcal{O}_{tu}^{(1)}$ and $\mathcal{O}_{Qu}^{(1)}/\mathcal{O}_{Qu}^{(8)}$ events at the i-th cut value. A penalty term is added to ensure that both efficiencies are maximized.

Figure 7.4 shows the DNN$^{\text{SvsS}}$ output distribution for the recombined odd and even simulated signal events, as well as for the total simulated background events that fulfill the initial same-charge lepton event selection. The vertical line marks the cut-value at NN$^{\text{SvsS}} = 0.538$, with events classified into SR+VR$_{\text{ctu}}$ and SR+VR$_{\text{cQu}}$ for NN$^{\text{SvsS}} \leq 0.538$ and NN$^{\text{SvsS}} > 0.538$, respectively. The chosen cut-value was optimized to yield maximum classification efficiencies for the signal events in both

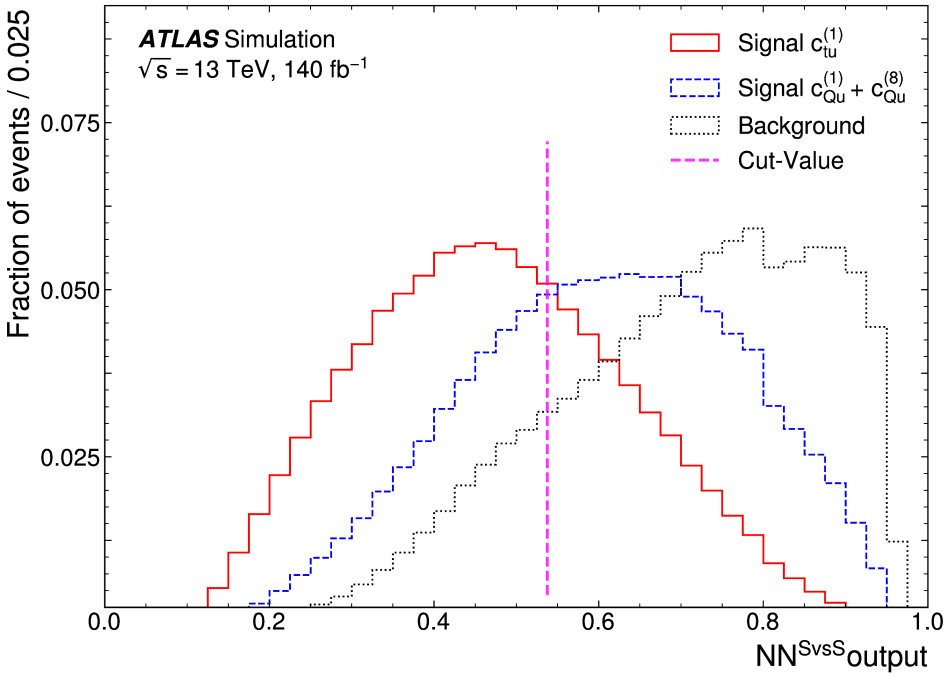

Figure 7.4: NN output variable for DNN$^{\text{SvsS}}$ used to classify the data into $c_{tu}^{(1)}$- and c_{Qu}-like regions. The distribution for signal $c_{tu}^{(1)}$ was generated with $c_{tu}^{(1)} = 0.04$ with the other Wilson coefficients being set to zero, while the other signal distribution was produced with $c_{tu}^{(1)} = 0, c_{Qu}^{(1)} = 0.1$ and $c_{Qu}^{(8)} = 0.2$. The background distribution shown is the sum of all background processes from MC simulation before the likelihood fit. The value chosen to separate the signal events is shown by the vertical dashed line. An efficiency of $\approx 65\,\%$ is obtained for the correct classification of c_{Qu} events and of $c_{tu}^{(1)}$ events. This plot was published in Ref. [1].

regions, leading to a classification efficiency of 65 % in both regions. The efficiency times acceptance values for signal events entering the SR+VR$_{\text{ctu}}$ and SR+VR$_{\text{cQu}}$ regions are 26.8 % and 12.4 % for events from the $\mathcal{O}_{tu}^{(1)}$ operator, and 15.8 % and 19.5 % for events from the $\mathcal{O}_{Qu}$ operators. Furthermore, it is observed that the background events are more often classified into the SR+VR$_{\text{cQu}}$ region, leading to a smaller signal to background ratio in this region. The distribution of the DNN$^{\text{SvsS}}$ output split for the different background processes is shown in Figure 7.5, highlighting that all background processes tend to be classified more often into the SR+VR$_{\text{cQu}}$ region.

The final performance of the DNN$^{\text{SvsS}}$ is evaluated with a receiver operating char-

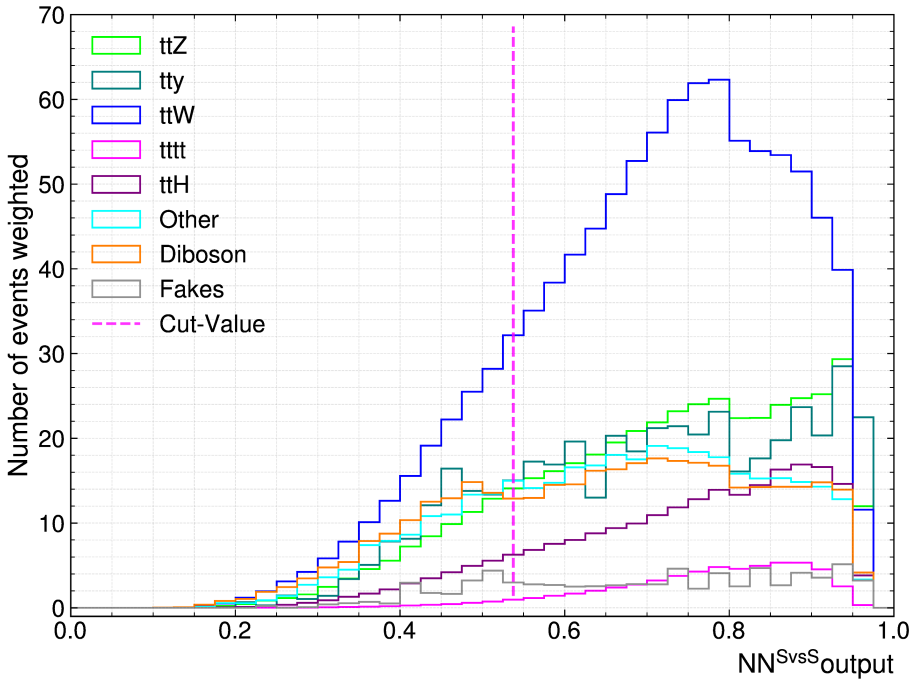

Figure 7.5: NN output variable for DNN^{SvsS} used to classify the data into $c_{tu}^{(1)}$- and c_{Qu}-like regions. The background events are shown split into the different background processes. All background processes tend to be classified more often into the $\text{SR+VR}_{\text{cQu}}$ region.

acteristic curve (ROC-curve) for the odd, even and combined trainings. The ROC curves are shown Figure 7.6. It can be observed that the performance of the odd and even DNNs are in good agreement. Given the challenging classification task, a good discrimination power is achieved for the DNN^{SvsS}.

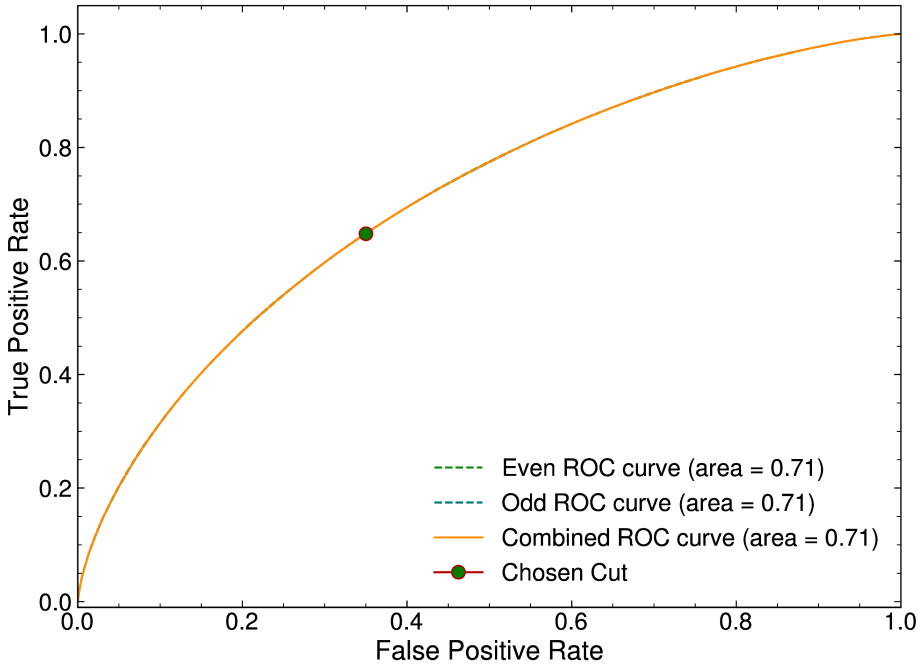

Figure 7.6: ROC curves for the odd, even and combined trainings of the DNN^{SvsS}. The performance of the odd and even DNNs is in very good agreement, as indicated by their overlapping ROC curves. The green dot marks the chosen cut-value for the DNN^{SvsS} output to define $\text{SR+VR}_{\text{ctu}}$ and $\text{SR+VR}_{\text{cQu}}$.

7.1.4 Discrimination of signal and background events

In the next step, a second set of DNNs, referred to as DNN^{SvsB}, is trained to separate the signal from the background events. Before proceeding with the training of the DNNs, the regions are split by the total lepton charge into the following four regions: $\text{SR+VR}_{\text{ctu}++}$, $\text{SR+VR}_{\text{ctu}--}$, $\text{SR+VR}_{\text{cQu}++}$ and $\text{SR+VR}_{\text{cQu}--}$. In order to reach the best possible signal to background discrimination, a split by total lepton charge is introduced. Due to the large asymmetry in the production cross-sections between tt and $\overline{tt}$ signal events and due to their different kinematics, this split increases the performance of the DNNs[2]. For each of the four regions, an odd and an even DNN is separately trained, following the same training setup and DNN architecture as for the DNN^{SvsS}.

[2]The split by total lepton charge has not been applied to the DNN^{SvsS} as it was found to have no effect on the discrimination of signal events.

The DNNs$^{\text{SvsB}}$ are trained using the following six input variables: $H_{\text{T}}^{\text{lep}}$, $p_{\text{T}}^{\text{jet0}}$, $M_{\text{T,lep-met}}$, the jet multiplicity N_{jets}, the b-tagging scores of the leading jet $S_{\text{b-tagging}}^{\text{jet0}}$, and b-tagging scores of the subleading jet $S_{\text{b-tagging}}^{\text{jet1}}$. The input variables for these DNNs were optimized in the same way as for the DNN$^{\text{SvsB}}$ by evaluating the performance of the DNNs with different sets of input variables. However, all dilepton variables were dropped at the start of the optimization process, despite indicating strong discrimination power. This removal is motivated by the cut on $\Delta\phi_{\ell,\ell}$ introduced later to define the final SRs and VRs. As most of the signal events fulfill $2.5 < \Delta\phi_{\ell,\ell}$, applying this cut allows increasing the signal to background ratio in the final SRs, while also providing VRs which mostly contain background events. The VRs are then used to validate the background estimation by comparing the predicted background to the observed data. Therefore, all dilepton variables are dropped, due to being strongly correlated to $\Delta\phi_{\ell,\ell}$. After dropping the dilepton variables, the input variables optimization is performed. The above-given list of input features was found to be the minimal set of input variables that still yields the same performance as the full set of input features. The three most discriminating input variables for the DNN$^{\text{SvsB}}$ are $H_{\text{T}}^{\text{lep}}$, $p_{\text{T}}^{\text{jet0}}$ and N_{jets}. The distributions for the six used input variables and the feature importance ranking plots for the four regions are shown in the Appendix A.2.

In Figure 7.7 the loss and accuracy curves for the DNN$^{\text{SvsB}}$ are shown for the four SR+VR regions. All trainings show very fast convergence. The ++ SRs show slightly better performance with respect to the −− regions by reaching approximately 7 % better validation accuracy in both regions. This performance difference is expected, as the kinematic differences between the tt signal and the background are significantly larger compared to $\overline{tt}$. Furthermore, it can be seen that the odd and even trainings behave very similar and achieve similar performance.

In Figure 7.8 the NN-output distributions from the MC samples for the four regions are shown, where the odd and even events are recombined again. The separation power s is provided in the sub-caption for each region. The separation power is calculated with the following equation:

$$s = \frac{1}{2} \sum_i \frac{(N_{\text{sig}}(i) - N_{\text{bkg}}(i))^2}{N_{\text{sig}}(i) + N_{\text{bkg}}(i)}, \tag{7.3}$$

where $N_{\text{sig}}(i)$ and $N_{\text{bkg}}(i)$ denote the number of signal and background events in the i-th bin, respectively. The separation s can range from 0 up to 1, where 1 corresponds to perfect discrimination.

The final performance is evaluated again by using ROC curves for the odd, even and combined events. The ROC curves split in odd and even are shown in Figure 7.9a, while the combined ROC curves are shown in Figure 7.9b. The performance of the odd and even DNNs are in good agreement, and the combined training shows a very good discrimination power for the DNN$^{\text{SvsB}}$.

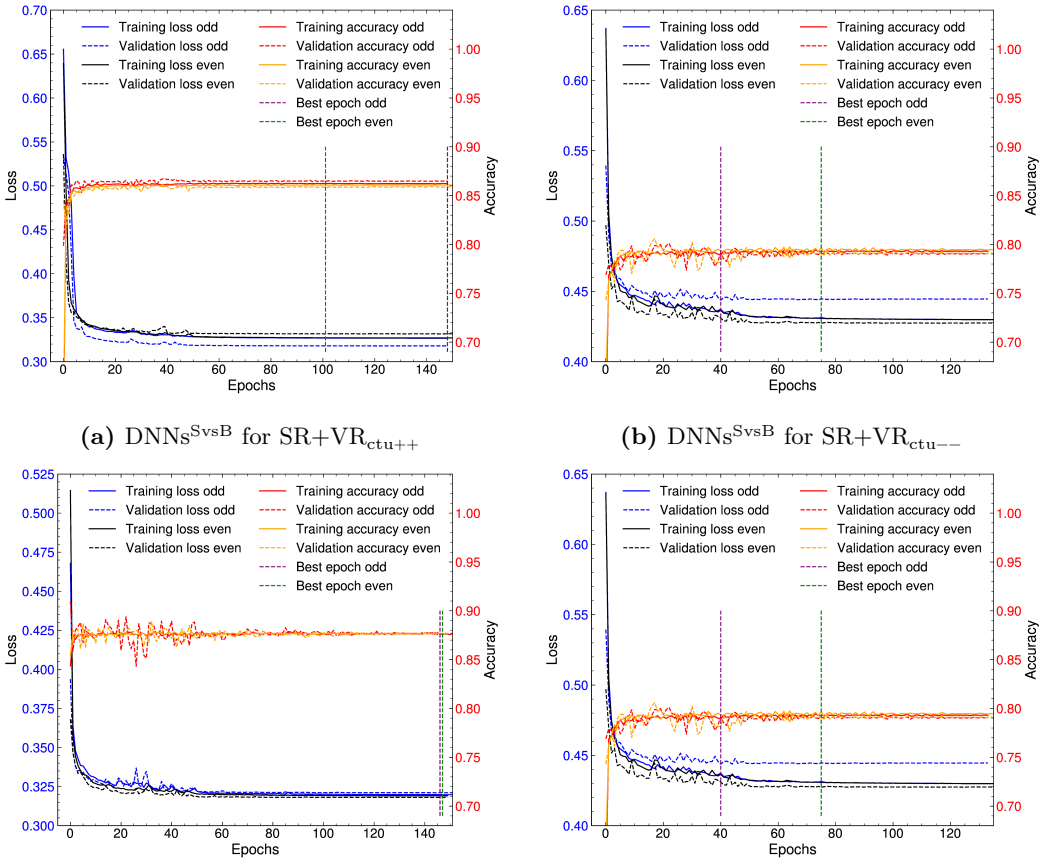

(a) DNNs$^{\mathrm{SvsB}}$ for SR+VR$_{\mathrm{ctu++}}$

(b) DNNs$^{\mathrm{SvsB}}$ for SR+VR$_{\mathrm{ctu--}}$

(c) DNNs$^{\mathrm{SvsB}}$ for SR+VR$_{\mathrm{cQu++}}$

(d) DNNs$^{\mathrm{SvsB}}$ for SR+VR$_{\mathrm{cQu--}}$

Figure 7.7: Loss and accuracy curves for the odd and even training for the DNNs$^{\mathrm{SvsB}}$ for SR+VR$_{\mathrm{ctu++}}$ (a), SR+VR$_{\mathrm{ctu--}}$ (b), SR+VR$_{\mathrm{cQu++}}$ (c), and SR+VR$_{\mathrm{cQu--}}$ (d) for the training and validation datasets per epoch. The best epoch is selected based on the lowest validation loss and is marked with a vertical dashed line.

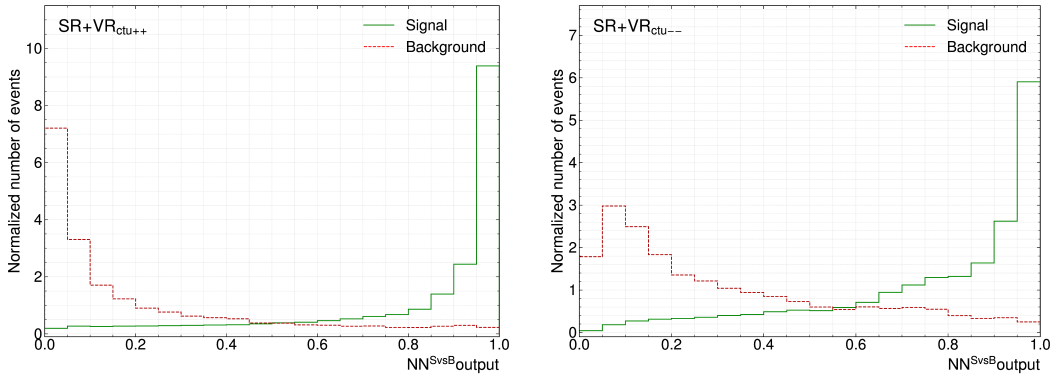

(a) $s = 57.3\,\%$

(b) $s = 41.7\,\%$

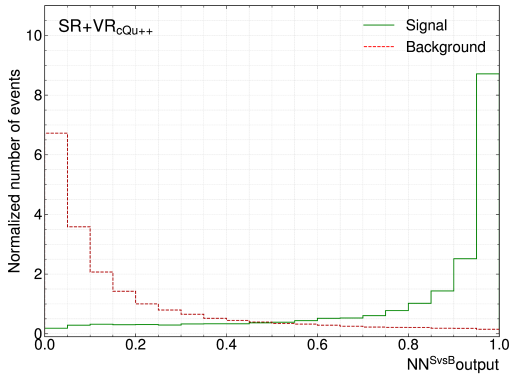

(c) $s = 58.8\,\%$

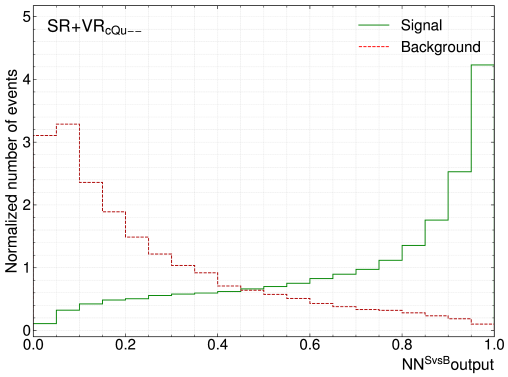

(d) $s = 41.2\,\%$

Figure 7.8: DNN$^{\mathrm{SvsB}}$ output distributions for the signal and background events for SR+VR$_{\mathrm{ctu++}}$ (a), SR+VR$_{\mathrm{ctu--}}$ (b), SR+VR$_{\mathrm{cQu++}}$ (c), and SR+VR$_{\mathrm{cQu--}}$ (d). For each subfigure, the separation power, s, is indicated in its subcaption.

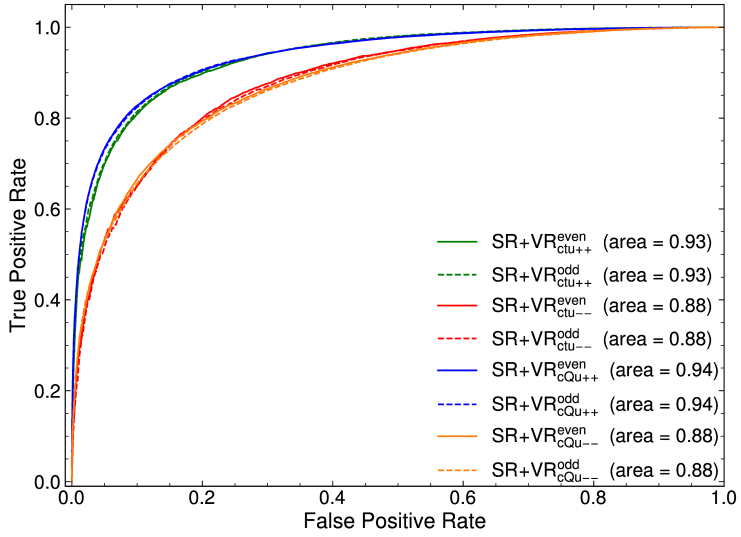

(a)

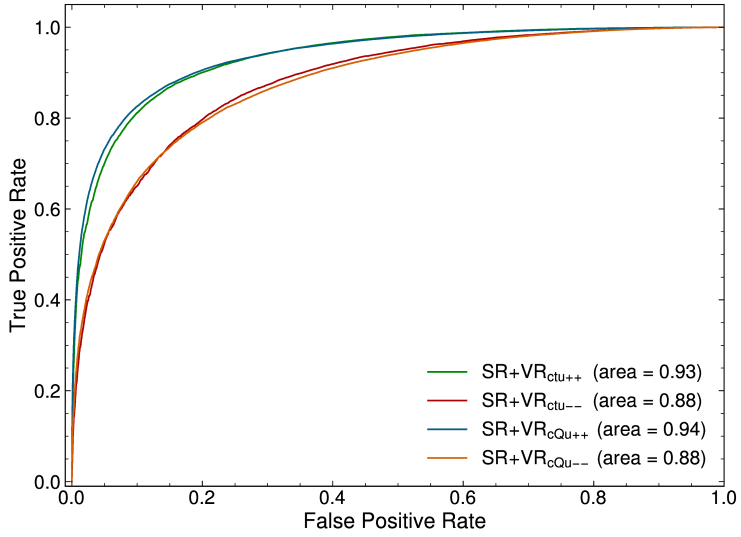

(b)

Figure 7.9: ROC curves to evaluate the performance of the DNN$^{\text{SvsB}}$ for the odd, even and combined trainings. The odd and even ROC curves DNN$^{\text{SvsB}}$ for the four SRs are shown in (a), while the combined ROC curves are shown in (b). The performance of the odd and even DNNs are in good agreement. Very good discrimination power is achieved for the DNN$^{\text{SvsB}}$.

7.1.5 Final signal and validation regions

The final SRs and VRs are defined by splitting the SR+VR regions according to the $\Delta\phi_{\ell,\ell}$ variable. The distribution of $\Delta\phi_{\ell,\ell}$ for the four preliminary regions is shown in Figure 7.10.

The $\Delta\phi_{\ell,\ell}$ distribution shows a relatively strong separation between the signal and background events. Furthermore, the distribution highlights that most of the background events are contained in the c_{Qu}-like regions, as the c_{tu}-like regions barely contain events with $\Delta\phi_{\ell,\ell} < 2.0$. Additionally, the asymmetry for the cross-sections between the signal events can be observed when comparing the $++$ and $--$ regions.

In all four regions, a cut on $\Delta\phi_{\ell,\ell} > 2.5$ is applied to define the final SRs and VRs. By applying this selection, most of the signal events are kept in the final SRs and the background contamination is strongly reduced, while the VRs are enriched in background events and contain only a few signal events. Hence, the VRs are used later on to validate the background estimation strategy by comparing the predicted background to the observed data. The VRs are not used to perform the fit. In detail, applying the $\Delta\phi_{\ell,\ell}$ cut results in the following rejection rates: 4.1 % (9.0 %) of the signal events and 24.8 % (24.5 %) of the background events are rejected for $\mathrm{SR}_{\mathrm{ctu}++}$ ($\mathrm{SR}_{\mathrm{ctu}--}$), while 31.4 % (54.8 %) of the signal events and 85.7 % (85.9 %) of the background events are rejected for $\mathrm{SR}_{\mathrm{cQu}++}$ ($\mathrm{SR}_{\mathrm{cQu}--}$).

The distributions of $\mathrm{DNN}^{\mathrm{SvsB}}$-output for SRs and VRs before the likelihood fit (pre-fit) are shown in Figure 7.12 and Figure 7.11, respectively.

For the four SRs a binning of four bins per region is chosen, while for the VRs the binning depends on the expected background yields. The $\mathrm{VR}_{\mathrm{ctu}++}$ and $\mathrm{VR}_{\mathrm{ctu}--}$ are used as single bin VRs due to the small number of events, while the $\mathrm{VR}_{\mathrm{cQu}++}$ and $\mathrm{VR}_{\mathrm{cQu}--}$ are split into ten bins each. Pre-fit yield tables for the SRs and VRs are shown in Table 7.2 and Table 7.3, respectively.

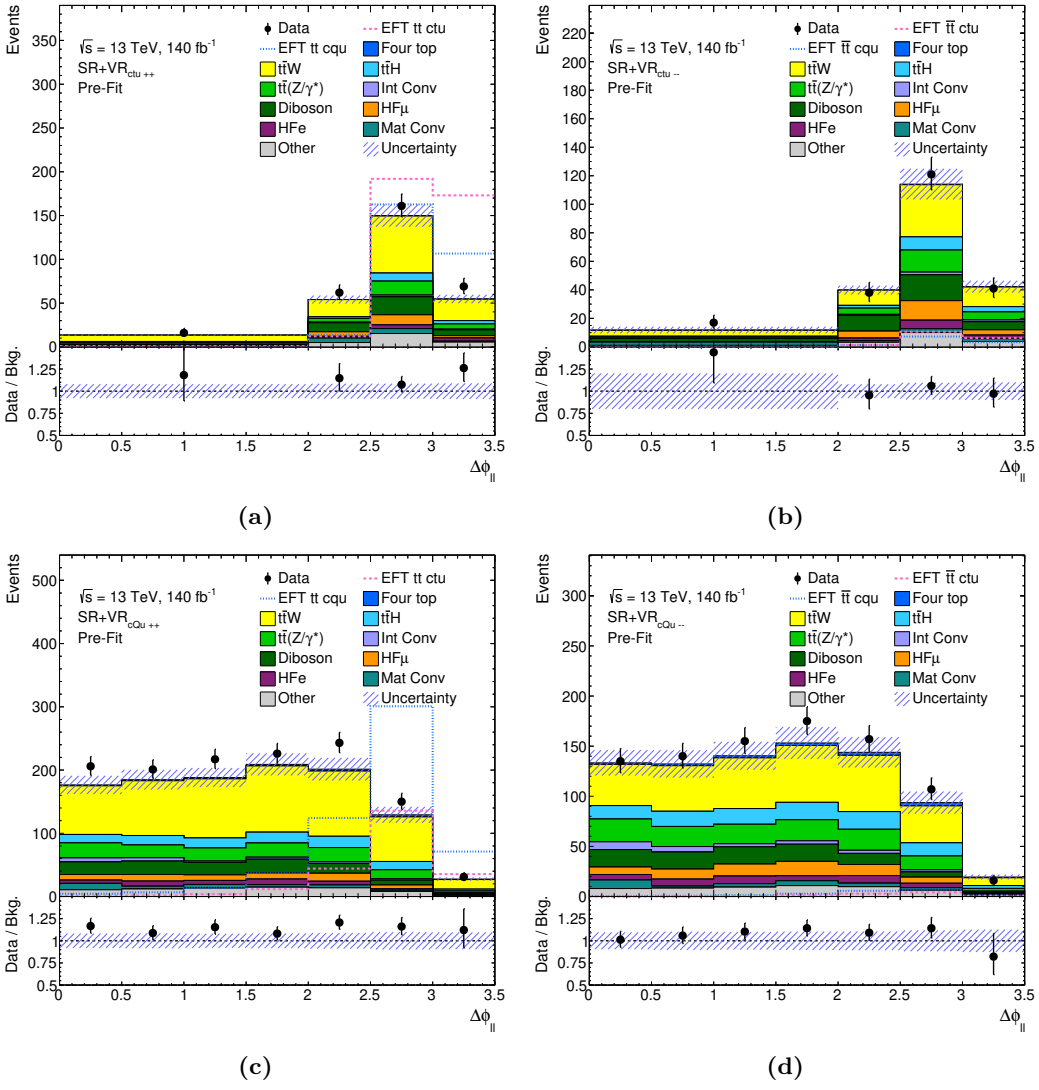

Figure 7.10: $\Delta\phi_{\ell,\ell}$ distribution in the four preliminary SR+VR$_{\mathrm{ctu++}}$ (a), SR+VR$_{\mathrm{ctu--}}$ (b), SR+VR$_{\mathrm{cQu++}}$ (c) and SR+VR$_{\mathrm{cQu--}}$ (d) regions. The ratio of the data to the total background prediction is shown in the bottom panel. Two signal samples using the Wilson coefficient values of $c_{tu}^{(1)} = 0.04$, $c_{Qu}^{(1)} = 0.0$, $c_{Qu}^{(8)} = 0.0$ and $c_{tu}^{(1)} = 0.0$, $c_{Qu}^{(1)} = 0.1$, $c_{Qu}^{(8)} = 0.2$ are shown as a dotted line and a dashed line, respectively. The combined statistical and systematic uncertainty in MC simulation is indicated by the hatched band, while the vertical error bars represent the statistical uncertainty in the data.

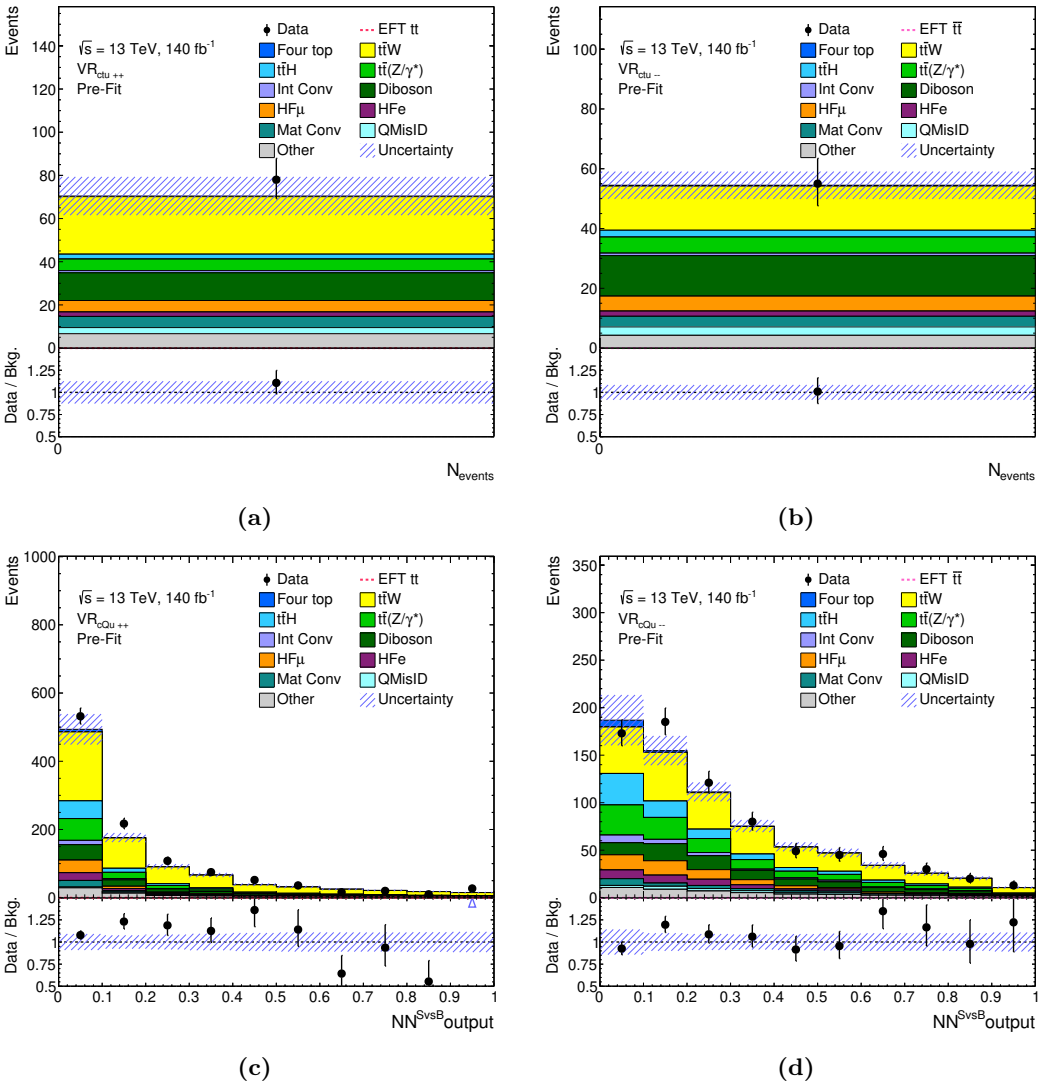

Figure 7.11: Distributions of the $\mathrm{NN^{SvsB}}$ output for data and the expected background before the likelihood fit in the four SRs. In (a) and (b) the number of events is shown instead of the $\mathrm{NN^{SvsB}}$ distribution, due to the small number of events. The predicted pre-fit background is shown as filled histograms. The ratio of the data to the total pre-fit background is shown in the lower panel. The combined statistical and systematic uncertainty in MC simulation is indicated by the hatched band, while the vertical error bars represent the statistical uncertainty in the data.

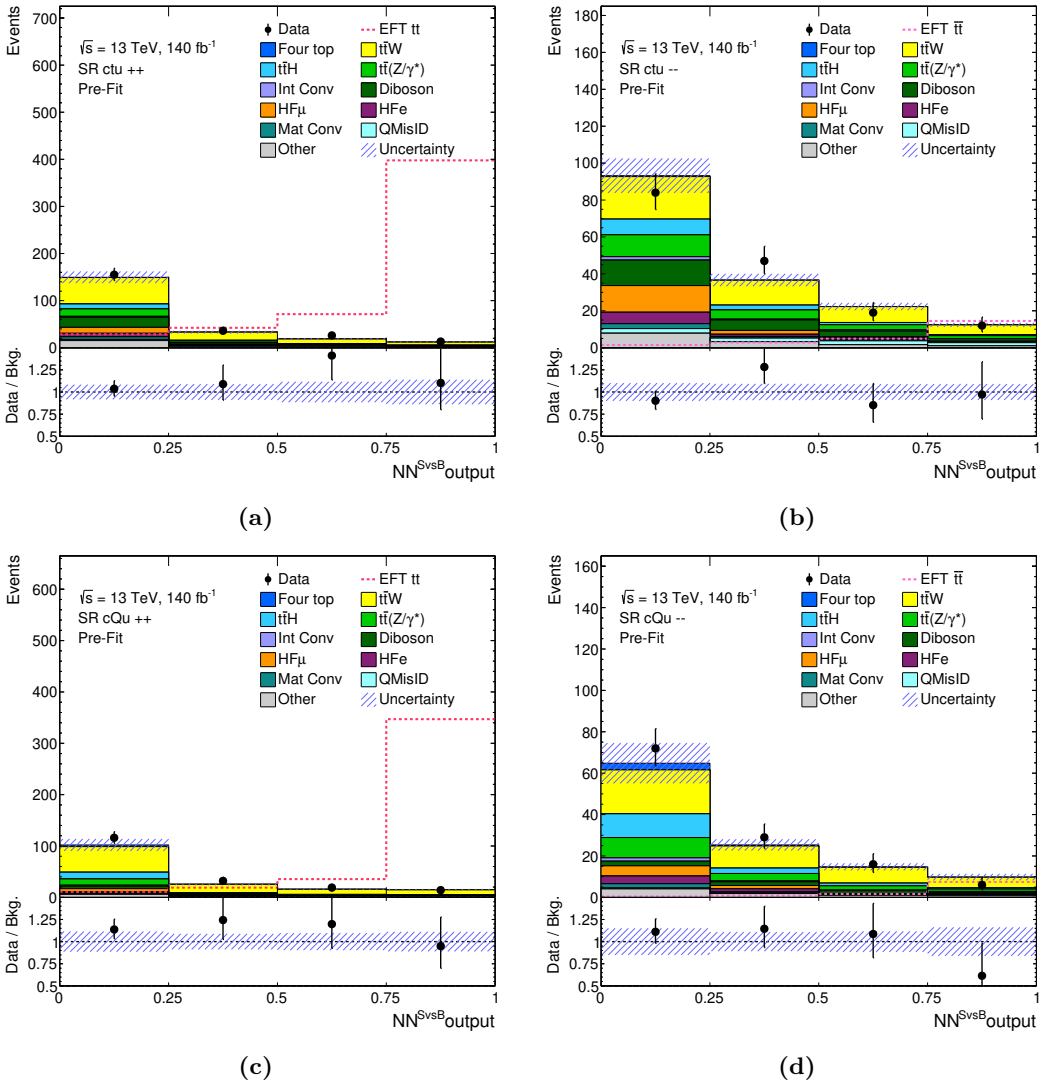

Figure 7.12: Distributions of the $\mathrm{NN^{SvsB}}$ output for data and the expected background before the likelihood fit in the four SRs. The predicted pre-fit background is shown as filled histograms. The signal distribution using the Wilson coefficient values $c_{tu}^{(1)} = 0.04$, $c_{Qu}^{(1)} = 0.1$, $c_{Qu}^{(8)} = 0.1$ is shown with a dotted line and corresponds to a signal of 100 fb. The ratio of the data to the total pre-fit background is shown in the lower panel. The combined statistical and systematic uncertainty in MC simulation is indicated by the hatched band, while the vertical error bars represent the statistical uncertainty in the data.

Table 7.2: Summary of the observed and predicted number of events in the four SRs. The background prediction is shown before the likelihood fit. The individual uncertainties are shown for the different background processes. The uncertainties represent the sum of the statistical and systematic uncertainties.

Process	SR_{ctu++}	SR_{ctu--}	SR_{cQu++}	SR_{cQu--}
$t\bar{t}W$	90 ± 11	50.3 ± 8.0	85.7 ± 8.3	44.6 ± 4.2
$t\bar{t}(Z/\gamma^*)$	21.9 ± 2.9	21.1 ± 2.7	17.0 ± 2.1	16.6 ± 2.1
$t\bar{t}H$	13.1 ± 9.0	13.0 ± 8.6	16 ± 12	16 ± 11
Four top	0.70 ± 0.15	0.68 ± 0.14	4.14 ± 0.83	4.05 ± 0.82
Diboson	27.2 ± 2.1	23.8 ± 1.6	9.36 ± 0.91	6.30 ± 0.58
HFe	8.0 ± 3.5	8.6 ± 3.8	3.4 ± 1.1	5.7 ± 3.4
HFμ	14.1 ± 3.5	17.4 ± 4.2	6.9 ± 2.2	6.6 ± 2.1
Mat Conv	6.6 ± 1.4	4.62 ± 0.51	2.27 ± 0.35	2.85 ± 0.72
Int Conv	2.7 ± 1.4	3.1 ± 1.6	2.2 ± 1.2	2.8 ± 1.5
QMisID	8.2 ± 2.2	8.2 ± 2.2	1.49 ± 0.39	1.49 ± 0.39
Other	20.7 ± 5.8	13.8 ± 4.3	9.7 ± 2.9	7.6 ± 2.9
Total Background	213 ± 18	165 ± 15	158 ± 16	115 ± 14
Data	230	162	181	123

Table 7.3: Summary of the observed and predicted number of events in the four VRs. The background prediction is shown before the likelihood fit. The individual uncertainties are shown for the different background processes. The uncertainties represent the sum of the statistical and systematic uncertainties.

Process	VR_{ctu++}	VR_{ctu--}	VR_{cQu++}	VR_{cQu--}
$t\bar{t}W$	26.7 ± 2.4	15 ± 2.0	465 ± 40	250 ± 23
$t\bar{t}(Z/\gamma^*)$	5.34 ± 0.76	5.39 ± 0.71	109 ± 12	104 ± 12
$t\bar{t}H$	2.2 ± 1.6	2.3 ± 1.5	79 ± 56	79 ± 56
Four top	0.288 ± 0.061	0.279 ± 0.058	10.8 ± 2.2	11.1 ± 2.2
Diboson	12.8 ± 1.2	13.6 ± 1.2	98.7 ± 7.4	79.8 ± 5.4
HFe	2.1 ± 1.5	1.75 ± 0.92	34 ± 13	33 ± 13
HFμ	5.3 ± 8.8	5.0 ± 1.4	50 ± 13	55 ± 14
Mat Conv	5.2 ± 2.3	3.54 ± 0.45	28.9 ± 3.2	22.3 ± 2.8
Int Conv	1.04 ± 0.56	0.82 ± 0.76	19.4 ± 9.8	23 ± 11
QMisID	2.83 ± 0.77	2.83 ± 0.77	16.9 ± 4.7	16.9 ± 4.7
Others	6.7 ± 1.8	4.3 ± 1.2	64 ± 18	46 ± 15
Total Background	70.4 ± 8.9	54.5 ± 4.6	977 ± 79	720 ± 70
Data	78	55	1093	762

7.2 Background estimation

Various approaches are utilized in this analysis to perform the background estimation. The majority of background processes are estimated using Monte Carlo (MC) simulation, while certain background processes are determined through data-driven methods. The different background processes are sorted into several groups for the purpose of the background estimation, plotting and the likelihood fit itself. Specifically, the following groups are defined for this analysis:

- $t\bar{t}(Z/\gamma^*)$ includes $t\bar{t}Z$, $t\bar{t}\gamma$ and $t\bar{t}\ell\ell$
- Diboson includes VV and $qqVV$
- HFe includes $t\bar{t}$, V+jets and single-top production with a non-prompt lepton
- HFμ includes $t\bar{t}$, V+jets and single-top production with a non-prompt lepton
- Mat Conv includes $Z \to \ell^+\ell^-$ (Mat Conv) and $t\bar{t}$ with a photon conversion candidate within the detector material region
- Int Conv includes $Z \to \ell^+\ell^-$+(γ*), W+jets, $Z \to \ell^+\ell^-$, $t\bar{t}$, single top and $V\gamma$ with a photon conversion candidate at the IP.
- QMisID is purely data-driven
- Others includes $t(Z/\gamma^*)$, $t\bar{t}t$, $t\bar{t}WH$, $t\bar{t}W^+W^-$, $t\bar{t}ZZ$, $t\bar{t}HH$, VH, VVV

Furthermore, the background processes are sorted into two categories, irreducible and reducible backgrounds. The irreducible backgrounds are defined by being able to pass the SR selection criteria, while the reducible backgrounds are only able to pass the SR selection due to misidentified or non-prompt leptons.

7.2.1 Irreducible background processes

Irreducible background processes play a crucial role in the analysis, as they have the largest contribution to the total background. Irreducible processes produce final states resembling the signal topology, often involving multiple prompt leptons and accompanying b-jets. The primary irreducible backgrounds include $t\bar{t}W$, $t\bar{t}(Z/\gamma^*)$ and $t\bar{t}H$.

The modeling of these backgrounds is primarily performed using MC simulation. Hence, precise MC simulations are crucial. The accuracy of MC simulation varies, with $t\bar{t}W$, $t\bar{t}(Z/\gamma^*)$ and VV production being particularly challenging, requiring additional data-driven techniques to adjust their normalization and improve modeling precision. For all irreducible backgrounds, potential mismodeling is addressed by a proper treatment of systematic uncertainties, described in detail in Chapter 8.2.1.

$t\bar{t}W$ is the dominant background within this analysis and is known to be mismodeled in MC simulation. Hence, the $t\bar{t}W$ processes is treated with great care and uses the largest set of systematic uncertainties, covering generator modeling, parton showering, scale and PDF uncertainties. As explained in Section 5.2.2, the QCD and EW contributions to $t\bar{t}W$ were simulated separately. Additionally, the systematic uncertainties are treated separately as well. The normalization of $t\bar{t}W$ QCD is left freely floating and is determined via the data within the likelihood fit. The first two bins of each of the four SRs act as a $t\bar{t}W$ CR as these bins are used to constrain its normalization. The first SR bins are enriched in $t\bar{t}W$ events and contain barely any signal events, as shown in Figure 7.12.

To improve the estimation of the other irreducible backgrounds, dedicated CRs have been established for $t\bar{t}(Z/\gamma^*)$ and VV processes in order to constrain their normalization with data. These regions use stringent selection criteria to isolate the desired backgrounds and minimize contamination from other processes. Events are required to have three charged leptons, consisting of an opposite-sign (OS) lepton pair of the same flavor and an additional lepton. The OS pair must satisfy an invariant mass condition, remaining within 10 GeV of the Z boson mass. The transverse momentum thresholds are set to $p_{\mathrm{T}}(\ell\ell, \mathrm{OS}) > 10\,\mathrm{GeV}$ and $p_{\mathrm{T}}(\ell\ell, \mathrm{SS}) > 20\,\mathrm{GeV}$. Additionally, both same-sign (SS) leptons have to be categorized as M_{inc}, according to the classification outlined in Section 6.4, while the OS lepton has to fulfill the L_{inc} category. For the $t\bar{t}(Z/\gamma^*)$ CR, events must contain at least four jets, whereas the VV CR requires exactly two or three jets. In both CRs, at least one jet must pass the 60 % b-tagging working point (WP), or alternatively, a minimum of two b-tagged jets must meet the 77 % WP requirement.

Using these two CRs, the normalization for these two backgrounds is determined within the upcoming likelihood fit. It should be noted that there is a significant contamination of $t\bar{t}(Z/\gamma^*)$ and Others in the form of tZq in the VV CR. This could be fixed by requiring a stricter selection. Instead, the additional contribution from $t\bar{t}(Z/\gamma^*)$ within the VV CR is used to constrain the $t\bar{t}(Z/\gamma^*)$ even further. Consequently, the Diboson background is slightly worse constrained, but as the $t\bar{t}(Z/\gamma^*)$ is contributing significantly more to the total background within the SRs, this trade-off was accepted. Additionally, VV events undergo specific corrections to address discrepancies in jet multiplicity observed between data and MC simulation, following the same approach as in Ref. [119]. These corrections are validated within another VV-enriched region to account for and mitigate potential mismodeling.

7.2.2 Reducible background processes

Reducible backgrounds are characterized in this analysis as events containing at least one misidentified charged lepton or a lepton that originates from non-prompt sources. These backgrounds typically arise from $t\bar{t}$, V+jets and single-top production and are

evaluated through a semi-data-driven strategy. Their contributions are estimated separately for electrons and muons, based on their lepton reconstruction. In addition to the data-driven estimation, several systematic uncertainties are defined to cover potential mismodeling of these background, presented in Chapter 8.2.1.

Seven additional CRs are dedicated to reducible background originating from non-prompt lepton events. Five of these CRs are utilized to estimate the background contribution originating from decays of heavy-flavor quarks, such as b, c, and light hadrons, and are classified into HF CRs. Specifically, there are two HF CRs for electrons (HFe) and three for muons (HFμ). In these HF CRs, only events are selected which fulfill the criteria of at least two jets and a same-charge lepton pair, where each lepton has a $p_{\mathrm{T}} > 20\,\mathrm{GeV}$. Events enter of the HF$\mu$ CRs if the sub-leading lepton is a muon ($\mu\mu + e\mu$), while events where the sub-leading lepton is an electron enter the HFe CRs. Separate CRs are defined according to the lepton categories: namely, TM, MT, and MM. Consequently, three CRs are used for each lepton flavor: *HFe TM*, *HFμ TM*, *HFe MT*, *HFμ MT*, and *HFμ TT*. However, the *HFe MT* region is excluded from the analysis, due to bad agreement between simulation data. Its removal has a negligible effect on the analysis results, as the HF non-prompt lepton backgrounds are well constrained by the remaining five CRs.

To mitigate contributions from $t\bar{t}W$ events in these CRs, the selection criteria are adjusted to include only events with a single b-tagged jet that meets the 77 % WP. Additionally, the transverse mass of the lepton and E_T^{miss} system must satisfy the condition $m_{T,\ell E_T^{\mathrm{miss}}} < 250\,\mathrm{GeV}$, where m_T represents the transverse mass. The sub-leading lepton p_{T} distribution is used in all HF CRs as the distribution in the upcoming likelihood fit. The normalization factors for both non-prompt electrons and non-prompt muons are allowed to float freely in the likelihood fit and will be constrained by the data in these five CRs.

Two additional CRs address backgrounds from lepton events stemming from photon conversions, such as $\gamma/\gamma^* \to e^+e^-$. As these secondary leptons can mimic the signature of prompt leptons from the primary interaction, they contribute to the reducible backgrounds that must be carefully estimated and mitigated. These two CRs are referred to the CR for material photon conversions (CR Mat Conv) and IP photon conversions (CR Int Conv). Both CRs select events with three leptons, requiring an OS lepton pair of identical flavor, each with $p_{\mathrm{T}} > 20\,\mathrm{GeV}$, and a third lepton with $p_{\mathrm{T}} > 10\,\mathrm{GeV}$. The two same-charge leptons must be categorized as M_{inc}, while the OS lepton must conform to L_{inc} criteria. Events featuring b-tagged jets meeting the 77 % WP are excluded. Additionally, the OS pair's invariant mass must be within 10 GeV of the Z boson mass, and the invariant mass of the three-lepton system must satisfy $|m_Z - m_{\ell\ell}| < 10\,\mathrm{GeV}$ and $E_T^{\mathrm{miss}} < 50\,\mathrm{GeV}$. Specific selection criteria are applied to conversion vertices, distinguishing material conversion candidates from IP conversions using variables such as vertex distance from the primary IP and energy-momentum constraints. Specifically, material conversion

candidates are required to have a conversion vertex with a radial distance from the IP of $r > 20\,\text{mm}$ and $0 < m_{\text{trk}-\text{trk,PV}} < 100\,\text{MeV}$. In contrast, IP conversion candidates must be rejected as material conversion candidates by not fulfilling the previous requirement and must additionally satisfy $0 < m_{\text{trk}-\text{trk,PV}} < 100\,\text{MeV}$.

Another source of reducible non-prompt lepton background arises from leptons with an incorrectly assigned charge. This background is particularly relevant for the 2ℓ regions in this analysis and is referred to as charge misidentification (QMisID). QMisID events mainly originate from the $t\bar{t}$ process, where one electron undergoes hard bremsstrahlung followed by an asymmetric conversion ($e^{\pm} \to e^{\pm}\gamma^{*} \to e^{\pm}e^{+}e^{-}$) or from a mismeasured track curvature. Because high-p_{T} electrons are more likely to emit bremsstrahlung and exhibit less curved tracks, the QMisID background is especially pronounced in the high-p_{T} region. Although QMisID events can also occur for muons, this effect is negligible for medium- to high-p_{T} muons. The QMisID background is measured in data by using samples of $Z \to ee$ events reconstructed as either SS or OS electrons pairs. In order to subtract non-Z backgrounds, a sideband method is applied using events outside the Z boson mass window. The QMisID rates are then extracted with a likelihood approach by using the ratio of SS and OS events, considering the possibility that both electron charges are misidentified. The QMisID rates are measured as a function of electron p_{T} and $|\eta|$ and vary from 10^{-5} for low-p_{T} electrons to 10^{-4} for high-p_{T} electrons. In all 2ℓ analysis regions the QMIsID background is then estimated by applying the measured charge misassignment rate to data events thats pass the selection criteria of the respective regions, except that the lepton has to be of the opposite charge.

Another source of reducible non-prompt lepton background arises from leptons with an incorrectly assigned charge. This background is particularly relevant for the 2ℓ regions in this analysis and is referred to as charge misidentification (QMisID). QMisID events mainly originate from the $t\bar{t}$ process, where one electron undergoes hard bremsstrahlung followed by an asymmetric conversion ($e^{\pm} \to e^{\pm}\gamma^{*} \to e^{\pm}e^{+}e^{-}$) or from a mismeasured track curvature. Because high-p_{T} electrons are more likely to emit bremsstrahlung and exhibit less curved tracks, the QMisID background is especially pronounced in the high-p_{T} region. Although similar misidentification can occur for muons, its effect on medium- to high-p_{T} muons is negligible. To quantify this background, we analyze data samples of $Z \to ee$ events, reconstructing electron pairs as SS or OS. A sideband method that uses events outside the Z boson mass window is employed to subtract non-Z backgrounds. QMisID rates are then extracted with a likelihood approach based on the ratio of SS to OS events, while accounting for the possibility that both electron charges are misidentified. These rates are determined as functions of electron p_{T} and $|\eta|$, varying from 10^{-5} for low-p_{T} electrons to 10^{-4} for high-p_{T} electrons. Finally, in all 2ℓ analysis regions, the QMisID background is estimated by applying the measured charge misassignment rates to data events that pass the selection criteria, with the only difference being that the lepton in question is required to have the opposite charge.

7.2.3 Pre-fit control regions

A summary of the selection criteria for the CRs used in the analysis is provided in Tables 7.4 and 7.5. These CRs are essential for estimating the background contributions from irreducible and reducible processes, affecting both the odeling and normalization. The CRs are designed to isolate specific background components, allowing for more precise shape and yield estimates. The pre-fit distributions for these 9 CRs are presented in Figure 7.13 and their corresponding pre-fit yields are shown in the Tables 7.6 and 7.7. Good pre-fit agreement is observed between data and the predicted background in all CRs, despite the fact that some background processes are known to being underestimated in simulation such a $t\bar{t}W$.

	CR HF TM	CR HF MT	CR HF MM
$p_{\mathrm{T}}^{\mathrm{lep}}$ [GeV]		>20	
BDT WPs (same-charge ℓ pair)	TM	MT	MM
N_{jets}		≥2	
$N_{b-\mathrm{tagged\,jets}}$		1 at 77 %	
Total lepton charge		++ or - -	
m_T(all ℓ, $E_{\mathrm{T}}^{\mathrm{miss}}$)		< 250 GeV	-

Table 7.4: Summary of the event selection applied in the dilepton CRs. The TM, MT, and MM regions are each split into a separate region for the muon channel ($\mu\mu + e\mu$) and the electron channel ($\mu e + ee$). The MT $\mu\mu + e\mu$ CR is not used.

	VV CR	$t\bar{t}Z$ CR	CR Int Conv	CR Mat Conv
$p_{\mathrm{T}}^{\mathrm{lep}}$ [GeV]		> 20 (SS pair), > 10 (OS)		
BDT WPs		$M_{\mathrm{inc}}M_{\mathrm{inc}}$ (SS pair) L_{inc} (OS)		
Total charge		±1		
Electron Conv. candidate		-	Int. Conv.	Mat. Conv.
N_{jets}	2 or 3	≥ 4	≥0	
$N_{b-\mathrm{tagged\,jets}}$	1 b-tagged jet at 60 % WP || ≥ 2 b-tagged jets at 77 % WP		0 at 77 %	
$\lvert m_{SFOS} - m_Z \rvert$		< 10 GeV	> 10 GeV	
$\lvert m(\ell\ell\ell) - m_Z \rvert$	-	-	< 10 GeV	

Table 7.5: Summary of the event selection applied in the three-lepton CRs.

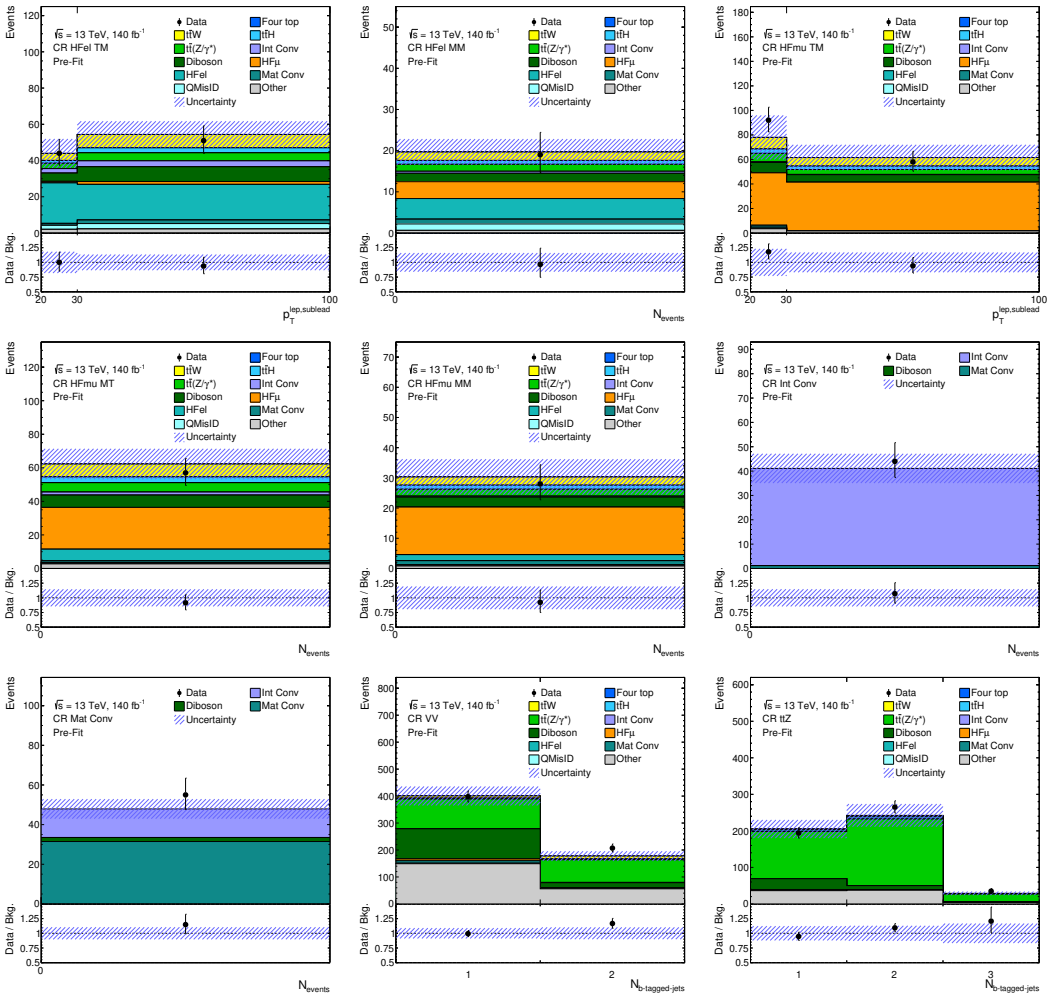

Figure 7.13: Pre-fit distributions for data and the expected background before the likelihood fit in the nine CRs. The predicted pre-fit background is shown as filled histograms. The ratio of the data to the total pre-fit background is shown in the lower panel. The combined statistical and systematic uncertainty in MC simulation is indicated by the hatched band, while the vertical error bars represent the statistical uncertainty in the data.

Table 7.6: Summary of the observed and predicted number of events in the HF Fakes CRs (2ℓSS). The background prediction is shown before the likelihood fit. The individual uncertainties are shown for the different background processes. The uncertainties represent the sum of the statistical and systematic uncertainties.

Process	CR HFμ TM	CR HFμ MT	CR HFμ MM	CR HFe TM	CR HFe MM
$t\bar{t}W$	16.4 ± 2.1	7.64 ± 0.68	2.03 ± 0.30	11.22 ± 0.74	2.03 ± 0.30
$t\bar{t}(Z/\gamma^*)$	10.9 ± 1.9	5.59 ± 0.76	1.69 ± 0.30	7.4 ± 1.5	1.69 ± 0.30
$t\bar{t}H$	6.4 ± 4.4	3.4 ± 2.4	0.95 ± 0.70	4.3 ± 2.8	0.95 ± 0.70
Four top	0.106 ± 0.027	0.072 ± 0.017	0.046 ± 0.012	0.067 ± 0.018	0.0364 ± 0.0089
Diboson	16.3 ± 2.1	7.35 ± 0.74	2.04 ± 0.31	12.75 ± 0.90	2.04 ± 0.31
HFe	1.6 ± 1.0	7.0 ± 2.8	5.0 ± 1.8	42 ± 13	5.0 ± 1.8
HFμ	82 ± 20	24.9 ± 7.6	4.1 ± 1.3	2.4 ± 0.75	4.09 ± 1.30
Mat Conv	1.3 ± 3.6	1.02 ± 0.41	1.16 ± 0.20	3.0 ± 1.5	1.16 ± 0.20
Int Conv	0.65 ± 0.35	1.82 ± 0.96	0.49 ± 0.28	5.7 ± 2.9	0.63 ± 0.17
QMisID	0.26 ± 0.12	0.76 ± 0.55	1.6 ± 1.1	5.2 ± 2.9	1.6 ± 1.1
Others	5.2 ± 1.5	2.73 ± 0.71	0.63 ± 0.17	4.2 ± 1.1	0.63 ± 0.17
Total Background	141 ± 24	62.3 ± 9.0	19.7 ± 3.1	98 ± 15	19.7 ± 3.1
Data	150	57	28	95	19

Table 7.7: Summary of the observed and predicted number of events for the Diboson, ttZ and photon conversion CRs (3ℓ CRs). The background prediction is shown before the likelihood fit. The individual uncertainties are shown for the different background processes. The uncertainties represent the sum of the statistical and systematic uncertainties.

Process	CR Int Conv	CR Mat Conv	CR ttZ	CR VV
$t\bar{t}W$	–	–	6.4 ± 1.0	18.4 ± 1.1
$t\bar{t}(Z/\gamma^*)$	–	–	334 ± 52	194 ± 29
$t\bar{t}H$	–	–	10.8 ± 7.7	6.5 ± 4.7
Four top	–	–	1.60 ± 0.32	0.09 ± 0.03
Diboson	0.036 ± 0.021	2.03 ± 0.25	43.5 ± 4.5	131.4 ± 5.3
HFe	–	–	0.59 ± 0.45	9.7 ± 8.3
HFμ	–	–	1.18 ± 0.43	8.5 ± 2.1
Mat Conv	1.16 ± 0.81	31.5 ± 3.2	0.53 ± 0.33	1.82 ± 0.42
Int Conv	39.9 ± 5.8	14.4 ± 2.3	0.14 ± 0.15	1.75 ± 0.90
QMisID	–	–	0.24 ± 0.19	0.80 ± 0.41
Others	–	–	78 ± 24	205 ± 40
Total Background	41.1 ± 6.0	47.9 ± 4.9	476 ± 59	578 ± 51
Data	44	55	494	605

7.3 Likelihood fit setup

The maximum likelihood fit performed in this analysis is using the RooFit framework [120] with the statistical model implemented in HistFactory format [121]. The likelihood function $\mathcal{L}(\mu, \vec{\lambda}, \vec{\theta})$ is defined as the product of Poisson probability terms for all bins and depends on $\mu, \vec{\lambda}, \vec{\theta}$. The parameter μ is the normalization factor for the signal events. In this specific analysis, μ is a vector that contains the three WCs $c_{tu}^{(1)}$, $c_{Qu}^{(1)}$, $c_{Qu}^{(8)}$. For each WC an EFT parametrization fit is performed in each bin of each SR, more details are provided in Section 7.4. Using this EFT parametrization allows predicting the signal yield for each bin in each SR for any given value for the three WCs. For simplicity, the common non-vector notation for μ is used. The parameter $\vec{\lambda}$ represents the normalization factors for the background processes which are allowed to float freely in the fit and are constrained via their dedicated CRs. The parameter $\vec{\theta}$ represents the systematic uncertainties, which are treated as nuisance parameters (NPs) in the fit. Each NP is linked to a source of systematic uncertainty described in Chapter 8. The NPs $\vec{\theta}$ are modeled as Gaussian constraints with a mean of 0 and a width of 1 and can produce variations in the signal and background predictions. Statistical uncertainties, due to the limited size of data and simulated samples, are included in the NPs $\vec{\theta}$ as dedicated parameters for each bin for every analysis region separately and are referred to as MC statistical parameters. The likelihood function for an analysis region is given as:

$$\mathcal{L}(\mu, \vec{\lambda}, \vec{\theta}) = \prod_{i=1}^{N} \frac{\left(\mu s_i(\vec{\theta}) + b_i(\vec{\lambda}, \vec{\theta})\right)^{n_i}}{n_i!} e^{-\left(\mu s_i(\vec{\theta}) + b_i(\vec{\lambda}, \vec{\theta})\right)}, \tag{7.4}$$

where n_i are the measured yields for a given bin i and the signal and background yields are denoted as s_i and b_i, respectively. For the CRs only background contributions are assumed, hence μ is set to 0 for the CRs. It was tested if the signal can contribute to the CRs and the results showed that no signal events entered the CRs. Therefore the likelihood function can be simplified by dropping the terms which are multiplied with μ for the CRs as:

$$\mathcal{L}(\vec{\lambda}, \vec{\theta}) = \prod_{j=1}^{M} \frac{b_j(\vec{\lambda}, \vec{\theta})^{m_j}}{m_j!} e^{-b_j(\vec{\lambda}, \vec{\theta})}. \tag{7.5}$$

The complete likelihood function is defined as the product of the likelihood functions for all analysis regions, with all regions sharing the same set of parameters $\vec{\lambda}$ and $\vec{\theta}$. The profile likelihood ratio used to test the signal hypothesis for the signal strength parameter μ is represented by the test statistic q_μ, defined as:

$$q_\mu = -2 \ln \left(\frac{\mathcal{L}\left(\mu, \hat{\vec{\lambda}}_\mu, \hat{\vec{\theta}}_\mu\right)}{\mathcal{L}\left(\hat{\mu}, \hat{\vec{\lambda}}_{\hat{\mu}}, \hat{\vec{\theta}}_{\hat{\mu}}\right)} \right), \tag{7.6}$$

where the $\hat{\mu}, \hat{\vec{\lambda}}_{\hat{\mu}}, \hat{\vec{\theta}}_{\hat{\mu}}$ parameters maximize the likelihood, while $\hat{\vec{\lambda}}_\mu, \hat{\vec{\theta}}_\mu$ maximize the likelihood for a given μ value.

To reduce the computational cost of the profile likelihood fit, a pruning procedure is applied to all nuisance parameters. Pruning involves removing those parameters that have a negligible impact on the fit. In this analysis, the impact of each parameter is measured by the deviation induced in the distributions across each analysis region. A parameter is removed from the fit if its induced deviation is below a threshold of 1 %. The effects on shape and normalization are evaluated separately, allowing a parameter to exceed the threshold for one effect while remaining below it for the other. In addition, a cross-check is performed by running the fit without any pruning to confirm that the procedure does not alter the final results.

In the likelihood fit the mean and width of each NP are allowed to change. This flexibility permits the fit to adjust systematic uncertainties by shifting the parameters from their nominal values and modifying their uncertainties based on the data. The *pull* quantifies the shift of a parameter's mean relative to its initial uncertainty, so a *pull* of +0.5 indicates a 0.5σ deviation from the nominal value. The *constraint* reflects how the data have modified the parameter's uncertainty. A reduction in the width shows that the data have provided additional information and tightened the uncertainty, while an increase indicates that the data have loosened the prior assumption about it. Figure 7.14a shows how the Gaussian constraints of NP might change within a fit. In contrast, Figure 7.14b illustrates how these changes in the NP affect an example analysis region used in the fit. In this example, the systematic uncertainty is increased to cover the discrepancy between the simulation and the observed data, as reflected by both a shift in the mean and an increase in the width of the NP.

In this analysis, three different maximum likelihood fits are performed. The normalization factors of the following background processes allowed to freely float in the upcoming three fits: $t\bar{t}W$ QCD, $t\bar{t}Z$, Diboson, HFμ, HFe, Mat Conv and Int Conv. The first fit is a background-only fit to all CRs and the first two bins of the SRs and is presented in Section 9.1. The first two bins of the signal regions are used for the background-only fit because they serve as a $t\bar{t}W$ CR used to constrain the normalization of $t\bar{t}W$ QCD. This fit is performed to validate the fit setup and the background estimation strategy within the SRs. The results of this fit are used to create an Asimov dataset [122] following the background-only hypothesis for the SRs in the second fit. An Asimov dataset is a synthetic set of data in which the event counts in each bin are fixed to their expected values, in this case following

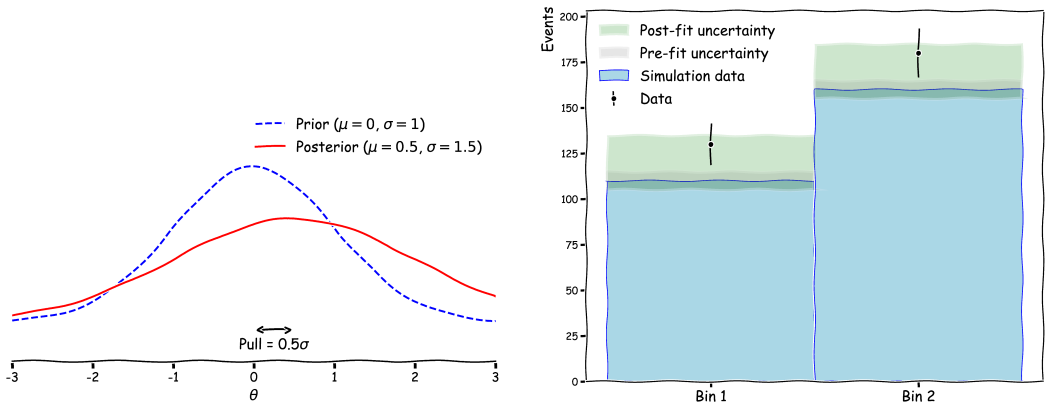

(a) Prior and posterior for a NP

(b) Example region with two bins

Figure 7.14: Illustration of pulls and constraints on nuisance parameters.

the background-only fit results. Asimov datasets are commonly used to estimate the expected sensitivity of a given analysis. The second fit is in this analysis makes use of an Asimov dataset, but only for the SRs. Hence, the fit is referred to as the hybrid-Asimov fit, as data is used for all nine CRs while for the SR an Asimov dataset is used. The hybrid-Asimov fit is shown in Section 9.2 and is performed over the nine CRs and four SRs, using all four bins of each SR. This fit is used to evaluate the expected limits on the WCs and the expected cross-section limit. The third and final fit is the data fit to all analysis regions under the signal+background hypothesis and is presented in Section 9.3. This fit is used to derive the observed WC limits and cross-section limits.

7.4 EFT parametrization in the signal regions

For the maximum likelihood fit, the signal strength parameter μ is parametrized by the three WCs $c_{tu}^{(1)}$, $c_{Qu}^{(1)}$, $c_{Qu}^{(8)}$. In order to be able to predict the signal yield for each bin in all four SRs for any given value of the three WCs, a EFT parametrization is performed. However, the framework used to perform the maximum likelihood fit requires an SM signal sample in order to function properly. Due to the fact that same-charge top-pair production is strongly suppressed in the SM, no SM signal sample is available for this process. The SM signal sample is needed as the following equation is used for the parametrization:

$$N_{\text{bin}} = N_{\text{SM}} + N_{\text{SM}} \cdot \sum_i (A_i \cdot c_i^2), \tag{7.7}$$

where N_{bin} represents the number of events in a given SR bin, N_{SM} is the number of events from SM signal sample for that bin, A_i is the fitted EFT parametrization parameter and c_i is the WC value for the WC i. If no SM signal sample is provided, N_{SM} is 0 and as a consequence the full equation vanishes as the EFT contribution is multiplied with the SM contribution. Therefore, a workaround is used to be able to perform the EFT parametrization, by creating an SM "dummy" signal sample. The dummy sample is created so that it contains a single event for each bin in each SR. In order to minimize the impact of the dummy sample on the fit, each event is assigned an MC weight of 0.0001. However, as this would distort the EFT contribution by a factor of 0.0001, the EFT contribution is scaled by 10^4 to compensate for the MC weight.

To incorporate signal systematics in the maximum likelihood fit, the systematic uncertainties on the signal have to be propagated to the SM dummy sample, as the used framework does not allow defining systematic on EFT samples. The signal systematics were propagated by analyzing the relative impact of each in this analysis considered signal systematic for the default EFT signal sample, with the following WC configuration: $c_{tu}^{(1)} = 0.04$, $c_{Qu}^{(1)} = 0.1$, $c_{Qu}^{(8)} = 0.1$. The relative impact of each systematic is then used to create the systematic variations for the SM dummy sample, by adjusting the MC weight by the relative impact of the given systematic. This whole procedure is validated afterward by comparing the relative impact of each uncertainty between the SM dummy sample and the default EFT signal sample.

Using this technical workaround allows performing the EFT parametrization even though there is no valid SM signal sample available. For the EFT parametrization fit all 32 available EFT samples are used, and the parametrization is performed separately for each bin in each SR. For the EFT parametrization fit the following parametrization is assumed:

$$\sigma_{\text{EFT}} = \frac{1}{\Lambda^4}[A \cdot (c_{tu}^{(1)})^2 + B \cdot (c_{Qu}^{(1)})^2 + C \cdot (c_{Qu}^{(8)})^2 + D \cdot (c_{Qu}^{(1)} \cdot c_{Qu}^{(8)})]. \tag{7.8}$$

The assumed parametrization consists out of three quadratic terms, one for each WC and one interference term for the WCs $c_{Qu}^{(1)}$ and $c_{Qu}^{(8)}$. The two other possible interference terms are expected to be negligible due to the different chirality of $\mathcal{O}_{tu}^{(1)}$ compared to $\mathcal{O}_{Qu}^{(1)}$ and $\mathcal{O}_{Qu}^{(8)}$. The fit is performed by using the predicted cross-section σ for each SR bin from the simulated EFT sample for a given WC configuration. The parametrization fits are shown in Figure 7.15 and Figure 7.16 for the ++ and −− SRs, respectively. The grey dots in the plots corresponds to EFT samples where the other WCs are not 0. The fitted parameters for each WCs per bin per SRs in shown in Table 7.8.

It should be noted that this purely quadratic EFT parametrization only allows for positive signal yields, as by definition the equation can not yield negative values of

parameters as the parameters A, B and C are only allowed to be positive. However, the interference term with the parameter D can introduce destructive interference, which can lead to negative signal yields. But, as the total yield is dominated by the three previous terms, no negative signal yields can be reached.

Fit parameter	$\mathbf{A}(c_{tu}^{(1)})^2$	$\mathbf{B}(c_{Qu}^{(1)})^2$	$\mathbf{C}(c_{Qu}^{(8)})^2$	$\mathbf{D}(c_{Qu}^{(1)} \cdot c_{Qu}^{(8)})$
SR_{ctu++} bin0	$4.58 \cdot 10^7$	$4.22 \cdot 10^6$	$1.17 \cdot 10^6$	$-1.37 \cdot 10^6$
SR_{ctu++} bin1	$6.92 \cdot 10^7$	$5.48 \cdot 10^6$	$1.42 \cdot 10^6$	$-1.22 \cdot 10^6$
SR_{ctu++} bin2	$1.18 \cdot 10^8$	$8.68 \cdot 10^6$	$2.17 \cdot 10^6$	$-1.46 \cdot 10^6$
SR_{ctu++} bin3	$6.71 \cdot 10^8$	$4.38 \cdot 10^7$	$1.04 \cdot 10^7$	$-3.99 \cdot 10^6$
SR_{cQu++} bin0	$1.27 \cdot 10^7$	$2.04 \cdot 10^6$	$5.13 \cdot 10^5$	$-3.51 \cdot 10^5$
SR_{cQu++} bin1	$2.14 \cdot 10^7$	$3.62 \cdot 10^6$	$8.79 \cdot 10^5$	$-4.39 \cdot 10^5$
SR_{cQu++} bin2	$3.91 \cdot 10^7$	$6.80 \cdot 10^6$	$1.61 \cdot 10^6$	$-5.95 \cdot 10^5$
SR_{cQu++} bin3	$3.51 \cdot 10^8$	$6.82 \cdot 10^7$	$1.55 \cdot 10^7$	$-2.23 \cdot 10^6$
SR_{ctu--} bin0	$2.53 \cdot 10^6$	$2.16 \cdot 10^5$	$6.44 \cdot 10^4$	$-9.75 \cdot 10^4$
SR_{ctu--} bin1	$4.99 \cdot 10^6$	$3.53 \cdot 10^5$	$9.91 \cdot 10^4$	$-1.24 \cdot 10^5$
SR_{ctu--} bin2	$8.70 \cdot 10^6$	$5.61 \cdot 10^5$	$1.51 \cdot 10^5$	$-1.59 \cdot 10^5$
SR_{ctu--} bin3	$2.56 \cdot 10^7$	$1.55 \cdot 10^6$	$3.94 \cdot 10^5$	$-2.92 \cdot 10^5$
SR_{cQu--} bin0	$5.58 \cdot 10^5$	$7.18 \cdot 10^4$	$1.91 \cdot 10^4$	$-1.88 \cdot 10^4$
SR_{cQu--} bin1	$1.09 \cdot 10^6$	$1.40 \cdot 10^5$	$3.55 \cdot 10^4$	$-2.67 \cdot 10^4$
SR_{cQu--} bin2	$2.09 \cdot 10^6$	$2.80 \cdot 10^5$	$6.84 \cdot 10^4$	$-3.73 \cdot 10^4$
SR_{cQu--} bin3	$8.66 \cdot 10^6$	$1.34 \cdot 10^6$	$3.14 \cdot 10^5$	$-9.82 \cdot 10^4$

Table 7.8: Fitted EFT parametrization for equation 7.8 for each bin of the four SRs: SR_{ctu++}, SR_{ctu--}, SR_{cQu++} and SR_{cQu--}.

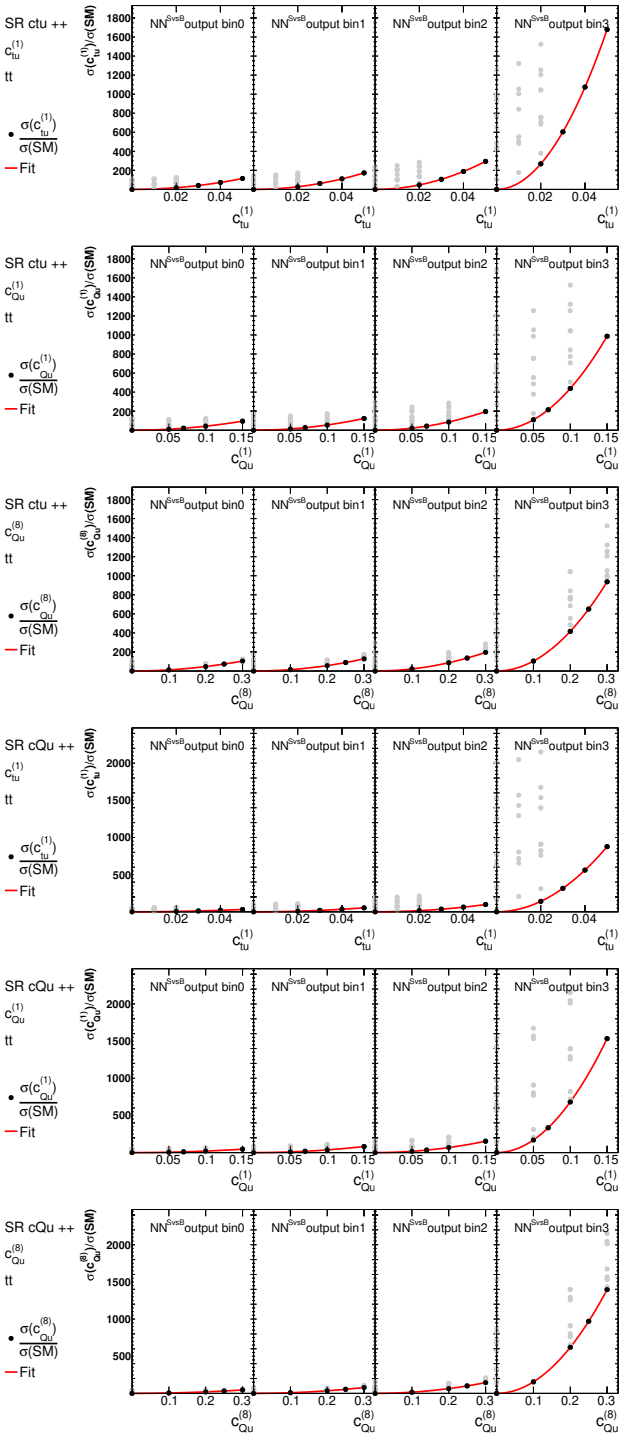

Figure 7.15: EFT parametrization fit for the SR_{ctu++} and the SR_{cQu++} for the three WCs $c_{tu}^{(1)}$, $c_{Qu}^{(1)}$, $c_{Qu}^{(8)}$. For the parametrization fits all 32 available EFT samples were used. The grey dots corresponds to EFT samples where the other WCs are not 0.

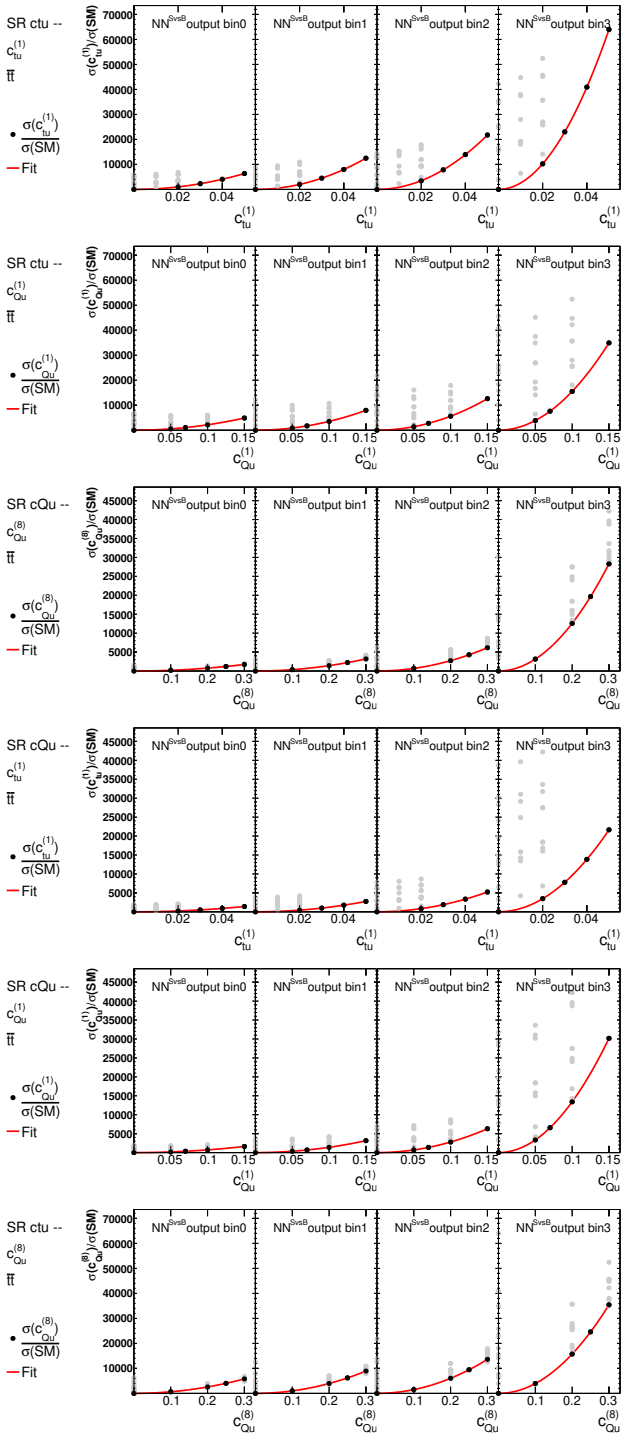

Figure 7.16: EFT parametrization fit for the $\mathrm{SR}_{\mathrm{ctu}--}$ and the $\mathrm{SR}_{\mathrm{cQu}--}$ for the three WCs $c_{tu}^{(1)}$, $c_{Qu}^{(1)}$, $c_{Qu}^{(8)}$. For the parametrization fits all 32 available EFT samples were used. The grey dots corresponds to EFT samples where the other WCs are not 0.

8 Systematic uncertainties

Several systematic uncertainties are considered in this analysis to take into account the imperfect modeling of the physics processes and of the detector response. Systematic uncertainties affect the signal and background events acceptance and selection efficiencies in the signal, validation and control regions, but also the shape of the kinematic distributions and therefore also the DNN^{SvsB} output distributions.

The systematic uncertainties are divided into three categories for this analysis. The first category includes all experimental uncertainties and is described in Section 8.1. The experimental uncertainties represent the uncertainties in the reconstruction of the physics objects that are used in this analysis, namely jets, b-tagged jets, leptons and $E_{\text{T}}^{\text{miss}}$.

The second category contains the modeling uncertainties, which are estimated by comparing different MC generators, parton shower algorithms, and hadronization models. Additionally, uncertainties are derived by comparing MC samples with different simulation settings, such as the renormalization μ_{R}, the factorization scale μ_{R}, or the choice of PDFs. The modeling uncertainties are presented separately for the irreducible background processes and the reducible non-prompt lepton backgrounds in Section 8.2 in their respective subsections.

All of these systematic uncertainties are incorporated in the likelihood function as NPs. Each systematic uncertainty is described by one or multiple NPs. The pre-fit mean values and standard deviations of the experimental uncertainties are provided by dedicated studies from the ATLAS Collaboration performance groups. The maximum-likelihood fit used to determine the best estimate the best set of fit parameters, including all NPs and NFs.

All systematic uncertainties in this analysis are smoothed with the *MaxVariation* algorithm. The MaxVariation smoothing algorithm reduces statistical fluctuations in histograms by iteratively minimizing the largest variations between neighboring bins while preserving the overall distribution shape. At each step, bin contents are adjusted to reduce large differences, ensuring that the underlying shape remain intact. The process stops when variations fall below a predefined threshold, which is set to 40 % for this analysis.

Additionally, all systematic uncertainties are symmetrized following specific symmetrization methods, depending on the availability of the up- and down-variations. For systematic uncertainties that only have an up- or down-variation, the missing variation is set to the mirrored version of the provided variation. For systematic uncertainties that have both up- and down-variations, the symmetrization is applied by taking the average of the up- and down-variations. Another symmetrization method

is applied to the $t\bar{t}W$ PDF uncertainties, mirroring the larger absolute variation of the up- and down-variations. Lastly, for a few systematic uncertainties that have both up- and down-variations, no symmetrization is applied to keep the exact shape of the systematic uncertainty.

Several systematic uncertainties in this analysis are used as normalization-only uncertainties, meaning that they only affect the normalization of the fitted distributions and not the shape. For normalization-only uncertainty, no symmetrization or smoothing is applied.

In Table 8.1 a summary of all experimental and background modeling uncertainties is given with the associated number of NPs. The applied symmetrization method is indicated in the table using different labels. Sym(2) represents the mirroring of the missing up- or down-variation, Sym(3) corresponds to the averaging of the up- and down-variations, and Sym(Max) denotes the mirroring of the larger absolute variation of the up- and down-variations. For systematic uncertainties without symmetrization applied, the respective column is left empty and normalization-only uncertainties are marked with "(N)".

Systematic uncertainty	Symmetrization	Components
Luminosity (N)		1
Pile-Up reweighting		1
Physics Objects		
Electron	Sym(3)	5
Muon	Sym(3)	12
Jet energy scale	Sym(3)	30
Jet energy resolution	Sym(3)	13
Jet vertex fraction		1
Jet flavour tagging		85
$E_{\mathrm{T}}^{\mathrm{miss}}$	Sym(2/3)	3
Total (Experimental)		151
Non-prompt-lepton backgrounds		
Electron Non-prompt BDT	Sym(2)	14
Muon Non-prompt BDT	Sym(2/3)	20
Mat Conv SR extrapolation (N)		1
Int Conv SR extrapolation (N)		1
QMisID normalization (N)		1
QMisID uncertainty		4
HF$e/\mu$ uncertainties	Sym(2)	10
HF$e/\mu$ SR extrapolation (N)		2
Total (Non-prompt-lepton backgrounds)		53

Systematic uncertainty	Symmetrization	Components
Signal modeling		
Scale uncertainties	Sym(2)	1
Flavour tagging extrapolation	Sym(2)	2
$t\bar{t}W$ **modeling**		
Normalization uncertainty (N)		1
Generator modeling	Sym(2)	2
Parton Showering	Sym(2)	2
Scale uncertainties		2
PDF uncertainties	Sym(Max)	2
$t\bar{t}H$ **modeling**		
Normalization uncertainty (N)		2
Generator modeling	Sym(2)	1
Parton Showering	Sym(2)	1
Scale uncertainties		1
$t\bar{t}Z$ **modeling**		
Parton Showering	Sym(2)	1
Parton Showering Var3c		1
Scale uncertainties		1
Diboson		
Jet multiplicity mismodeling		1
Scale uncertainties		1
Other background modeling		
Normalization uncertainty (N)		8
Total (Modeling)		30
Total (Overall)		234

Table 8.1: Sources of systematic uncertainty considered in the analysis. All uncertainties affect also the shape of the fitted distributions and/or the acceptance in the fit categories, expect NPs marked "(N)" which indicates that only the normalization is affected. Some systematic uncertainties are split into several components, as indicated by the number in the rightmost column.

8.1 Experimental uncertainties

Several experimental uncertainties are considered in this analysis to account for the imperfect object reconstruction, identification and calibration, as well as the detector response and resolution.

Starting with the luminosity uncertainty, it was found to have an uncertainty of 0.83 % [45] and was determined using the LUCID-2 detector [123] by performing van-der-Meer scans. This uncertainty is applied to all simulated samples and is considered as a normalization uncertainty. The MC samples are reweighted to reproduce the observed pileup distribution in the data. The pileup-related uncertainty is derived by varying the reweighting factors, ensuring the difference between the theoretical predictions and measured data is captured [124].

Experimental uncertainties to account for differences between simulated and data events in the reconstruction, identification, calibration, trigger, and isolation efficiencies for electrons and muons are applied as scale factors to simulations. The scale factors and their corresponding systematic uncertainties are derived by the ATLAS performance groups in $Z \to ee(\mu\mu)$ and $J/\psi \to ee(\mu\mu)$ [101, 102, 125, 126]. The scale factors are evaluated for electrons and muons separately as a function of the transverse momentum p_{T} or the pseudorapidity η using tag-and-probe techniques.

Uncertainties for the reconstruction of E_T^{miss} are also considered. Since for the reconstruction of E_T^{miss} all reconstructed objects are used, the corresponding uncertainties on the objects are propagated to the estimation of the $E_{\mathrm{T}}^{\mathrm{miss}}$. Additionally, uncertainties for the soft term of $E_{\mathrm{T}}^{\mathrm{miss}}$ are considered, by comparing the measured soft terms in data and simulation. These uncertainties are implemented as three separate NPs [108], where one NP describes the scale uncertainty on $E_{\mathrm{T}}^{\mathrm{miss}}$ and the other two NP resolution uncertainty parallel and perpendicular to $E_{\mathrm{T}}^{\mathrm{miss}}$.

The jet energy scale (JES) is calibrated using a combination of test beam data, simulations, and in-situ methods [107]. The associated uncertainty involves 30 independent components, addressing factors like pileup modeling, jet flavor composition and response, and differences between jets originating from b-quarks or gluons and those outside the calorimeter. The uncertainty in jet energy resolution (JER) is evaluated by smearing the resolution of either the simulation or data to match the lower resolution between the two. The JER uncertainty is characterized through 13 orthogonal components, in different bins of p_{T} and η [107]. Uncertainties related to the jet vertex tagger (JVT) efficiency are derived from $Z(\to \mu^+\mu^-)$+jets events [127].

The b-tagging efficiency of true b-jets and the mistagging rates for light-flavor and c-jets are also sources of uncertainty. The b-tagging efficiencies are measured in dileptonic $t\bar{t}$ events as functions of jet p_{T}, and discrepancies between simulation and

data are corrected using scale factors. The uncertainty associated with these scale factors is distributed across 45 distinct components [128]. The mistagging probability for c-jets as b-jets is evaluated in semileptonic $t\bar{t}$ events where a W-boson decays to a c-quark and a light-flavor quark [129]. The rate is expressed as a function of jet p_{T}, with an overall uncertainty between 3 % and 17 %, divided into 20 components. Similarly, the mistagging rate for light-flavor jets is broken into 20 NPs. The uncertainties are represented by scale factors that are obtained through techniques described in Ref. [130].

8.2 Modeling uncertainties

There are numerous uncertainties in the modeling of background processes that are considered in the analysis.

Starting with the normalization uncertainties, for both the reducible and irreducible backgrounds. Global normalization uncertainties are included for all processes without free-floating normalization factors, following the measured cross-section uncertainties by other measurements or using conservative estimates. As a reminder, the normalization factors of the following processes allowed to freely float in the fit: $t\bar{t}W$ QCD, $t\bar{t}Z$, diboson, HFμ, HFe, Mat Conv and Int Conv.

A 20 % uncertainty is applied to the NLO EW diagrams contributing to $t\bar{t}W$ [131], as only the QCD component of $t\bar{t}W$ is free-floating in the fit. For $t\bar{t}t\bar{t}$, $t\bar{t}H$, and tZ processes, normalization uncertainties of 20 % [132], 11 % [80], and 20 % [133] are assigned, respectively. Additionally, 50 % normalization uncertainties are assigned to tZ, $t\bar{t}H$ and $t\bar{t}$ events containing additional heavy-flavor jets [134]. These additional normalization uncertainties are taken into account, as the modeling of processes with additional heavy-flavor jets is challenging and known to exhibit inaccuracies. All other minor irreducible background processes, which are grouped in *Others* are assigned a conservative 50 % normalization uncertainty. No normalization uncertainties are considered for $t\bar{t}$, single-top-quark, Z+jets and W+jets production, as all of these processes exclusively contribute to the reducible non-prompt lepton backgrounds, HFμ, HFe, Mat Conv and Int Conv which are free-floating in the fit. For the purely data-driven QmisID background, a normalization uncertainty of 20 % is applied, to cover potential shortcomings in the data-driven approach.

8.2.1 Irreducible background modeling uncertainties

Primarily for the dominant irreducible background processes, additional modeling uncertainties are introduced, utilizing the alternative samples specified in parentheses in Table 5.1. These comparisons across different generator configurations

account for acceptance effects, event category migrations, and impacts on kinematic distributions. The generator choice contributes as a systematic uncertainty for $t\bar{t}W$ and $t\bar{t}H$. In the case of $t\bar{t}W$ production, this uncertainty is assessed by comparing the default Sherpa 2.2.10 sample to alternative samples generated using MadGraph5_aMC@NLO with Pythia 8. For $t\bar{t}H$, the default Powheg Box sample is compared against an alternative MadGraph5_aMC@NLO sample interfaced to Pythia 8.

Uncertainties in PS and hadronization modeling are also considered for $t\bar{t}W$, $t\bar{t}H$, and $t\bar{t}Z$. In the case of $t\bar{t}H$ and $t\bar{t}Z$, these uncertainties are estimated by comparing the default samples with alternatives where the ME generators use Herwig 7 instead of Pythia 8. For $t\bar{t}W$ production, two distinct alternative samples provide the comparison: one where the matrix element is interfaced with Pythia 8 and another with Herwig 7. The relative variations between these samples are calculated across all bins of the analysis and then applied to the default Sherpa 2.2.10 $t\bar{t}W$ sample.

The uncertainties arising from variations in the factorization scale μ_{F} and renormalization scale μ_{R} for matrix element calculations are also evaluated for the $t\bar{t}H$, $t\bar{t}W$, $t\bar{t}Z$, and VV processes. These scales are varied independently by factors of 0.5 and 2.0. For $t\bar{t}W$, separate scale uncertainties are computed for the QCD and EW components.

For the signal samples, the impact of μ_{F} and μ_{R} variations is calculated at the generator level. This is then propagated to the NN-output distributions in the SRs, resulting in shape uncertainties that vary between 2 % and 25 %, depending on the SR and NN-output bin. Additionally, high-p_{T} flavour tagging extrapolation uncertainties are applied to the signal samples separately in the form of two NPs, one for b/c-tagging and one for light-jet tagging.

Uncertainties from initial-state radiation are considered for $t\bar{t}Z$ events by applying the Var3c variation of the A14 tune [58] to $\alpha_{\mathrm{s}}^{\mathrm{ISR}}$. For $t\bar{t}W$, additional uncertainties from PDFs are included. The first is derived by comparing the nominal PDF with $\alpha_{\mathrm{s}} = 0.118$ to variations using $\alpha_{\mathrm{s}} = 0.117$ and $\alpha_{\mathrm{s}} = 0.119$. The second is based on comparisons of the nominal PDF set NNPDF3.0nlo with alternative sets such as CT14nnlo [135] and MMHT2014nnlo68cl [61]. Lastly, the statistical uncertainty on the fitted parameters for the diboson jet-multiplicity correction is considered as an additional uncertainty [119].

Table 8.2 summarizes the uncertainties associated with the normalization, generator configurations, parton showering, and scale choices for the different background processes, for the irreducible backgrounds, excluding the non-prompt lepton backgrounds which are discussed in more detail in the next section.

Process	Normalization uncertainty	Generator (alternative)	Parton Shower (alternative)	Scale variations
$t\bar{t}W$ QCD	–	MadGraph5_aMC@NLO + Pythia 8 with FxFx merging scheme Powheg+Pythia8 vs Powheg+Herwig7		✓
$t\bar{t}W$ EW	± 20 %	MadGraph5_aMC@NLO + Pythia 8 Powheg+Pythia8 vs Powheg+Herwig7		✓
$t\bar{t}Z$	–	–	MG5 + Herwig 7.1.3	✓
$t\bar{t}H$	± 11 % (± 50 %)	MadGraph5_aMC@NLO + Pythia 8	Powheg+Herwig 7.1.3	✓
Diboson	–	–	–	✓
Four top	± 20 %	–	–	–
tZ	± 20 % (± 50 %)	–	–	–
Others	± 50 %	–	–	–

Table 8.2: Summary of modeling uncertainties for the MC predictions for different processes. The normalization factors for $t\bar{t}W$, $t\bar{t}Z$, and Diboson are all freely floating and determined via CRs and therefore do not have normalization uncertainty. The normalization uncertainties given in parentheses are related only to events with additional heavy-flavor jets.

8.2.2 Reducible background modeling uncertainties

The reducible non-prompt lepton backgrounds are mostly estimated using data-driven techniques in this analysis, by having the NFs freely floating for HFμ, HFe, Mat Conv and Int Conv. However, the estimation of these background also rely significantly on the used non-prompt lepton BDT. Consequently, mismodeling in the BDT input variables used for the training and differences between the BDT WPs are sources of systematic uncertainties are considered in the upcoming statistical analysis.

Starting with the uncertainties that arise due to the imperfect modeling of the variables used in the non-prompt lepton BDT. To address this, systematic uncertainties are introduced based on discrepancies observed between data and simulation for the BDT input variables. These uncertainties are modeled as 34 NPs that only affect the shape of the distributions without altering their normalization and are provided by the ATLAS performance groups. Furthermore, five NPs are included for HFμ, HFe, to account for shape differences in the five most important BDT input variables distributions between the M and T BDT WPs.

Additional uncertainties are included to account for potential differences in the efficiencies of the non-prompt lepton BDT WPs when alternative simulations are used. For the M and T BDT WPs, these uncertainties are estimated by comparing efficiencies derived from the nominal Powheg+Pythia 8 $t\bar{t}$ simulation against those from alternative $t\bar{t}$ simulations, either Herwig 7 or Sherpa 2.2.10, as functions of the lepton p_{T}. This results in the assignment of a 20 % normalization uncertainty to both HFe and HFμ in the SRs, referred to as HF$e/\mu$ SR extrapolation.

To account for possible discrepancies between data and simulation in the rate of photon conversions, additional uncertainties are incorporated. These uncertainties

are derived by comparing photon conversion rates in data and simulation within dedicated 2ℓ validation regions, which require two T same-charge leptons, one of which is identified as a conversion candidate. Interaction-based and material-based photon conversion extrapolation uncertainties of 50 % and 10 %, respectively, are assigned to the conversion rates in the SRs.

Systematic uncertainties are also assigned to the data-driven QMisID background process, with four uncertainties contributing to the overall uncertainty. These include differences in rates between misidentified electrons and positrons, as well as variations in the charge misidentification rates within the m_Z window. Additionally, they encompass discrepancies between rates obtained using the likelihood method and those derived from matching reconstructed to generated $Z \to e^+e^-$ events in simulation, along with statistical uncertainties associated with the likelihood method. The total uncertainty varies with kinematic properties, increasing as a function of the electron p_{T} while decreasing with $|\eta|$, and ranges between 10 % and 60 %. This uncertainty is calculated and implemented as four separate NPs for the analysis regions that require *MM*, *MT*, *TM* and *TT* BDT WPs.

9 Results

In the following three sections, the results of this thesis are presented. Three different maximum likelihood fits were performed. The three different fit setups and the general likelihood fit setup are described in detail in Section 7.3. The EFT signal parameterization that is used for the fits including signal is described in Section 7.4.

First, the background-only fit, the hybrid-Asimov fit and the fit to data are shown, followed by Section 9.4, in which the results of the hybrid-Asimov fit and the data fit are used to constrain the WCs and the associated same-charge top-quark pair production cross-section. In the final Section 9.5 of this chapter, the results of this analysis are compared to the previous best limits on the three considered EFT operators derived from other analyses. As the main result of this analysis is the signal+background fit to data, the results of the background-only and hybrid-Asimov fit are only briefly discussed.

9.1 Background-only fit to all CRs and first signal region bins

In order to validate the background estimation strategy of this analysis, a maximum likelihood fit is performed to the data events in the nine CRs and the first two bins of all four SRs. The fit is performed under the background-only hypothesis, where all three WCs are set to 0, while the normalization factors for the background processes $t\bar{t}W$, $t\bar{t}Z$, diboson and the non-prompt lepton backgrounds are free to float. The first two bins of the SRs are included as they serve as a CR for $t\bar{t}W$ and are shown to contain only a negligible amount of signal. Having good control of the $t\bar{t}W$ background is crucial for this analysis, as it is the dominant background in the bins with the highest signal contribution in each SR. Furthermore, in previous measurements of the $t\bar{t}W$ cross-section an excess with respect to the SM theory prediction was found by the ATLAS Collaboration [69] as well as by the CMS Collaboration [136]. Hence, the normalization factor for $t\bar{t}W$ is expected to be larger than the SM prediction. However, the newest NNLO predictions for the $t\bar{t}W$ cross-section [137] decreases the tension between the SM prediction and the measured values, but does not fully resolve it. In order to stay consistent with the latest ATLAS $t\bar{t}W$ cross-section measurement and due to the fact that updating the cross-section prediction does not impact the final result, the SM prediction is not altered in this analysis.

In Figure 9.1 a summary plot of the nine CRs after performing the background-only fit is shown.

The post-fit background predictions are shown as the filled histograms, while the pre-fit background predictions are shown as dashed lines. The bottom panel compares

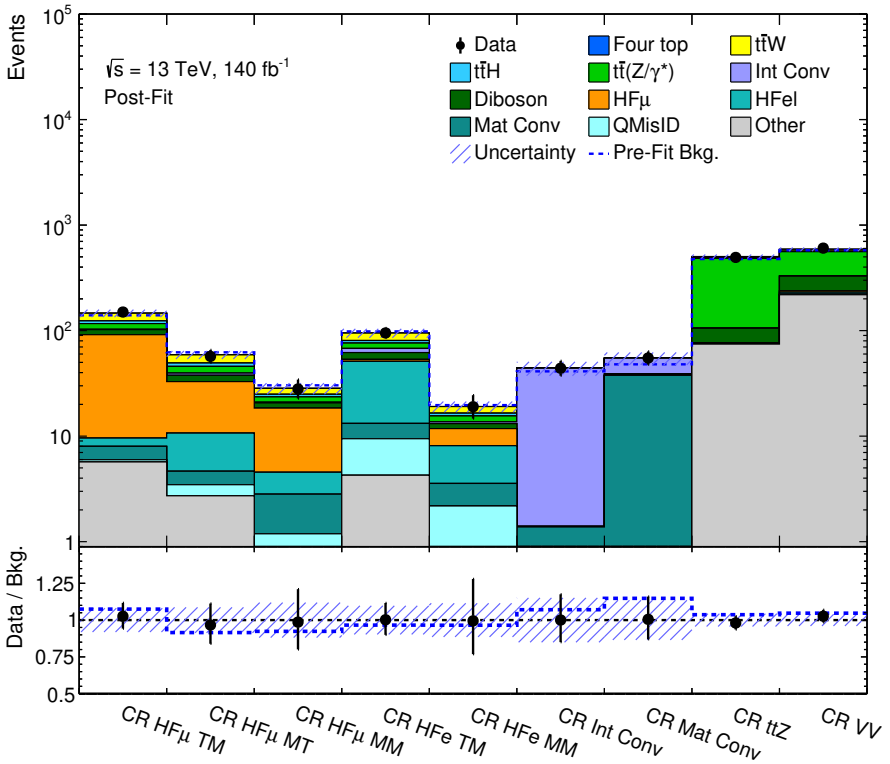

Figure 9.1: Comparison between the event yields in data and the background expectation for the nine CRs after the background-only fit. The post-fit background expectations are shown as filled histograms, the combined pre-fit background expectations are shown as dashed lines. The ratio of the data to the total post-fit background is shown in the lower panel. The combined statistical and systematic uncertainty in the simulation is indicated by the hatched band, while the vertical error bars represent the statistical uncertainty in the data.

the predicted post-fit background with the data. The post-fit background predictions are in very good agreement with the data in all CRs. However, the pre-fit background predictions were already in good agreement with the data within the uncertainties. The fitted normalization factors for the background processes are shown in Figure 9.2. The normalization factors are consistent with the predictions of the SM for all processes, except for $t\bar{t}W$. However, the measured normalization factor for $t\bar{t}W$ is consistent with the found excess from the ATLAS and CMS measurements [69, 136].

The different post-fit distributions for the four CRs with multiple bins are shown separately in Figure 9.3. Good bin-wise agreement between the predicted background and the data is observed in these CRs.

The post-fit distributions of the $\mathrm{NN}^{\mathrm{SvsB}}$ output in the first two bins of the four SRs

are shown in Figure 9.4. The post-fit background predictions are in good agreement with the data for each bin in all four SRs.

Very good agreement between the data and the post-fit background predictions is observed in all CRs and the SRs considered in this fit. This indicates that the background estimation strategy in combination with the set of systematic uncertainties is able to describe the data well. Additional plots for the background-only fit can be found in Appendix B.1, including the post-fit distributions for the VRs, and the pull and constraint plots for the NPs. The effect of pulls and constraints of NPs in the likelihood was explained in Section 7.3. No significant pulls or constraints on the NPs are observed in the fit.

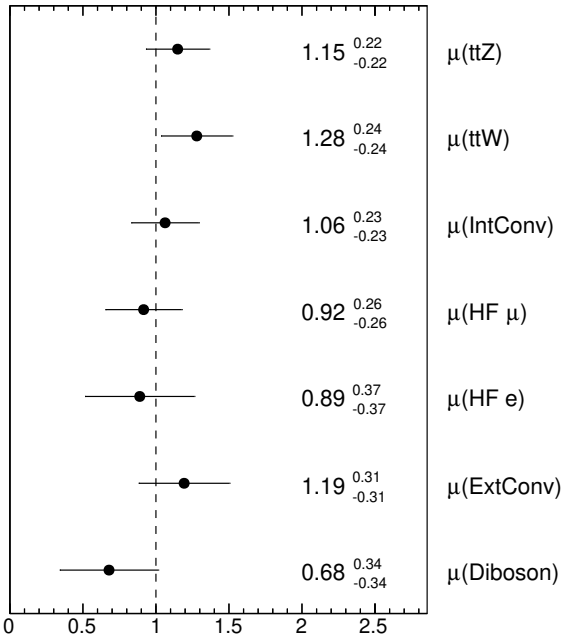

Figure 9.2: Normalization factors for the background processes for the background-only fit to the CRs and first two SR bins with statistical and systematic uncertainties. The deviation for the $t\bar{t}W$ NF is in agreement with the latest cross-section measurements [69, 136].

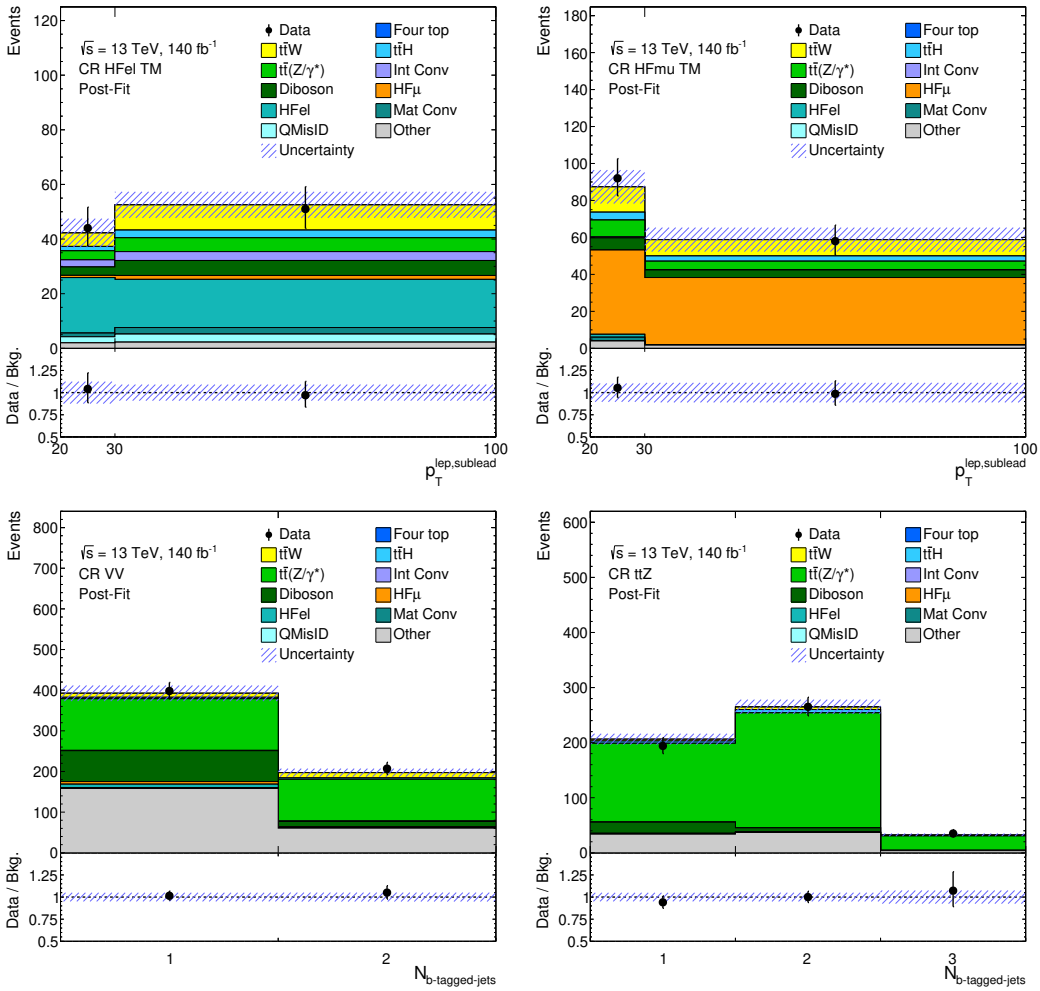

Figure 9.3: Comparison between the event yields in data and the background prediction after the background-only fit for the four multiple-bin CRs. The ratio of the data to the total post-fit background is shown in the lower panel. The combined statistical and systematic uncertainty in the simulation is indicated by the hatched band, while the vertical error bars represent the statistical uncertainty in the data.

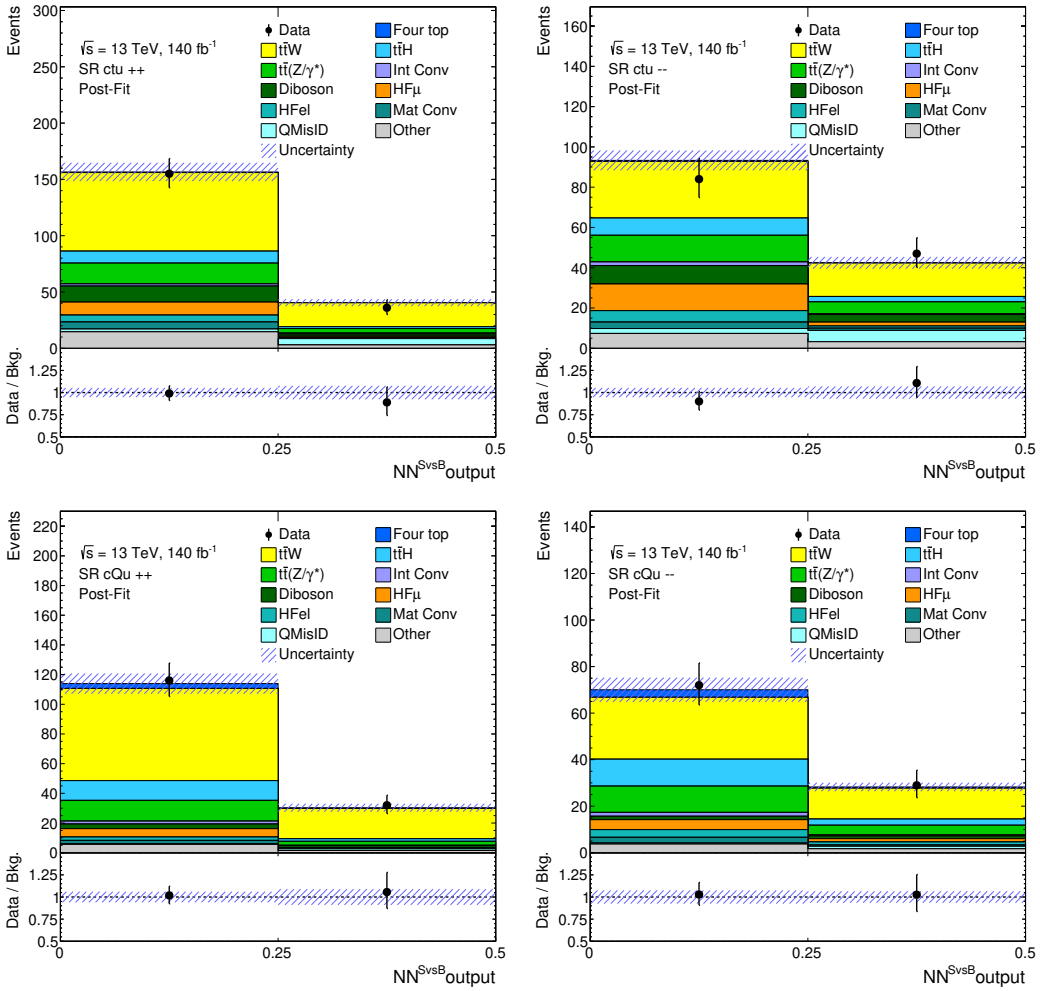

Figure 9.4: Distributions of the $\mathrm{NN}^{\mathrm{SvsB}}$ output for data and the expected background after the background-only fit in the first two bins of the four SRs. The post-fit background expectations are shown as filled histograms, the combined pre-fit background expectations are shown as dashed lines. The ratio of the data to the total post-fit background is shown in the lower panel. The combined statistical and systematic uncertainty in MC simulation is indicated by the hatched band, while the vertical error bars represent the statistical uncertainty in the data.

9.2 Hybrid-Asimov fit to all analysis regions

In the following, the fit is performed under the signal+background assumption but the SR bins are blinded. Instead of data, an Asimov dataset [122] is used for all SR bins that follows the fit results of the background-only fit. For the CRs data is used, and therefore this fit is also referred to as hybrid-Asimov fit, as it only uses an pseudo-data for the SRs. The same normalization factors as for the background-only are free to float, while additionally the WCs are also allowed to vary in this fit. By evaluating the results of this fit, the sensitivity of the analysis to the WCs can be tested and the expected limits on the WCs and the cross-section for same-charge top-quark pair production can be determined.

In Figure 9.5 the normalization factors for the background processes and the fitted WCs values for the hybrid-Asimov fit to all analysis regions are shown. The normalization factors are consistent with the fitted NFs from the previous background-only fit. Since, the post-fit distributions for the CRs barely change, they are not shown for this fit again here. Instead, the CRs and additional figures showing for the constraints and correlations between the NPs can be found in Appendix B.2. It is expected that the NFs for the hybrid-Asimov fit are consistent with the background-only fit, as the Asimov dataset is constructed to follow the background-only fit results. However, by adding additional degrees of freedom in the form of two additional bins per SR and by including signal parameters in the fit, minor changes are also possible.

It should be noted that in this fit the first two bins of each SR are blinded again, which could impact the expected results. Therefore, an alternative fit setup was tested to investigate the impact of this reblinding. For the test setup, each SR was split into two separate regions, one containing the first two bins and the other the last bins. By introducing this split, it was possible to use the data in the first two SR bins, while keeping the last two bins blinded. It was found that the reblinding of the first two SR bins has a negligible impact on the expected limits, and therefore the original fit setup was chosen.

The fitted WC values are consistent with the SM predictions and were fitted close to 0, indicating that a negligible amount of signal was fitted. This is in agreement with the expected behavior, as the hybrid-Asimov dataset is constructed to follow the background-only fit results. In an alternative fit setup, the Asimov dataset was constructed to follow an signal+background hypothesis, where the WCs were set to $c_{tu}^{(1)} = 0.04$, $c_{Qu}^{(1)} = 0.1$, and $c_{Qu}^{(8)} = 0.1$. The fitted WCs were found to be consistent with these values, indicating that the analysis is able to extract the signal contribution from the data.

The post-fit distributions of the $\mathrm{NN}^{\mathrm{SvsB}}$ output for the four SRs are shown in Figure 9.6. As all bins of each SR are blinded, no data is shown in the post-fit distributions and therefore the agreement of the MC predictions can not be evaluated.

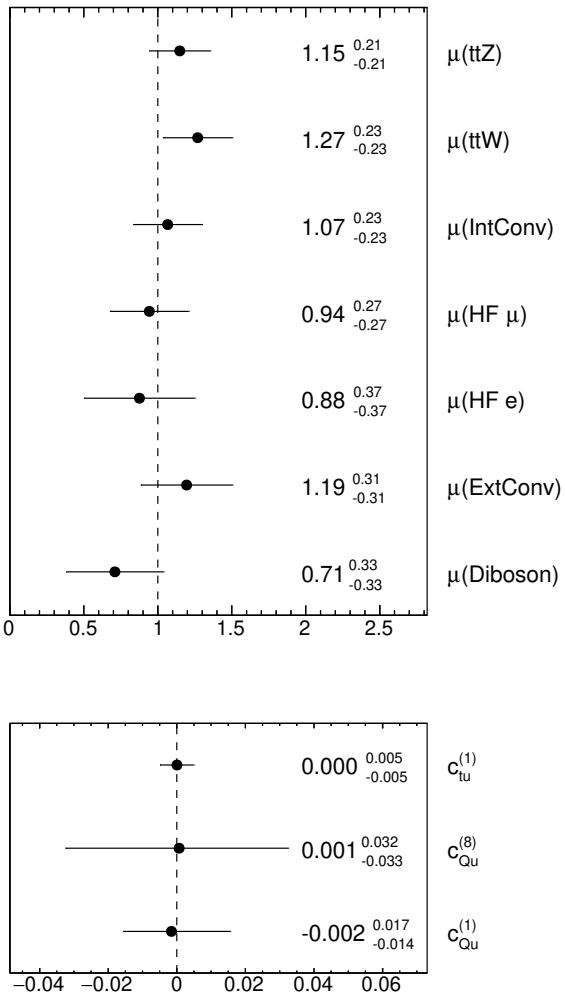

Figure 9.5: Normalization factors for the background processes and the fitted WCs values for the the hybrid-Asimov to all analysis regions with statistical and systematic uncertainties.

Instead, for this fit the post-fit distributions for the VRs are presented in Figure 9.7. The VRs are not included in the fit, but the fitted NPs and NFs are propagated to the VRs. The VRs show decent agreement between data and simulation. Some disagreement in form of statistical fluctuations are observed for the last two bins in the $\mathrm{VR}_{\mathrm{cQu++}}$.

In the upcoming Section 9.4, the results of the hybrid-Asimov fit are used to extract the expected limits on the WCs by performing a likelihood scan over a range of values

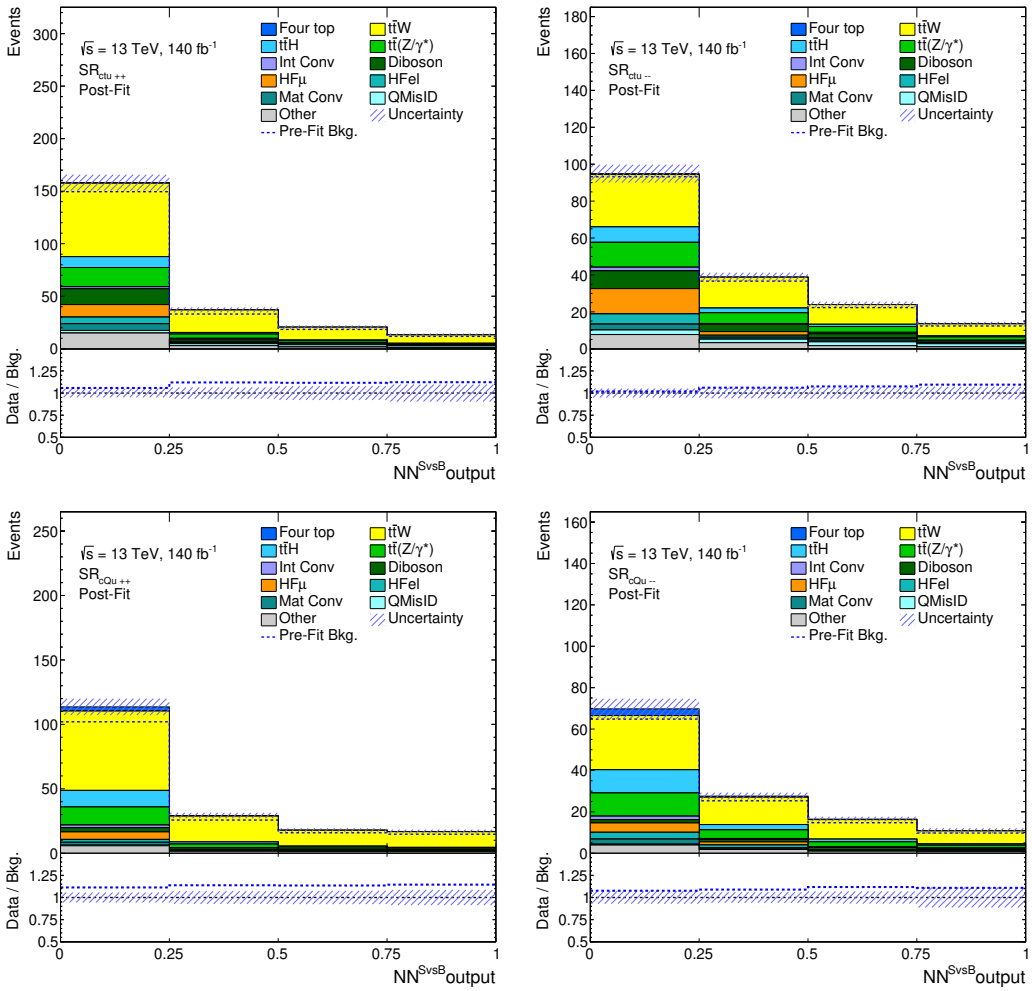

Figure 9.6: Distributions of the $\mathrm{NN}^{\mathrm{SvsB}}$ output in the four SRs the expected background after the hybrid-Asimov fit. The data is blinded in this fit, instead an Asimov dataset is used that follows the fit results of the background-only fit. The post-fit background expectations are shown as filled histograms, the combined pre-fit background expectations are shown as dashed lines. The combined statistical and systematic uncertainty in MC simulation is indicated by the hatched band.

for each WCs separately. The expected limits on the WCs are also used to constrain the production cross-section of same-charge top-quark pairs.

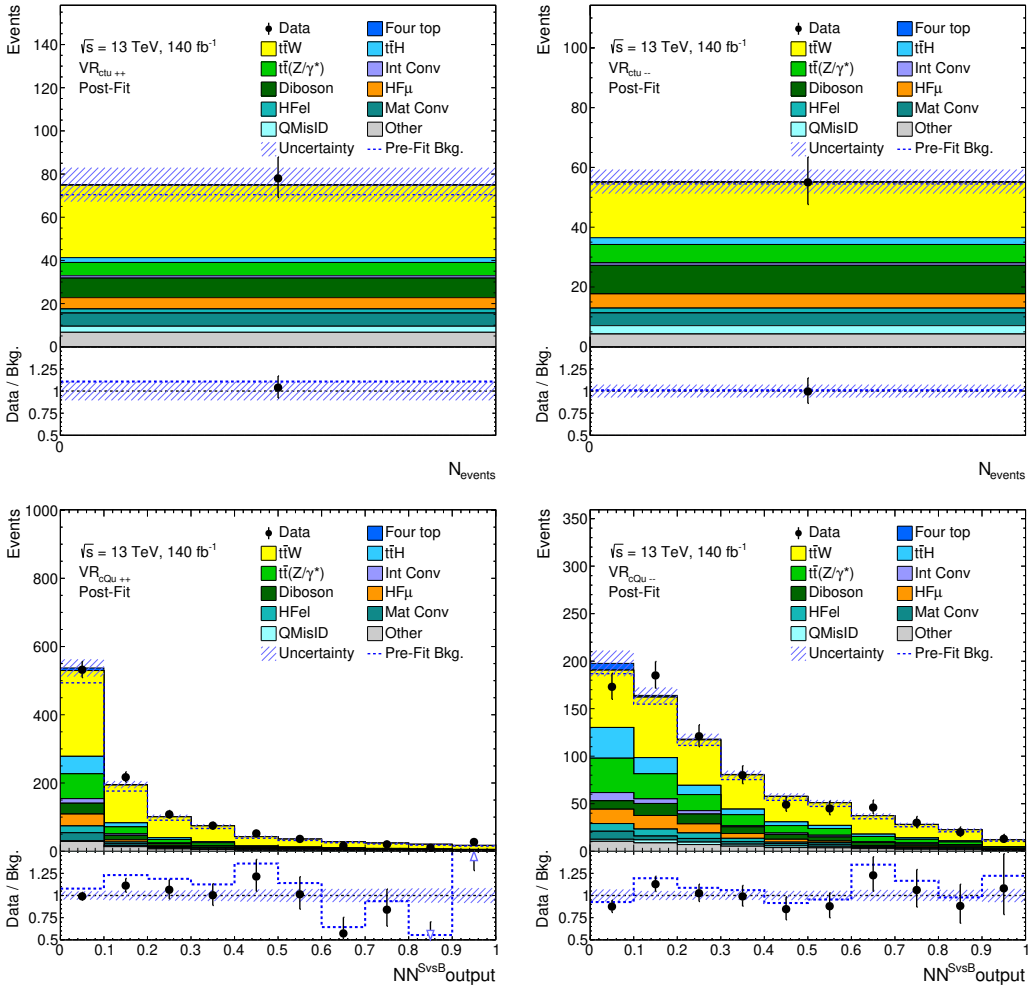

Figure 9.7: Distributions of the NN^{SvsB} output in the VRs for data and the expected background after the hybrid-Asimov fit to all analysis regions. The post-fit background expectations are shown as filled histograms, the combined pre-fit background expectations are shown as dashed lines. The ratio of the data to the total post-fit background is shown in the lower panel. The arrows in the ratio plot indicate that the ratio is outside the range of the plot. The combined statistical and systematic uncertainty in MC simulation is indicated by the hatched band, while the vertical error bars represent the statistical uncertainty in the data.

9.3 Fit to data in all analysis regions

The final maximum likelihood fit is performed under the signal+background hypothesis using the data for all analysis regions. As for the previous fits, the VRs are not considered in the fit. Similar to the hybrid-Asimov fit, all background NFs and the

WCs are free to float.

No deviation from the SM was found in this fit, hence no significant signal contribution was fitted. A post-fit summary plot for the nine CRs is shown in Figure 9.8, and the post-fit distributions of the NN^{SvsB} output for the four SRs are shown in Figure 9.9.

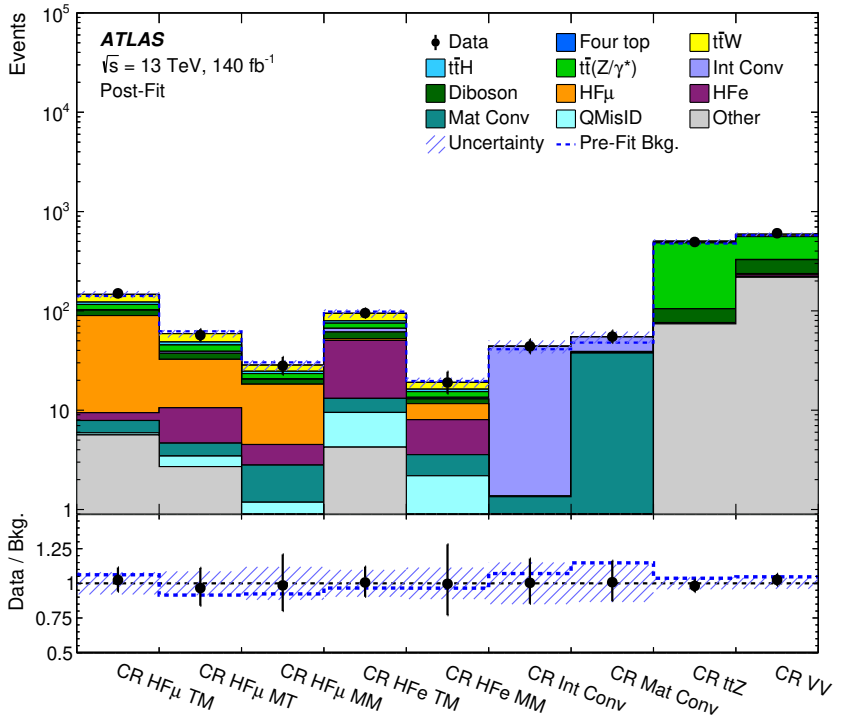

Figure 9.8: Comparison between the event yields in data and the background expectation for the nine CRs after the data fit. The post-fit background expectations are shown as filled histograms, the combined pre-fit background expectations are shown as dashed lines. The ratio of the data to the total post-fit background is shown in the lower panel. The combined statistical and systematic uncertainty in the simulation is indicated by the hatched band, while the vertical error bars represent the statistical uncertainty in the data. This plot was published in Ref. [1].

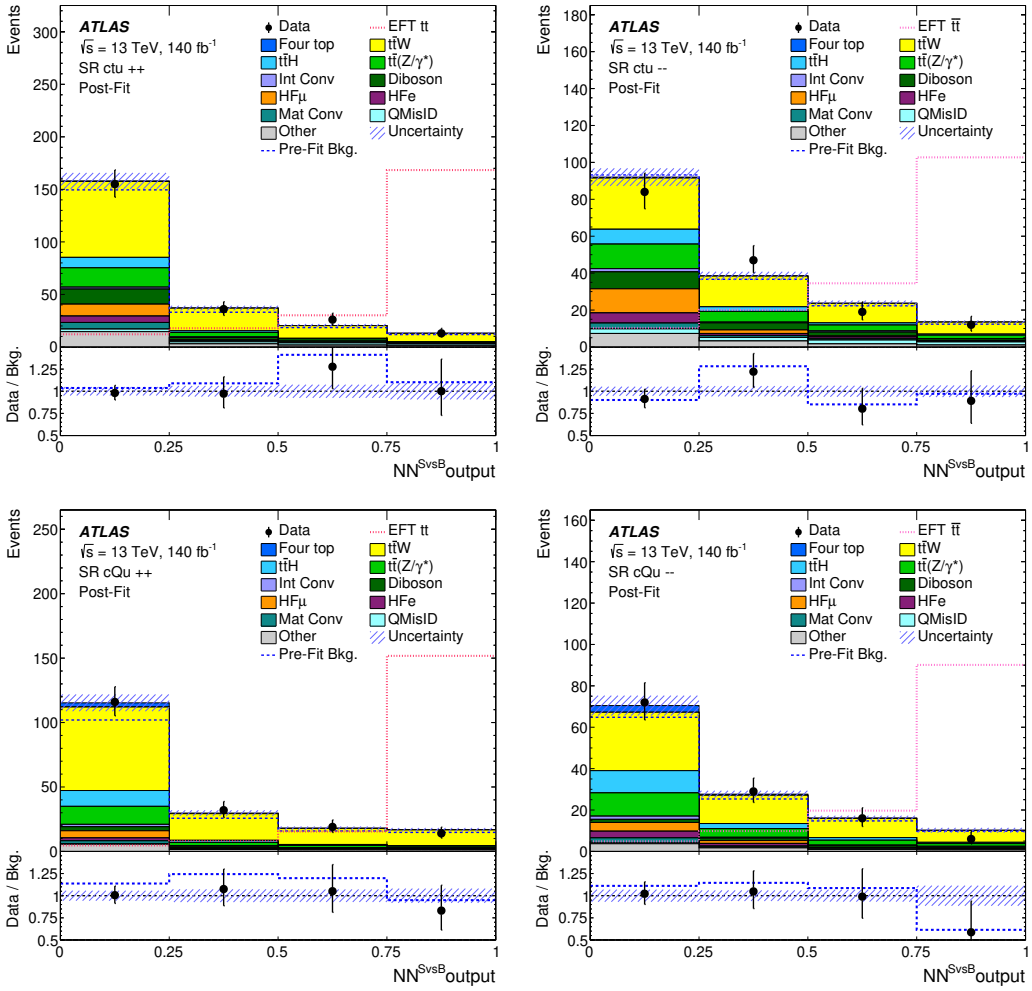

Figure 9.9: Distributions of the $\mathrm{NN^{SvsB}}$ output in the four SRs for data and the expected background after the data fit. The post-fit background expectations are shown as filled histograms, the combined pre-fit background expectations are shown as dashed lines. The signal distribution using the WC values $c_{tu}^{(1)} = 0.04$, $c_{Qu}^{(1)} = 0.1$, $c_{Qu}^{(8)} = 0.1$ is shown with a dotted line, normalized to the same number of events as the background. The ratio of the data to the total post-fit background is shown in the lower panel. The combined statistical and systematic uncertainty in MC simulation is indicated by the hatched band, while the vertical error bars represent the statistical uncertainty in the data. These figures were published in Ref. [1].

As in the previous fits, very good agreement between data and the SM predictions is observed in the CRs. In the SRs the data and SM predictions agree within their uncertainties, while high $\mathrm{NN^{SvsB}}$ bins tend to contain less data than predicted by the SM, hence leaving less room for signal. Consequently, this will lead to the observed limits being slightly more strict compared to the expected limits. The next section discusses both the derivation of the limits and the limits themselves.

The fitted normalization factors and WC values are shown in Figure 9.10. All three WCs were fitted to a value of $\leq 10^{-5}$. The fitted signal contribution is found to be ≤ 0.001 events in all SRs, resulting in rounded yields of zero. Therefore, instead of showing the fitted signal yields in Figure 9.9 the signal distribution using the WC values $c_{tu}^{(1)} = 0.04$, $c_{Qu}^{(1)} = 0.1$, $c_{Qu}^{(8)} = 0.1$ is shown, normalized to the same number of events as the background.

The fitted NFs for the background processes are consistent with the previous fits. The already observed excess for the $t\bar{t}W$ NF did increase further from $1.27^{+0.23}_{-0.23}$ in the hybrid-Asimov to $1.37^{+0.26}_{-0.26}$ in this fit. This shift is caused by unblinding the remaining SR bins. Notably, the third bin in both the $\mathrm{SR_{ctu++}}$ and $\mathrm{SR_{cQu++}}$ regions drives an increase in the $t\bar{t}W$ NF. This occurs because these bins are predominantly populated by $t\bar{t}W$ events, and the observed data exceed the predictions. Moreover, the ++ SRs contain roughly twice as many $t\bar{t}W$ events as the −− regions, making the $t\bar{t}W$ NFs more sensitive in the ++ regions. The fitted NF corresponds to a measured $t\bar{t}W$ cross-section of $\approx 972\,\mathrm{fb}$. This measured $t\bar{t}W$ cross-section is still consistent with the ATLAS and CMS measurements [69, 136].

The data fit to all analysis regions is further validated by checking the post-fit agreement in the VRs, by propagating the fitted NFs and NPs to the VRs. The VRs are presented in Figure 9.11 as a summary plot. The post-fit background predictions are in good agreement with the data in all VRs.

The post-fit event yields after performing the data fit to all analysis regions are reported in the Tables 9.1, 9.2, 9.3 and 9.4, for the SRs, VRs, 2ℓ CRs and 3ℓ CRs, respectively.

Since no significant signal contribution is observed in the fit to data, observed upper limits on three WCs and the cross-section for same-charge top-quark pair production are derived by running 1D- and 2D-likelihood scans, presented in the next section. The results of this fit to data is publicly available in the HEPData repository [31]. Additional plots for the data fit to all analysis regions can be found in the Appendix B.3.

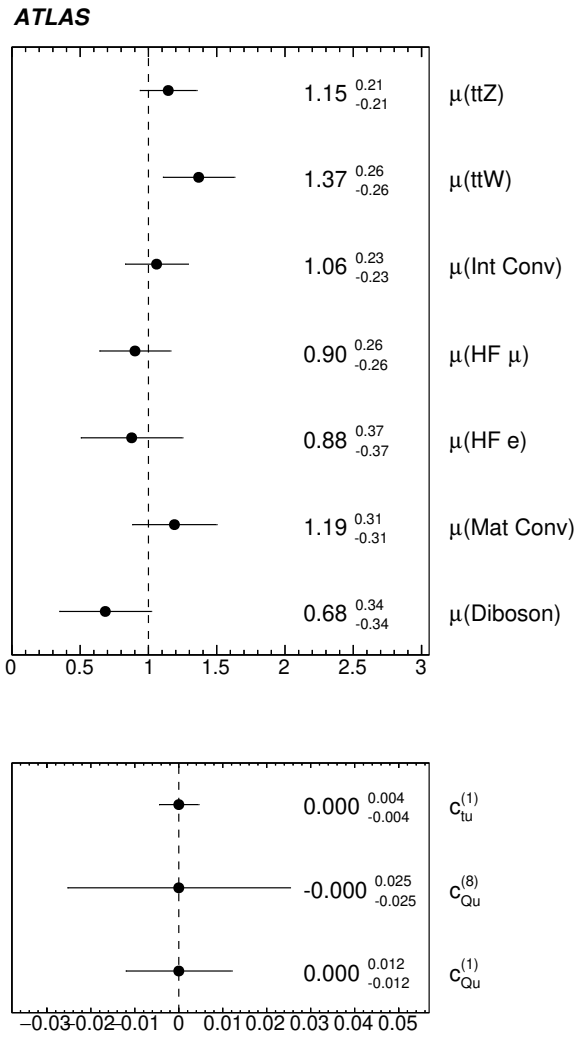

Figure 9.10: Post-fit normalization factors for the background processes (top) and the fitted WCs values (bottom) for the data fit to all analysis regions. The upper plot was published in the auxiliary material of Ref. [1].

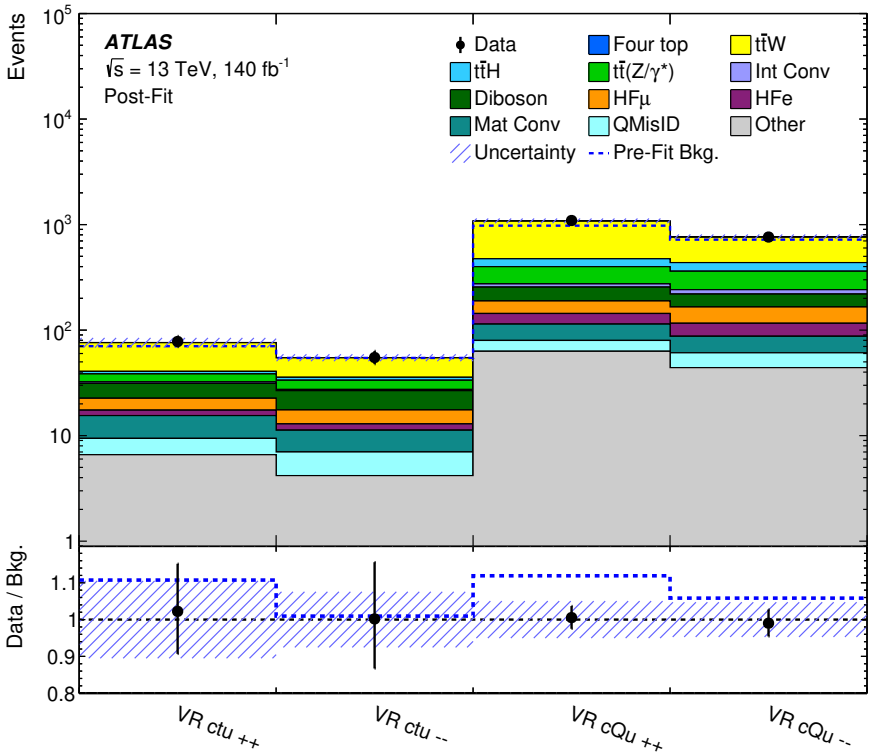

Figure 9.11: Comparison between data and the background expectation after the data fit for the four VRs. The post-fit background expectations are shown as filled histograms, the combined pre-fit background expectations are shown as dashed lines. The ratio of the data to the total post-fit background is shown in the lower panel. The combined statistical and systematic uncertainty for MC is indicated by the hatched band, while the vertical error bars represent the statistical uncertainty on the data. This figure was published in the auxiliary material of Ref. [1].

Table 9.1: Summary of the observed and predicted number of events in the four SRs. The background prediction is shown after the combined likelihood fit to data under the signal-plus-background hypothesis across all CRs and SRs. The uncertainties in the total yields are smaller than the sum in quadrature of the uncertainties in the individual contributions due to anti-correlations between parameters in the likelihood fit. This table was published in Ref. [1].

Process	SR_{ctu++}	SR_{ctu--}	SR_{cQu++}	SR_{cQu--}
$t\bar{t}W$	114 ± 15	62 ± 10	110 ± 15	56.9 ± 8.9
$t\bar{t}(Z/\gamma^*)$	25.5 ± 3.0	24.1 ± 2.6	19.5 ± 2.0	19.1 ± 2.1
$t\bar{t}H$	12.4 ± 7.5	12.3 ± 7.1	15.1 ± 9.6	15.1 ± 9.2
Four top	0.72 ± 0.15	0.69 ± 0.14	4.16 ± 0.83	4.07 ± 0.82
Diboson	18.1 ± 9.3	15.9 ± 8.1	6.3 ± 3.2	4.2 ± 2.1
HFe	6.5 ± 2.9	7.6 ± 3.0	3.0 ± 1.1	4.9 ± 2.5
HFμ	12.6 ± 2.7	15.7 ± 3.2	6.3 ± 1.8	5.7 ± 1.7
Mat Conv	7.6 ± 2.5	5.5 ± 1.6	2.73 ± 0.83	3.3 ± 1.2
Int Conv	2.7 ± 1.6	3.0 ± 1.7	2.1 ± 1.2	2.7 ± 1.6
QMisID	8.1 ± 2.2	8.1 ± 2.2	1.48 ± 0.39	1.48 ± 0.39
Other	20.3 ± 5.5	13.3 ± 4.0	9.3 ± 2.8	7.0 ± 2.7
Total Bkg.	228 ± 11	167.7 ± 7.9	180 ± 10	124.5 ± 6.3
Data	230	162	181	123

Table 9.2: Summary of the observed and predicted number of events in the four VRs. The background prediction is shown after the combined likelihood fit to data under the signal-plus-background hypothesis across all CRs and SRs. The uncertainties in the total yields are smaller than the sum in quadrature of the uncertainties in the individual contributions due to anti-correlations between parameters in the likelihood fit.

Process	VR_{ctu++}	VR_{ctu--}	VR_{cQu++}	VR_{cQu--}
$t\bar{t}W$	35.4 ± 5.7	18.9 ± 3.5	602 ± 83	322 ± 54
$t\bar{t}(Z/\gamma^*)$	6.15 ± 0.89	6.10 ± 0.90	125 ± 16	120 ± 15
$t\bar{t}H$	2.2 ± 1.4	2.2 ± 1.3	75 ± 47	75 ± 46
Four top	0.289 ± 0.058	0.280 ± 0.056	10.8 ± 2.2	11.1 ± 2.2
Diboson	8.7 ± 4.4	9.2 ± 4.7	67 ± 34	54 ± 27
HFe	1.9 ± 1.2	1.66 ± 0.79	30 ± 11	29 ± 10
HFμ	5.2 ± 8.5	4.6 ± 1.1	45 ± 10	50 ± 11
Mat Conv	6.1 ± 3.0	4.3 ± 1.2	34.2 ± 9.7	26.5 ± 7.6
Int Conv	1.01 ± 0.61	0.71 ± 0.69	19 ± 11	22 ± 13
QMisID	2.82 ± 0.74	2.82 ± 0.74	16.8 ± 4.6	16.8 ± 4.6
Others	6.6 ± 1.7	4.2 ± 1.1	63 ± 17	44 ± 14
Total Background	76.3 ± 8.0	54.9 ± 4.1	1087 ± 55	770 ± 36
Data	78	55	1093	762

Table 9.3: Summary of the observed and predicted number of events in the five 2ℓ CRs. The background prediction is shown after the combined likelihood fit to data under the signal-plus-background hypothesis across all CRs and SRs. The uncertainties in the total yields are smaller than the sum in quadrature of the uncertainties in the individual contributions due to anti-correlations between parameters in the likelihood fit. This table was published in Ref. [1].

Process	CR HFμ TM	CR HFμ MT	CR HFμ MM	CR HFe TM	CR HFe MM
$t\bar{t}W$	24.0 ± 4.9	10.3 ± 2.0	3.73 ± 0.86	15.1 ± 2.9	2.76 ± 0.59
$t\bar{t}(Z/\gamma^*)$	13.6 ± 2.6	6.2 ± 1.1	2.59 ± 0.58	8.4 ± 1.8	1.90 ± 0.37
$t\bar{t}H$	6.6 ± 4.0	3.2 ± 1.9	1.28 ± 0.79	4.1 ± 2.4	0.90 ± 0.58
Four top	0.113 ± 0.028	0.071 ± 0.017	0.046 ± 0.012	0.069 ± 0.019	0.036 ± 0.009
Diboson	11.9 ± 6.1	4.9 ± 2.5	2.2 ± 1.1	8.6 ± 4.4	1.35 ± 0.71
HFe	1.6 ± 1.1	5.9 ± 2.9	1.71 ± 0.97	37 ± 12	4.5 ± 1.6
HFμ	80 ± 14	21.9 ± 5.6	13.7 ± 3.2	2.20 ± 0.66	3.62 ± 0.99
Mat Conv	2.0 ± 7.1	1.20 ± 0.56	1.62 ± 0.51	3.7 ± 2.1	1.38 ± 0.43
Int Conv	0.68 ± 0.41	1.7 ± 1.0	0.30 ± 0.18	5.5 ± 3.2	0.48 ± 0.31
QMisID	0.28 ± 0.13	0.75 ± 0.54	0.38 ± 0.26	5.2 ± 2.9	1.6 ± 1.0
Other	5.6 ± 1.5	2.71 ± 0.68	0.81 ± 0.22	4.2 ± 1.1	0.63 ± 0.17
Total Bkg.	147 ± 12	59.0 ± 5.1	28.4 ± 3.4	94.4 ± 9.2	19.1 ± 2.2
Data	150	57	28	95	19

Table 9.4: Summary of the observed and predicted number of events in the four 3ℓ CRs. The background prediction is shown after the combined likelihood fit to data under the signal-plus-background hypothesis across all CRs and SRs. The uncertainties in the total yields are smaller than the sum in quadrature of the uncertainties in the individual contributions due to anti-correlations between parameters in the likelihood fit. This table was published in Ref. [1].

Process	CR Int Conv	CR Mat Conv	CR ttZ	CR VV
$t\bar{t}W$	–	–	8.4 ± 1.8	24.5 ± 4.7
$t\bar{t}(Z/\gamma^*)$	–	–	378 ± 32	230 ± 28
$t\bar{t}H$	–	–	10.0 ± 6.3	6.3 ± 4.0
Four top	–	–	1.61 ± 0.32	0.092 ± 0.020
Diboson	0.025 ± 0.019	1.40 ± 0.72	29 ± 15	90 ± 45
HFe	–	–	0.47 ± 0.35	9.2 ± 6.8
HFμ	–	–	1.04 ± 0.35	7.5 ± 1.8
Mat Conv	1.3 ± 1.1	37.6 ± 8.6	0.59 ± 0.40	2.19 ± 0.77
Int Conv	42.5 ± 6.8	15.6 ± 4.3	0.14 ± 0.15	1.66 ± 0.96
QMisID	–	–	0.22 ± 0.17	0.83 ± 0.41
Other	–	–	74 ± 23	218 ± 41
Total Bkg.	43.9 ± 6.6	54.6 ± 7.3	503 ± 22	590 ± 23
Data	44	55	494	605

9.4 Upper limits on SMEFT wilson coefficients

Upper limits on the considered SMEFT operators are derived in this section. These limits are obtained by performing likelihood scans over the three WCs $c_{tu}^{(1)}$, $c_{Qu}^{(1)}$, and $c_{Qu}^{(8)}$, using both the fit to data and the fit to hybrid-Asimov data. For each WC a separate likelihood scan is performed. The EFT parameterization presented in Section 7.4 allows any value of the WCs to be injected during the likelihood scans. In these scans the WCs are varied in the ranges $[-0.01, 0.01]$ for $c_{tu}^{(1)}$, $[-0.03, 0.03]$ for $c_{Qu}^{(1)}$, and $[-0.06, 0.06]$ for $c_{Qu}^{(8)}$, with 60 scanned points for each scan. Different ranges are used to reflect the different expected sensitivities of the three WCs. For each scanned point the likelihood value quantifies the agreement between data and the prediction including signal according to the injected WC value. Since the SRs are already in good agreement with the SM predictions, the likelihood is expected to reach its minimum with the WCs being zero and to increase as the WC deviates further from zero. In the likelihood scans all NPs, NFs, and the other two WCs are allowed to vary freely. However, the freely floating WCs tend to be fitted towards zero, as the data are consistent with the SM predictions and barely leave room for signal events. Consequently, additional signal events lead to worse agreement with the data and are therefore penalized in the likelihood. Furthermore, the contribution of the signal cannot reach negative values due to the purely quadratic EFT parameterization.

The observed and expected limits on the WCs are then determined by identifying the intersection points between the likelihood scan curve and the 1σ and 2σ threshold lines. Under Wilks' theorem [138] and the asymptotic approximation, these thresholds correspond to changes in the likelihood associated with one and two standard deviations from the best-fit value, which represent confidence levels (CLs) of approximately 68 % and 95 %, respectively. Wilks' theorem states that, in the large sample limit, the distribution of the log-likelihood ratio test statistic approaches a χ^2 distribution with degrees of freedom equal to the number of free parameters being tested. Hence, the 1σ and 2σ threshold lines correspond to 1 and 3.84 for one degree of freedom, respectively, for the negative log-likelihood ratio test statistic in Equation 7.6. As in the likelihood scans the negative log-likelihood ratio test statistic is used without the factor of 2, the 1σ and 2σ threshold lines are set to 0.5 and 1.92, respectively. The observed limits are determined by the intersection points with the likelihood scan curve from the fit to data, while the expected limits are determined by the intersection points with the likelihood scan curve from the fit to hybrid-Asimov data.

Following this strategy, in Figure 9.12 likelihood scans for three WCs and their observed and expected limits at 68 % and 95 % CL are shown. The observed (expected) limits at 95 % CL in (TeV/Λ^2) are $c_{tu}^{(1)} < 0.0068\,(0.0071)$, $c_{Qu}^{(1)} < 0.020\,(0.022)$ and $c_{Qu}^{(8)} < 0.041\,(0.046)$. These WC limits can be translated into observed (expected)

cross-section limits. For all three WCs this results in the same observed (expected) cross-section limit at 95 % CL of 1.6 (2.0) fb, when applying proper rounding.

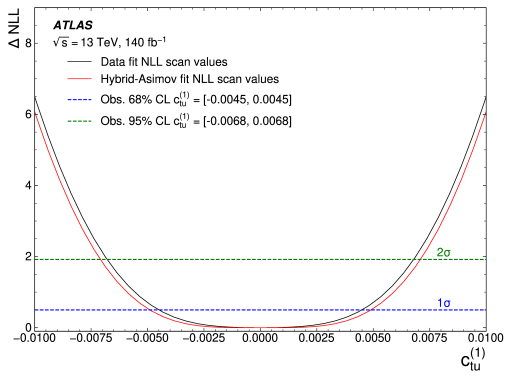

(a) $c_{tu}^{(1)}$

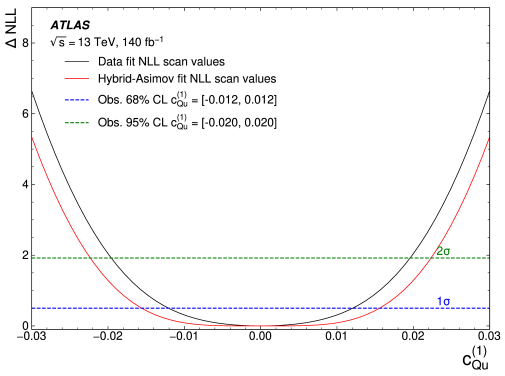

(b) $c_{Qu}^{(1)}$

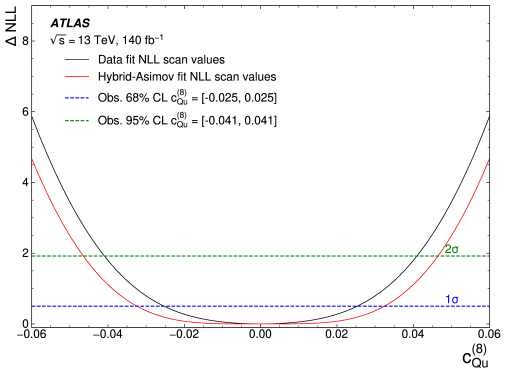

(c) $c_{Qu}^{(8)}$

Figure 9.12: Limits for the three different WCs: (a) $c_{tu}^{(1)}$, (b) $c_{Qu}^{(1)}$, and (c) $c_{Qu}^{(8)}$. The observed and expected limits at 68 % and 95 % confidence level (CL) can be read off by finding the intersection of the likelihood scan curve with the 1σ and 2σ lines. The observed limits are shown numerically in the respective legend. The new-physics scale is set to $\Lambda = 1\,\text{TeV}$. These figures were published in the auxiliary material of Ref. [1].

However, it should be noted that the presented results violate Wilks' Theorem by the quadratic EFT terms, according to Ref. [139]. This violation arises because the quadratic EFT terms do not allow negative signal contributions, which creates a boundary in the parameter space at the SM hypothesis. As a consequence of

violating Wilks' Theorem, the derived confidence intervals (CIs) may be over- or underestimated, as the log-likelihood ratio test statistic is not guaranteed to follow a χ^2 distribution. Hence, it has to be carefully checked if and how the results of this analysis are affected by this violation. The limits are validated by comparing them to the limits derived from MC pseudo-experiments, referred to as toy experiments in the following. The toy experiments are generated by varying the post-fit NFs and NPs using the results from the fit to data according to its standard deviation. Separate toy experiments are created for each WCs separately. The true value of the considered WC is set to the observed limit value, while the other two WCs are set to zero for the toy creation. For each WC 25000 toy experiments were generated. The goal of this approach is to check the coverage of the CI. Therefore, for each toy the fit procedure and the likelihood scans are performed and the CI for the non-zero WC is determined. Then for each toy, it is checked if the injected WC value is covered by the derived CIs. By definition, a CI at 95 % CL is expected to cover the true value in 95 % of the cases, while a CI at 68 % CL is expected to cover the true value in 68 % of the cases. Deviations from these expected coverages are referred to as over- or undercoverage.

Following this cross-check, slight overcoverage for both the 68 % and 95 % CIs are observed for all three WCs using their respective observed limits as the injected true value for the toy experiments. To correct the limits for the overcoverage, the 1σ and 2σ lines are shifted downwards until the expected coverage is achieved for the toy experiments. The shifted 1σ and 2σ lines are then propagated to the likelihood scans from the fit to data. Consequently, the corrected limits at 95 % CL are slightly stricter with $c_{tu}^{(1)} < 0.0065$, $c_{Qu}^{(1)} < 0.018$ and $c_{Qu}^{(8)} < 0.037$. These corrected limits are at most 9 % more strict than the uncorrected limits. However, the shifted 1σ and 2σ lines are only valid for the injected WC values used for the generation of the toy experiments. Therefore, this procedure needs to be repeated for the all WCs values considered in the likelihood scans in order to get the fully corrected 1σ and 2σ lines, which is computationally very expensive, especially for multidimensional scans.

As the presented check shows, the derived CIs are only affected by overcoverage. Hence, the non-corrected results are considered as valid as they are slightly less strict. Additionally, deriving the corrected limits for the upcoming 2D-likelihood scans would be computationally very expensive and complex. Lastly, during the finalization of this analysis the discussion about the validity of Wilks' Theorem in the context of EFTs was ongoing within the ATLAS Collaboration. Furthermore, computing the corrected limits is computationally very expensive. Hence, the non-corrected limits are used for the final results, as they were shown to be conservative. Additional information about the coverage check for Wilks' Theorem is given in the Appendix C.

The observed CIs at 95 % CL on the three WCs for different sets of uncertainties are summarized in Table 9.5. The first row presented the CIs when considering only statistical uncertainties, in the second row the modeling uncertainties are added and

the last row shows the CIs using all uncertainties. The table clearly shows that the sensitivity of this analysis is limited by the available number of events. The observed limits are degraded by about 3 % when including all systematics. The largest degradation is caused by the $t\bar{t}W$ modeling uncertainties, namely the ME and PS uncertainties. As $t\bar{t}W$ is the dominant background processes in the signal sensitive SR bins, this behavior is expected.

Table 9.5: Observed 95 % CL confidence intervals on the three WCs for different sets of uncertainties. The first, second and third rows show the limits obtained by considering, respectively: only the statistical uncertainties, both the statistical and modeling uncertainties, and all uncertainties. The new-physics scale is set to $\Lambda = 1\,\text{TeV}$. This table was published in Ref. [1]

Wilson Coefficient CIs at 95 % CL ($\times 10^{-2}$)			
Uncertainties	$c_{tu}^{(1)}$	$c_{Qu}^{(1)}$	$c_{Qu}^{(8)}$
Statistical uncertainty only	[-0.65, 0.65]	[-1.9, 1.9]	[-3.9, 3.9]
Statistical + modeling uncertainties	[-0.67, 0.67]	[-1.9, 1.9]	[-4.0, 4.0]
Total uncertainty	[-0.68, 0.68]	[-2.0, 2.0]	[-4.1, 4.1]

In Figure 9.13 two-dimensional-likelihood scans are performed for the different combination of the three WCs. As for the 1D-scans, the NPs, NFs and the remaining WC is allowed to vary freely. In the 2D-scans, the 1σ and 2σ contour lines correspond to higher likelihood values, due to the additional degree of freedom in the 2D-scans compared to the 1D-scans. This results in larger limits within the 2D-likelihood-scans compared to the individual limits from the 1D scans. In order to resolve the 2D-scans properly, the scanned range of WCs values is increased by a factor of ≈ 1.5 for the 2D scans.

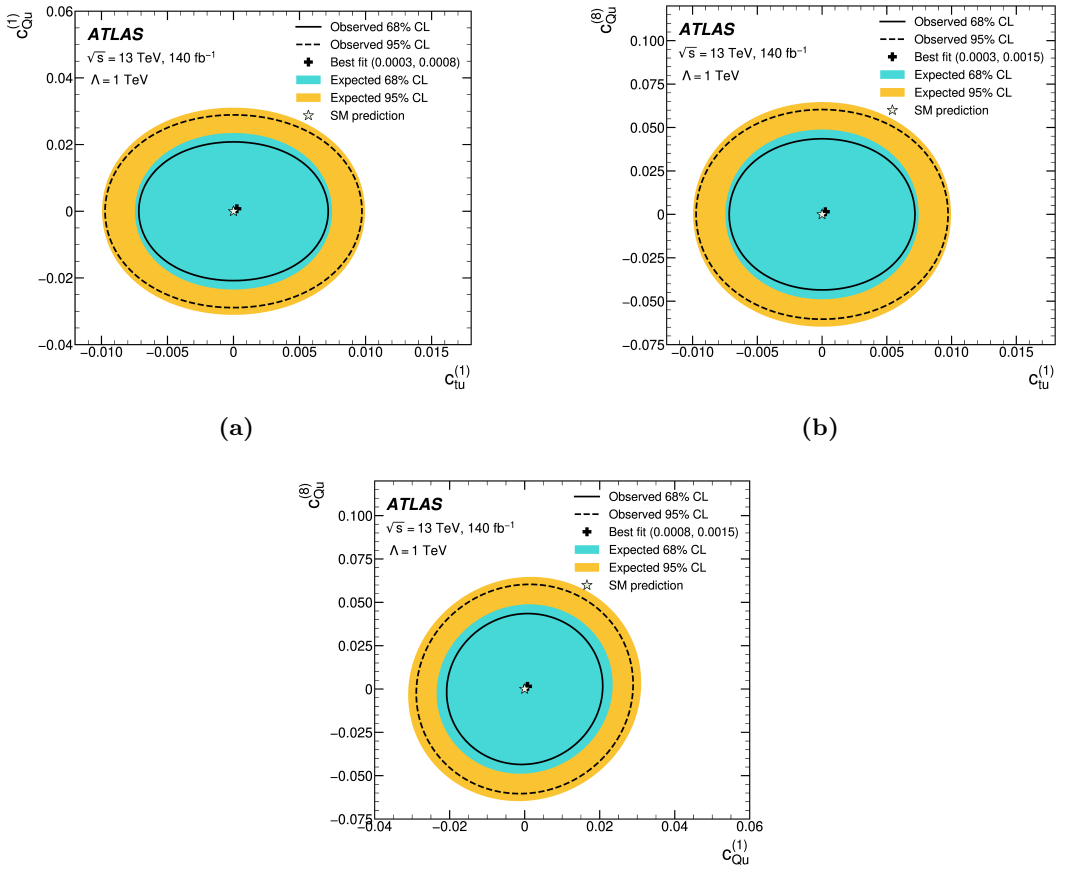

Figure 9.13: 2D likelihood scans for the different combinations of WCs: (a) $c_{tu}^{(1)}$ versus $c_{Qu}^{(1)}$, (b) $c_{tu}^{(1)}$ versus $c_{Qu}^{(8)}$, and (c) $c_{Qu}^{(1)}$ versus $c_{Qu}^{(8)}$. The observed limits at 68 % and 95 % CL are represented by solid and dashed lines, respectively, while the expected limits are illustrated by the inner and outer shaded regions. The best fit value is marked with a black cross. The SM prediction is marked with a white star. The new-physics scale is set to $\Lambda = 1\,\text{TeV}$. These figures were published in Ref. [1].

9.5 Comparison to previous analyses

The resulting limits of the previous section are now compared to the limits of previous analyses. The previous best limits were achieved by an ATLAS Run 1 analysis of events with b-tagged jets and a same-charge lepton pair [30]. The analysis used the Run 1 dataset with a center-of-mass energy of 8 TeV and an integrated luminosity of $20.3\,\text{fb}^{-1}$ and interpreted the results using several BSM models. As this analysis did only provide cross-section limits at 95 % CL for same-charge top-quark pair production for different chiralities, the cross-section limits are translated to constraints on the WCs by using the fitted EFT parameterization of this analysis.

The results are compared in two separate ways in Figure 9.14 and Figure 9.15.

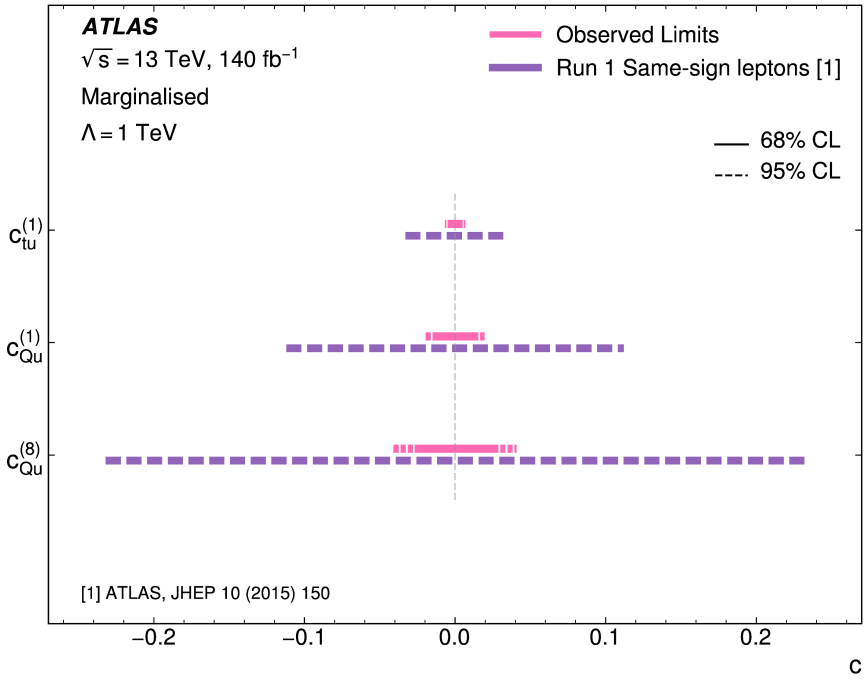

Figure 9.14: Comparison of the observed limits on the three WCs of this analysis to the limit obtained by the ATLAS Run 1 analysis of events with b-tagged jets and a same-charge lepton pair [30]. The cross-section limits from the Run 1 search are converted to the limits on the WCs by using the fitted EFT parametrization. The bounds on the WCs are shown at the 68 % CL (solid) and/or 95 % CL (dashed) levels. For the ATLAS Run 1 analysis, only the limits at 95 % CL are available. The vertical bar represents the SM prediction. The new-physics scale is set to $\Lambda = 1\,\text{TeV}$. This figure was published in Ref. [1].

In Figure 9.14 the direct WC limits are compared. As the ATLAS Run 1 analysis only

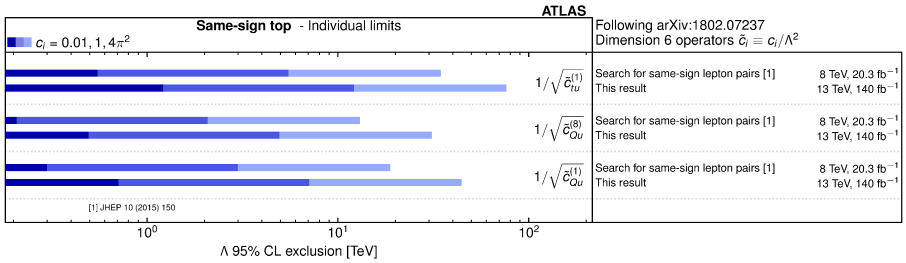

Figure 9.15: Observed lower limits at 95 % confidence level on the scale of new physics Λ for WC values of 0.01, 1 and $4\pi^2$. The limits are compared with the results of other analyses. This plot was published in Ref. [1].

provides limits at 95 % CL, no limits at 68 % CL are available for the comparison. For the second comparison limits are set on the new-physics scale Λ and instead the WCs values are set to a constant value of 0.01, 1 or $4\pi^2$. These WC values correspond to a weak coupling, strong coupling and a value where the SMEFT breaks down. Limits on Λ have emerged to be the gold standard for comparing different analyses, as this also allows for a comparison of analyses which do not consider the same value for Λ. However, in this case, the same value of $\Lambda = 1\,\text{TeV}$ is used for both analyses.

In both comparisons, it can be seen that the limits of this analysis are significantly stricter than the previous best limits from the ATLAS Run 1 analysis. Consequently, the ATLAS Run 1 analysis measured observed cross-section limits for same-charge top-quark pair production of 51 fb for left-right handed chirality and 38 fb for right-right handed chirality at 95 % CL. This analysis significantly improves these limits, reducing the cross-section limit to 1.6 fb.

Therefore, this analysis improves on the previous best limits by roughly a factor of 10. A significant part of this improvement stems from the increased dataset size, but the dedicated analysis strategy also plays a crucial role. In particular, the optimized SR definitions using DNNs, the refined background estimation focused on non-prompt leptons, and the improved $t\bar{t}W$ modeling are the key contributors. A simplified analysis that excluded the DNN-based SR definitions indicates that their inclusion alone enhances the limits by approximately 250 %.

10 Summary and Conclusion

In this thesis, the search for the production of same-sign top-quark pairs with identical electric charges using data collected during the full Run 2 period of the ATLAS detector at the LHC was presented. The dataset used corresponds to an integrated luminosity of $140\,\text{fb}^{-1}$, gathered at a center-of-mass energy of $\sqrt{s} = 13\,\text{TeV}$ from 2015 to 2018. The analysis was performed in the framework of the Standard Model Effective Field Theory (SMEFT), focusing on the operators $\mathcal{O}_{tu}^{(1)}$, $\mathcal{O}_{Qu}^{(1)}$, and $\mathcal{O}_{Qu}^{(8)}$ with a new physics scale set to $\Lambda = 1\,\text{TeV}$. The three EFT operators can generate same-charge top-quark pair production, which is otherwise strongly suppressed in the SM. In this analysis, only the dilepton channel is considered, where both top quarks decay via $t \to Wb \to \ell\nu b$. Consequently, the final state signature is characterized by two leptons with the same electric charge, at least two jets, and missing transverse momentum from the two neutrinos. Even though this signature is rarely produced in SM processes, several processes may mimic this final state due to misreconstruction of physics objects or due to detector inefficiencies. Therefore, an accurate background estimation and estimation of systematic uncertainties are crucial to obtaining a reliable result.

Numerous mutually exclusive analysis regions are defined, each enriched in either signal or background events. All analysis regions are used in a profile likelihood fit to extract the signal strength in the form of the three considered Wilson coefficients (WCs).

To optimize the sensitivity, two sets of Deep Neural Networks (DNNs) are employed in the analysis. Initially, a preliminary event selection is applied to reduce background contamination by imposing strict requirements on the b-tagging of jets, the presence of exactly two isolated, same-charge leptons, and a large amount of missing transverse energy. The first set of DNNs is used to create separate signal regions (SRs), each enriched in signal events associated with different EFT operators. Subsequently, these preliminary SRs are further split by the sign of the same-charge lepton pair. A second set of DNNs is then trained to perform signal-background discrimination within each region. This two-step DNN approach enhances the separation between signal and background while allowing for the identification of contributions from different EFT operators. Finally, the regions are divided into validation regions (VRs) and SRs by requiring the azimuthal distance between the lepton pair, $\Delta\phi_{\ell,\ell}$, to be larger than 2.5 to enter the final SRs. Events that do not meet this requirement are used in the VRs to validate the background estimation.

The background estimation strategy combines data-driven and simulation-based methods. Nine control regions, carefully designed to be orthogonal to the SRs, are defined to constrain several background processes. The dominant backgrounds

include $t\bar{t}W$, $t\bar{t}Z$, and non-prompt lepton sources. Consequently, these backgrounds are treated with great care. This analysis applies a comprehensive set of systematic uncertainties to account for detector inefficiencies, modeling uncertainties, and statistical uncertainties, ensuring the robustness of the results.

No evidence for deviations from SM predictions was observed. Consequently, upper limits were set at the 95 % CL for the WCs and the cross-section of same-sign top-quark pair production. The observed limits on the WCs were $|c_{tu}^{(1)}| < 0.0068$, $|c_{Qu}^{(1)}| < 0.020$, and $|c_{Qu}^{(8)}| < 0.041$ ($[\text{TeV}/\Lambda]^2$), with expected limits of 0.0071, 0.022, and 0.046 respectively. Additionally, the production cross-section $\sigma(pp \to tt)$ was constrained to be less than 1.6 fb (observed) and 2.0 fb (expected) at 95 % CL. These results provide the strongest constraints to date for these coefficients and improve previous limits by approximately a factor of 10. This is the first search for same-charge top-quark pair production using SMEFT within the ATLAS Collaboration. The results of this search were also published in Ref. [1].

The sensitivity of this analysis is clearly limited by the amount of available data. Future analyses using the data collected during the LHC Run 3 period, possibly in combination with the Run 2 dataset, are expected to significantly improve the results. Moreover, the analysis could be further refined by dropping the flavor universality assumption for the EFT operators, thereby allowing separate constraints on the WCs for different quark flavors. Such an approach would enable a more detailed exploration of the flavor structure underlying potential new physics. Additionally, the analysis could be extended to include the two other four-fermion operators, $\mathcal{O}_{Qq}^{(1)}$ and $\mathcal{O}_{Qq}^{(3)}$, which can also contribute to same-charge top-quark pair production. Although the corresponding WCs are already strongly constrained by other analyses, the constraints from this analysis are expected to provide even tighter limits.

Appendices

A Input variables for the Neural Networks

In the following appendix chapter the input variables for the Neural Networks used in this analysis are shown. The input variables are shown for the DNN^{SvsS} and DNN^{SvsB} trainings. The input variables are shown for the two EFT signals separately and the background is shown as the sum of all background processes. The distributions are normalized to unity and the first and last bins contain the underflow and overflow events, respectively. Additionally, the feature importance ranking plots are shown for the DNN^{SvsS} and DNN^{SvsB} trainings.

The Section A.1 shows the input variables and ranking plots for the DNN^{SvsS} training and the Section A.2 the DNN^{SvsB} trainings.

A.1 DNN^{SvsS} input variables

In the following figures the nine input variables used for the DNN^{SvsS} training and the permutation feature importance ranking plot are shown.

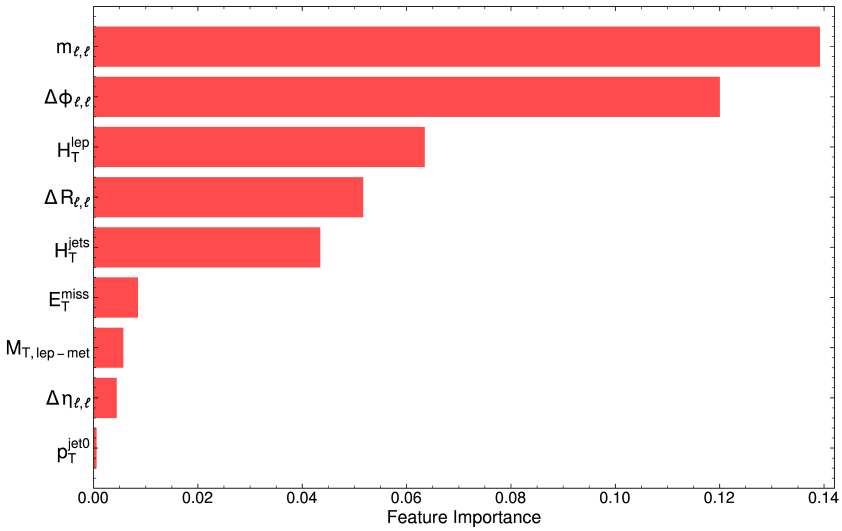

Figure A.1: Permutation feature importance ranking plot for the DNN^{SvsS} training.

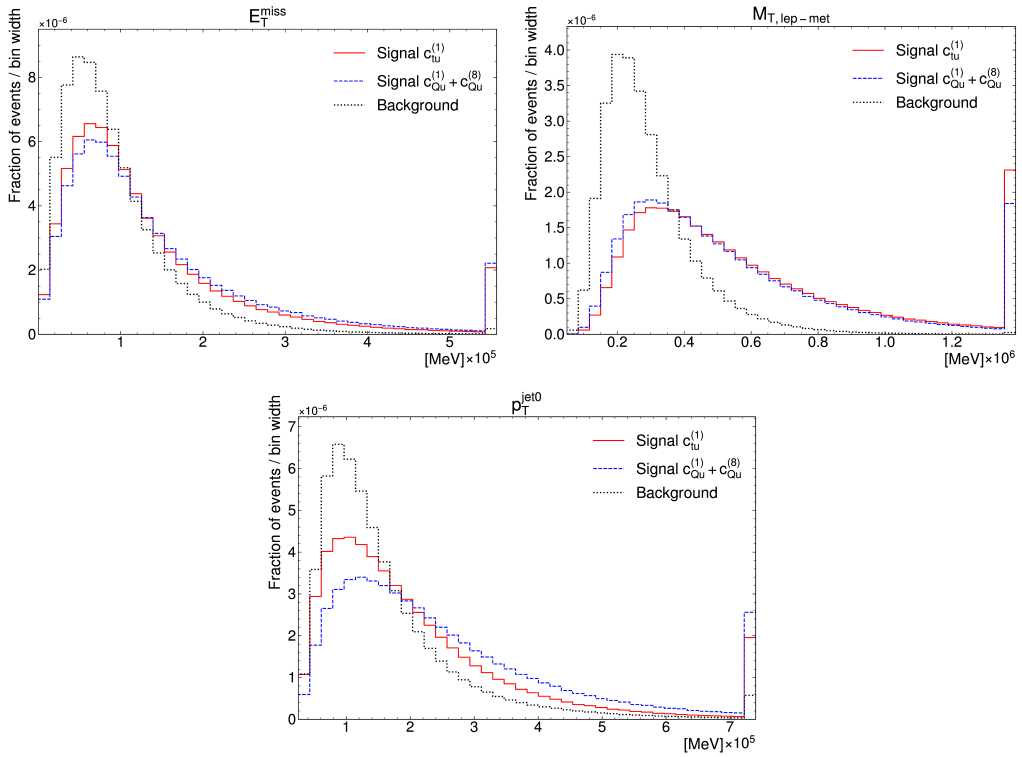

Figure A.2: Kinematic distributions for the first 3 of the 9 input variables that are used for the DNN$^{\text{SvsS}}$ training. The two EFT signals are shown separately for $c_{tu}^{(1)}$ and $c_{Qu}^{(1)} + c_{Qu}^{(8)}$ and the background is shown as the sum of all background processes. All distributions are normalized to unity. The first and last bins contain the underflow and overflow events, respectively.

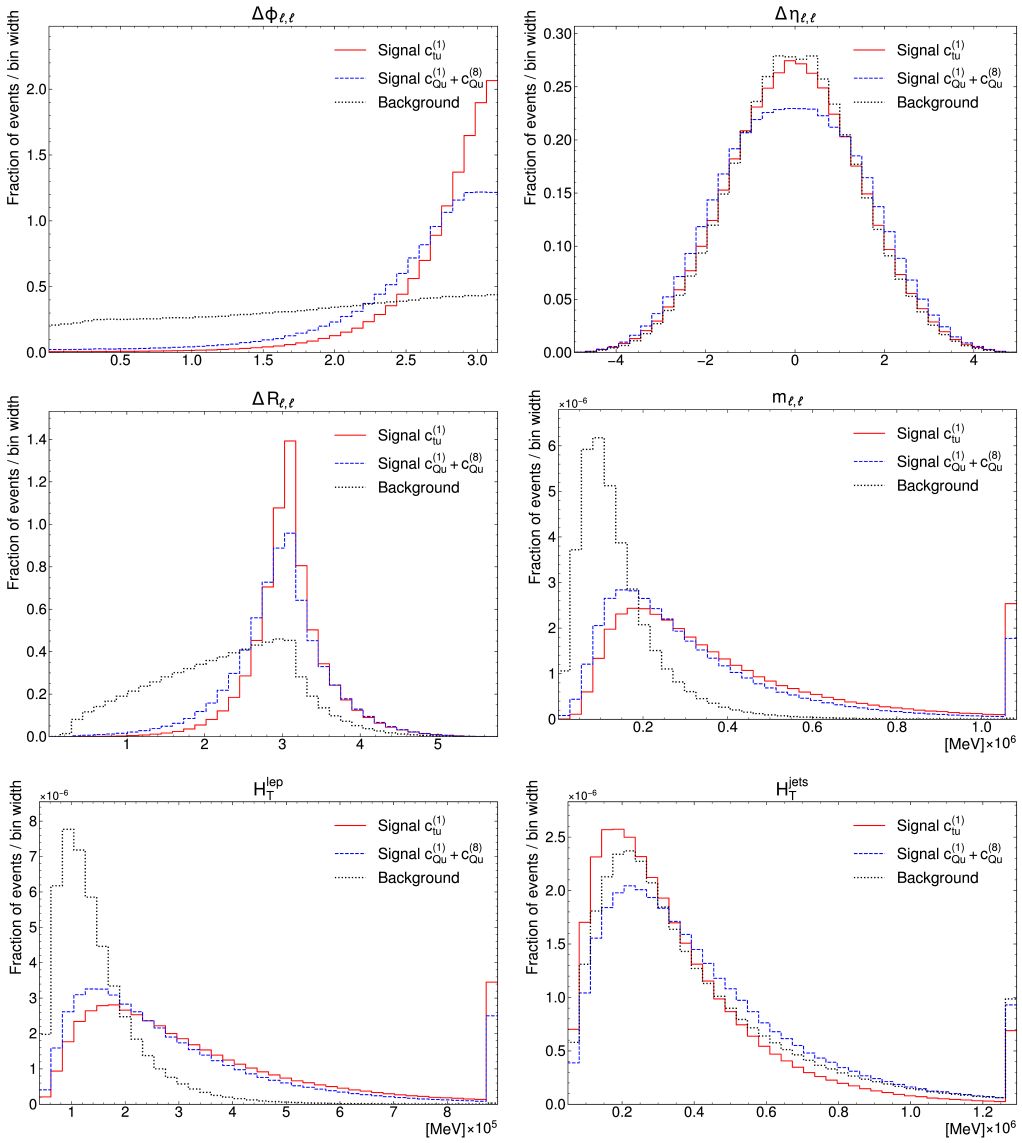

Figure A.3: Kinematic distributions for the last 6 of the 9 input variables that are used for the DNN^{SvsS} training. The two EFT signals are shown separately for $c_{tu}^{(1)}$ and $c_{Qu}^{(1)} + c_{Qu}^{(8)}$ and the background is shown as the sum of all background processes. All distributions are normalized to unity. The first and last bins contain the underflow and overflow events, respectively.

A.2 $\mathrm{DNN}^{\mathrm{SvsB}}$ input variables

In Figure A.4 the input variables for the $\mathrm{DNN}^{\mathrm{SvsB}}$ training for the $\mathrm{SR+VR_{ctu}}$ region are shown. The input variables are shown before applying the split by the total lepton charge. The signal is shown separately for tt and $\overline{tt}$ and the background is shown as the sum of all background processes. The distributions are normalized to unity and the first and last bins contain the underflow and overflow events, respectively. The feature importance ranking plots for the $\mathrm{DNN}^{\mathrm{SvsB}}$ training in the $\mathrm{SR+VR_{ctu++}}$ and $\mathrm{SR+VR_{ctu--}}$ regions are shown in Figure A.5 and Figure A.6, respectively. The same is shown for the $\mathrm{SR+VR_{cQu}}$ region in Figure A.7, Figure A.8 and Figure A.9.

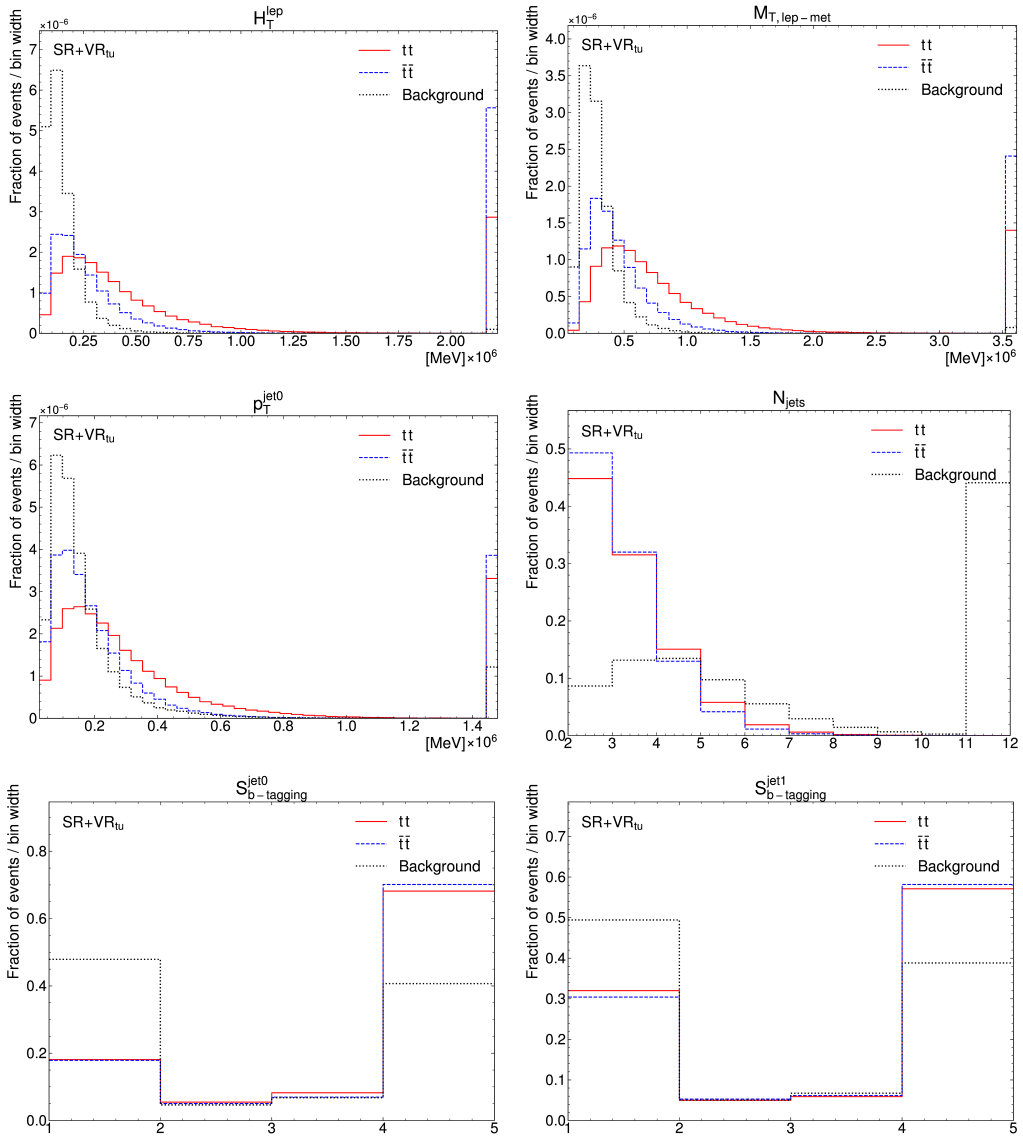

Figure A.4: Kinematic distributions for the 6 input variables that are used for the DNN$^{\mathrm{SvsB}}$ training for the SR+VR$_{\mathrm{ctu}}$ region, before applying the split by the total lepton charge. The signal is shown separately for tt and $\overline{tt}$ and the background is shown as the sum of all background processes. All distributions are normalized to unity. The first and last bins contain the underflow and overflow events, respectively.

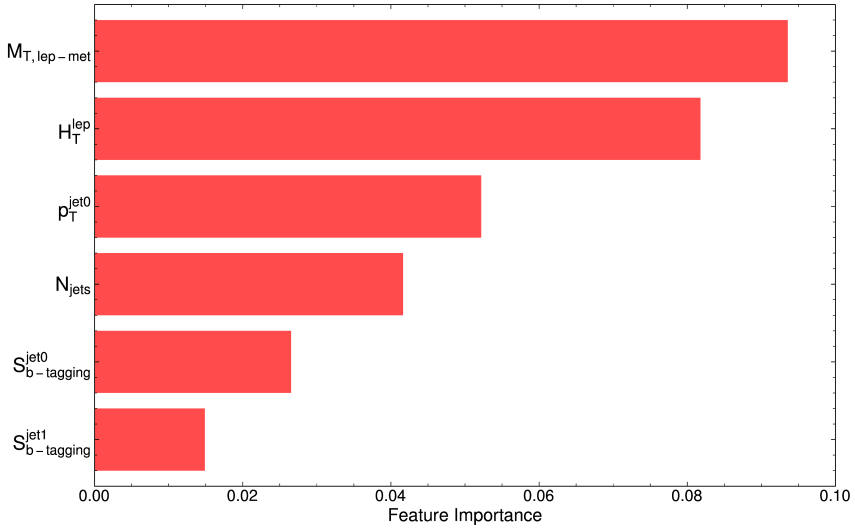

Figure A.5: Permutation feature importance ranking plot for the $\mathrm{DNN}^{\mathrm{SvsB}}$ trained in the $\mathrm{SR{+}VR}_{\mathrm{ctu++}}$ region.

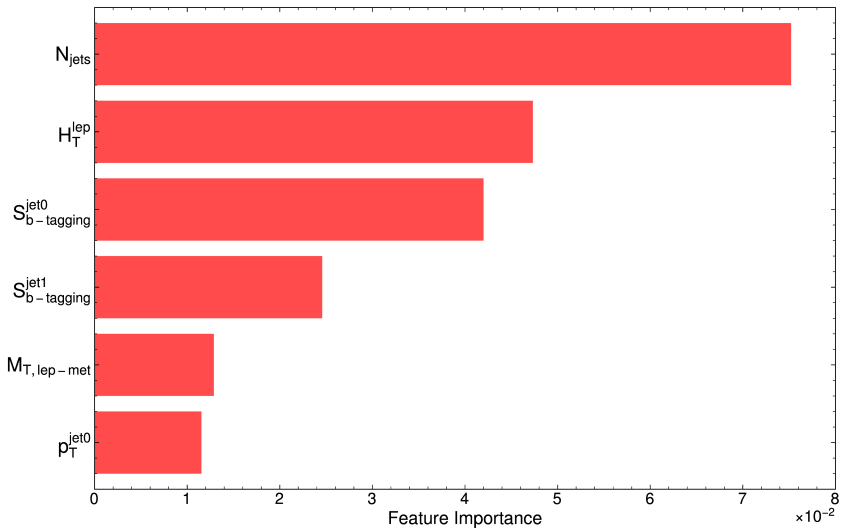

Figure A.6: Permutation feature importance ranking plot for the $\mathrm{DNN}^{\mathrm{SvsB}}$ trained in the $\mathrm{SR{+}VR}_{\mathrm{ctu--}}$ region.

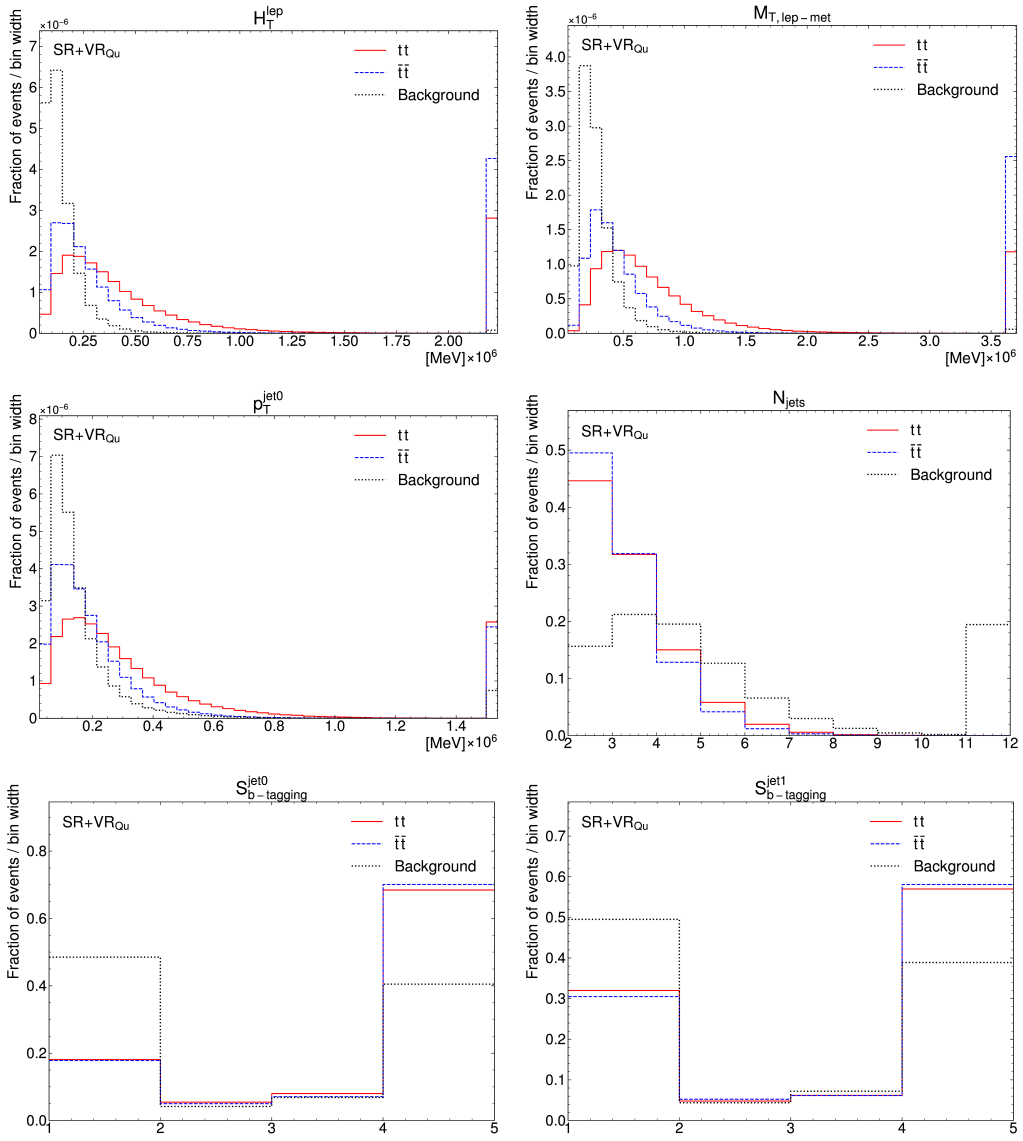

Figure A.7: Kinematic distributions for the 6 input variables that are used for the DNN$^{\mathrm{SvsB}}$ training for the SR+VR$_{\mathrm{cQu}}$ region, before applying the split by the total lepton charge. The signal is shown separately for tt and $\overline{tt}$ and the background is shown as the sum of all background processes. All distributions are normalized to unity. The first and last bins contain the underflow and overflow events, respectively.

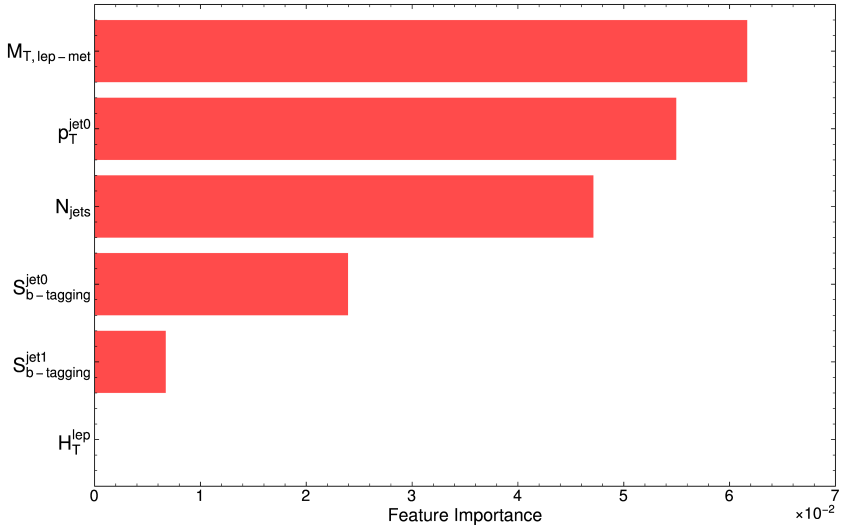

Figure A.8: Permutation feature importance ranking plot for the $\mathrm{DNN}^{\mathrm{SvsB}}$ trained in the $\mathrm{SR{+}VR}_{\mathrm{cQu{+}{+}}}$ region.

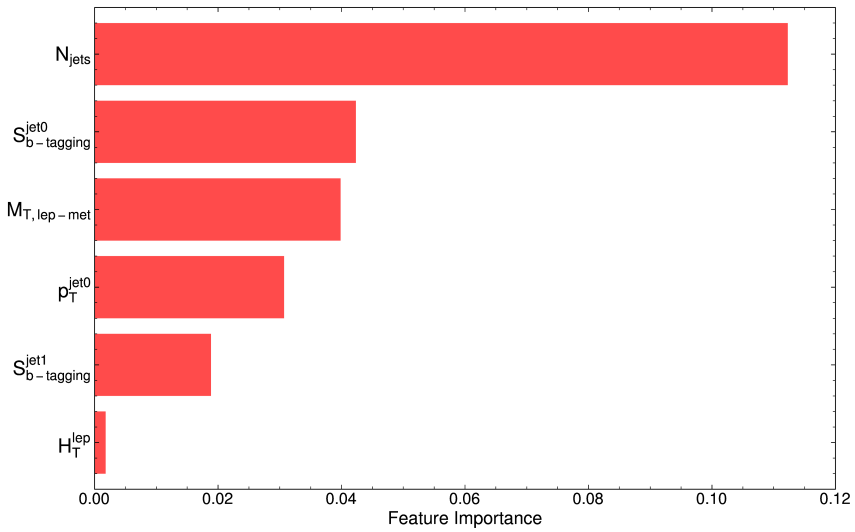

Figure A.9: Permutation feature importance ranking plot for the $\mathrm{DNN}^{\mathrm{SvsB}}$ trained in the $\mathrm{SR{+}VR}_{\mathrm{cQu{-}{-}}}$ region.

B Additional plots for the analysis results

The following appendix chapter contains additional plots for the three likelihood fits performed in this analysis, that are not shown in the main body of the thesis. In the following three sections, additional plots are shown for the background-only fit, the hybrid-Asimov fit, the data fit.

The additionally shown plots primarily focus on giving more details about the behavior of the nuisance parameters in the fit. Therefore, the pulls and constraints resulting from each fit are shown in form of bar plots for the respective nuisance parameters categories, namely electron, muon, data-driven, instrumental, and theory. It should be noted that if a NP is not present in a given plot, this means it was pruned during the fit.

B.1 Background-only fit to all control regions and first signal region bins

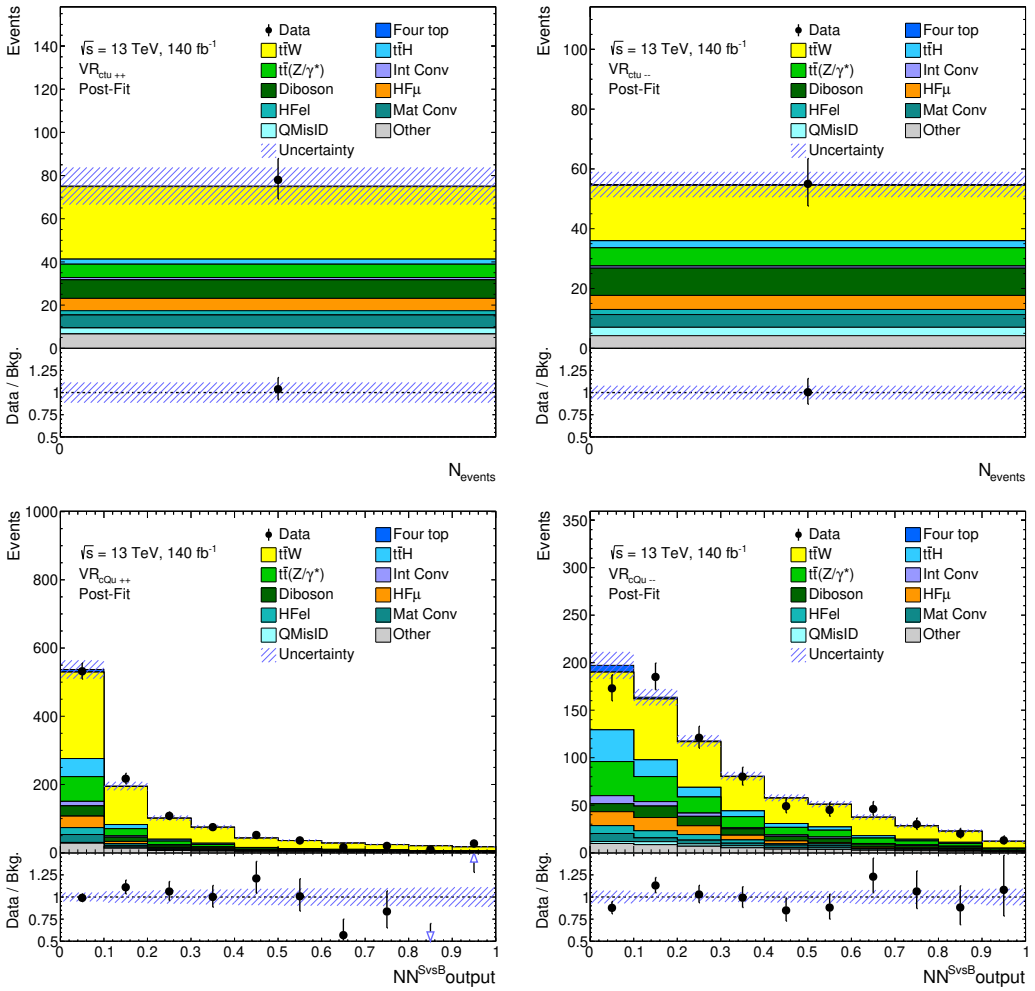

Figure B.1: Distributions of the $\mathrm{NN^{SvsB}}$ output for data and the expected background after the background-only fit. The post-fit background expectations are shown as filled histograms, the combined pre-fit background expectations are shown as dashed lines. The ratio of the data to the total post-fit background is shown in the lower panel. The combined statistical and systematic uncertainty in MC simulation is indicated by the hatched band, while the vertical error bars represent the statistical uncertainty in the data.

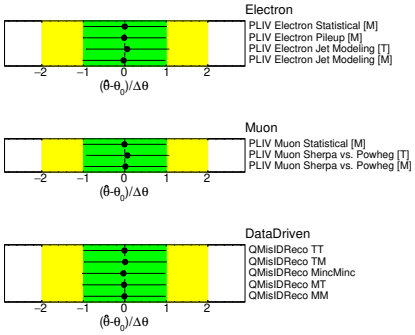

Figure B.2: Pulls and constraints on the electron (top), muon (middle), and data-driven (bottom) nuisance parameter for the background-only fit.

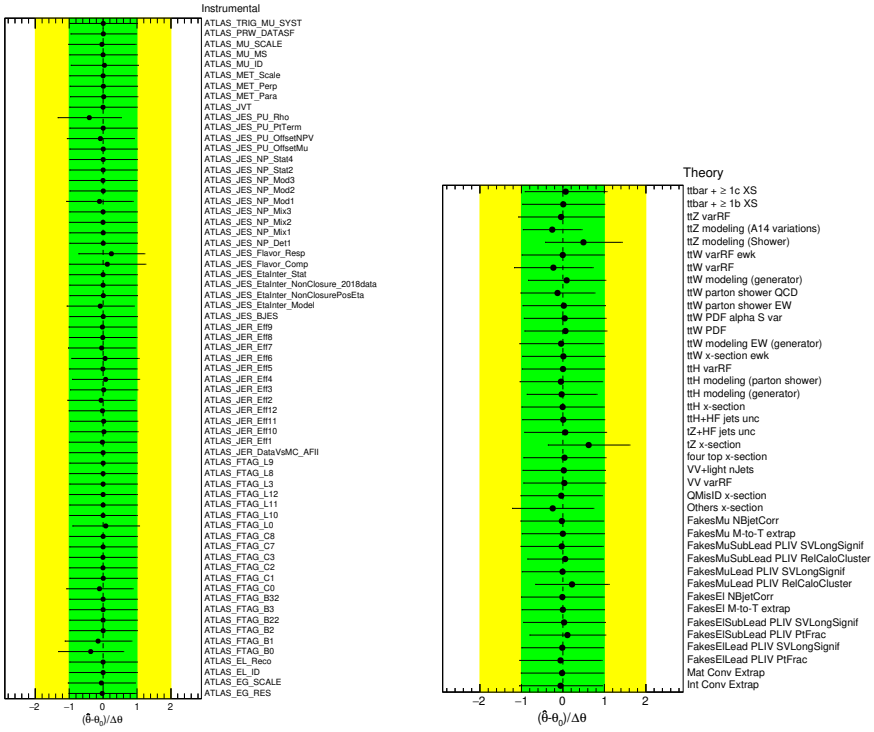

Figure B.3: Pulls and constraints on the instrumental (left) and theory (right) nuisance parameter for the background-only fit.

B.2 Hybrid-Asimov fit to all analysis regions

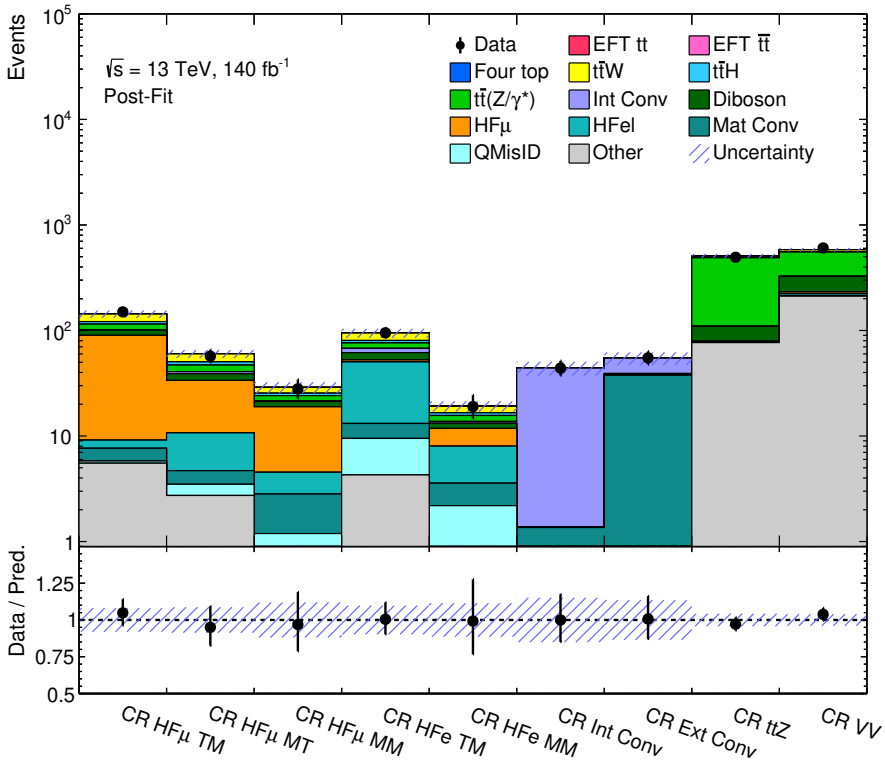

Figure B.4: Comparison between the event yields in data and the background expectation after the hybrid-Asimov fit for the nine CRs. The post-fit background expectations are shown as filled histograms, the combined pre-fit background expectations are shown as dashed lines. The ratio of the data to the total post-fit background is shown in the lower panel. The combined statistical and systematic uncertainty in the simulation is indicated by the hatched band, while the vertical error bars represent the statistical uncertainty in the data.

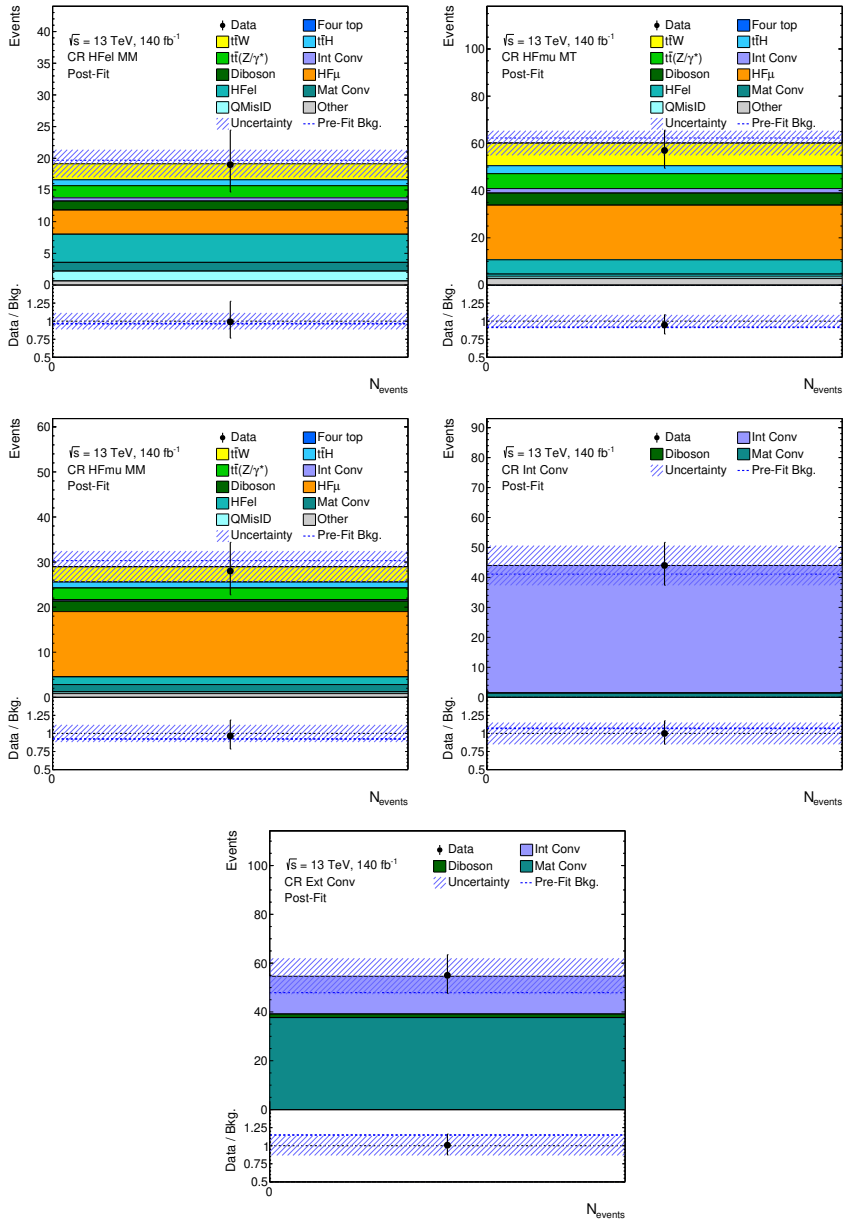

Figure B.5: Comparison between the event yields in data and the background prediction after the hybrid-Asimov fit for the five single-bin CRs. The ratio of the data to the total post-fit background is shown in the lower panel. The combined statistical and systematic uncertainty in the simulation is indicated by the hatched band, while the vertical error bars represent the statistical uncertainty in the data.

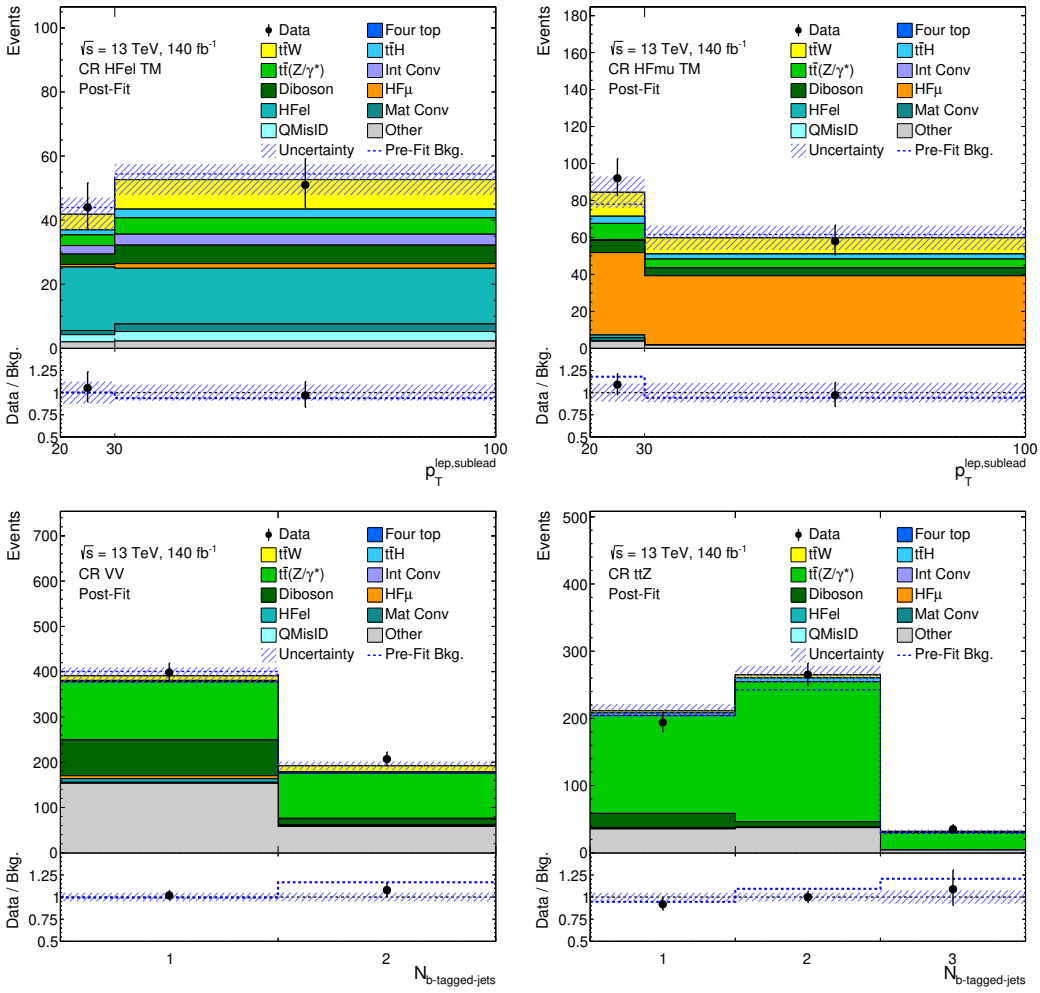

Figure B.6: Comparison between the event yields in data and the background prediction after the hybrid-Asimov fit for the four single-bin CRs. The ratio of the data to the total post-fit background is shown in the lower panel. The combined statistical and systematic uncertainty in the simulation is indicated by the hatched band, while the vertical error bars represent the statistical uncertainty in the data.

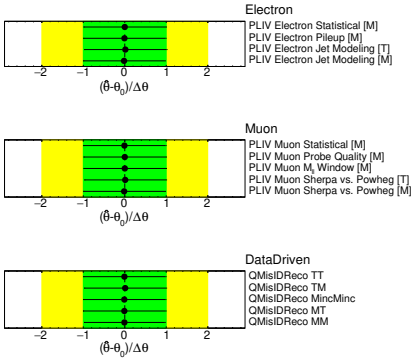

Figure B.7: Pulls and constraints on the electron (top), muon (middle), and data-driven (bottom) nuisance parameter for the hybrid-Asimov fit.

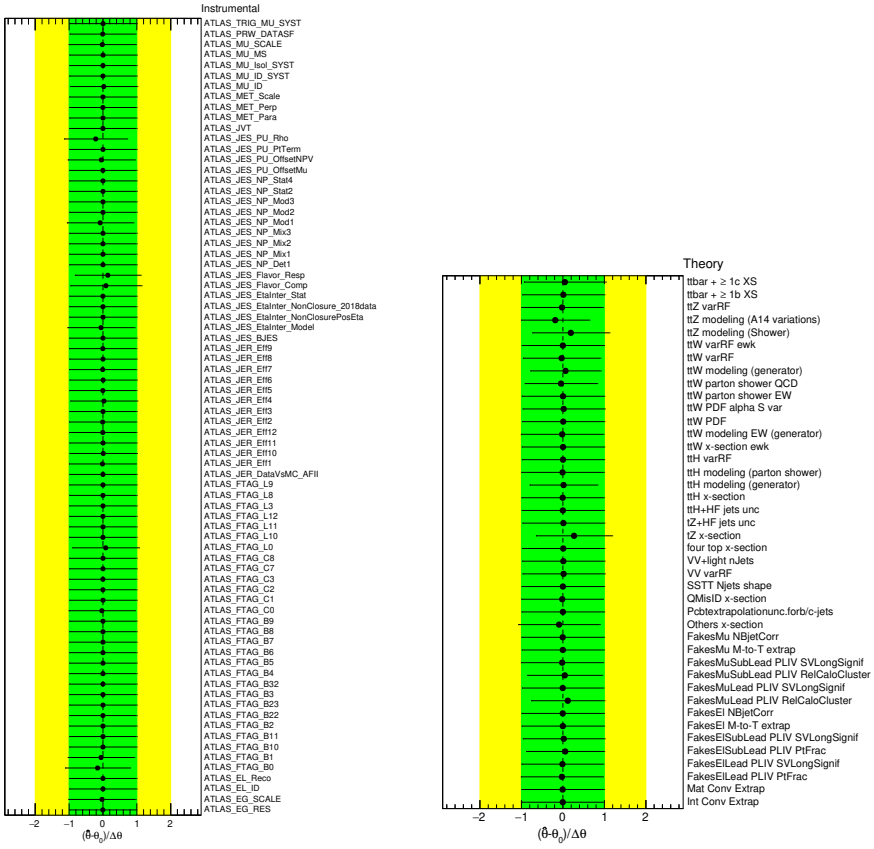

Figure B.8: Pulls and constraints on the instrumental (left) and theory (right) nuisance parameter for the hybrid-Asimov fit.

B.3 Data fit to all analysis regions

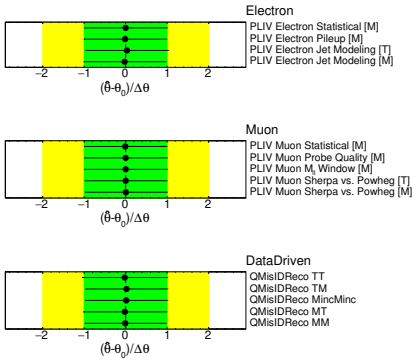

Figure B.9: Pulls and constraints on the electron (top), muon (middle), and data-driven (bottom) nuisance parameter for the data fit.

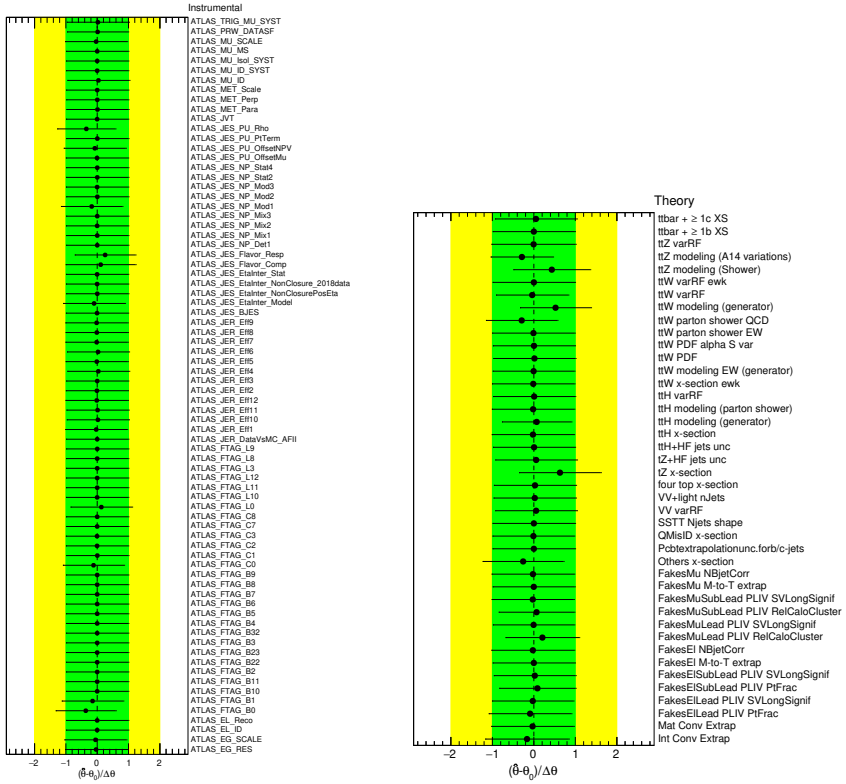

Figure B.10: Pulls and constraints on the instrumental (left) and theory (right) nuisance parameter for the data fit.

C Details on the check for Wilks' Theorem

In this appendix chapter, additional information and plots for the check of Wilks' Theorem is presented. As presented in the results chapter, the quadratic EFT terms in this analysis violate Wilks' Theorem. Hence, the coverage for the derived CIs in this analysis is not guaranteed to be as expected. Therefore, the coverage of the CIs is checked using toy experiments generated around the best-fit values of the Wilson coefficients. For each toy experiment, the likelihood is scanned for different WC values, to determine the CIs. Then each toy experiment is checked, if the CI contains the true WC value that was used for the generation of the pseudo-data. Once this is done for all toy experiments, the coverage is calculated as the fraction of toy experiments where the true WC value is contained in the CI. Following this procedure for each of the three WCs separately with their observed limit at 95% CL as the true value, it was checked how valid the results of this analysis are.

For all three WCs overcoverage is observed. In detail, the coverage for the CIs at 95% CL is found to be 96.48%, 97.39%, and 97.78% for $c_{tu}^{(1)}$, $c_{Qu}^{(1)}$, and $c_{Qu}^{(8)}$, respectively. For generation of toy experiments for each of these coverage checks, two WCs are set to zero and the third one is set to the observed limit value at 95% CL. In detail, the following values were used as true values for the WCs: $c_{tu}^{(1)} = 0.0068$, $c_{Qu}^{(1)} = 0.020$, and $c_{Qu}^{(8)} = 0.040$. By using true values which are very close to the observed limits, the coverage is checked in the region where the approximation is valid. In Figure C.1 the likelihood scans are for the hybrid-Asimov fit and data fit, but with the uncorrected and corrected 2σ lines. The corrected 2σ lines are derived, by shifting down the line until the coverage agrees with the expected coverage of 95%. Due to the 2σ lines only being valid exactly around the injected WCs value, it loses its validity when moving away from the injected value. Hence, the corrected 2σ lines are only plotted in the range where the approximation is expected to be valid.

However, it is possible to derive a corrected sigma line that is valid for the full range of scanned WCs values, by repeating running toy experiments for different injected WCs values. This has to be done in small steps to ensure validity in the full range of WC values. An example plot using such corrected σ lines from an ATLAS analysis is shown in Figure C.2.

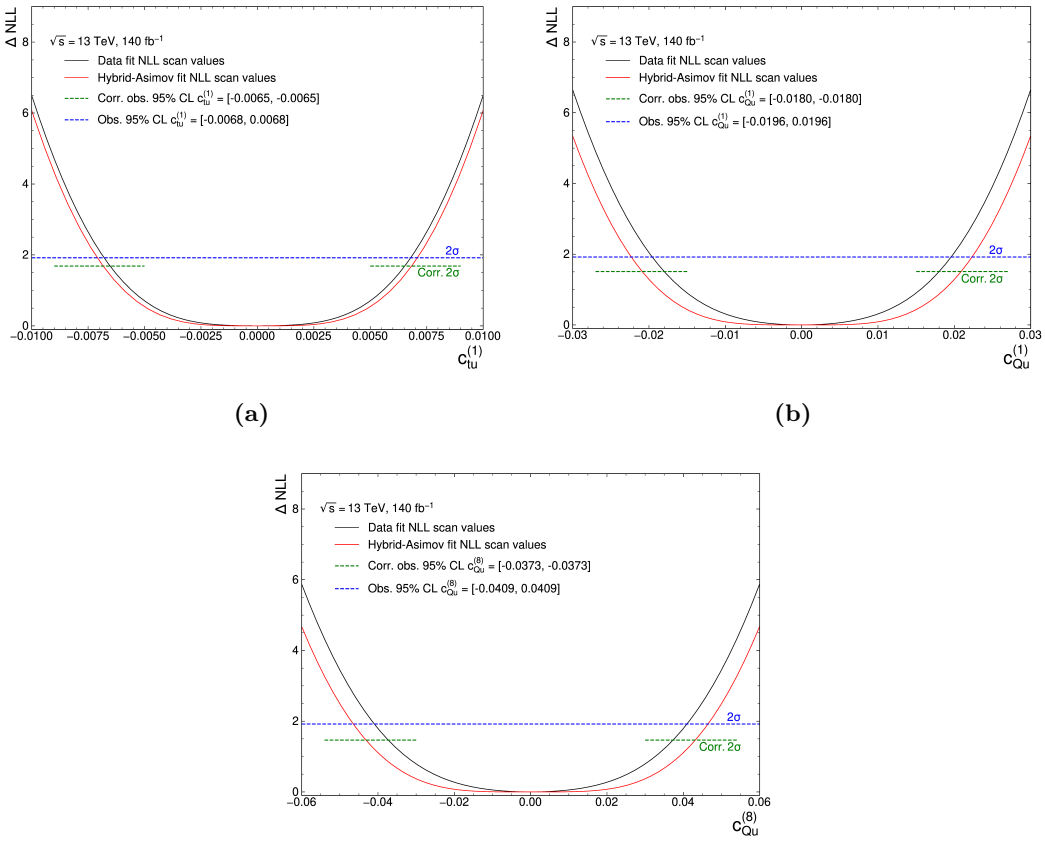

Figure C.1: Limits for the three different Wilson coefficients: (a) $c_{tu}^{(1)}$, (b) $c_{Qu}^{(1)}$, and (c) $c_{Qu}^{(8)}$. The corrected and uncorrected observed and expected limits at 95% confidence level (CL) can be read off by finding the intersection of the likelihood scan curve with the corrected or uncorrected 2σ line. The observed limits are shown numerically in the respective legend. The new-physics scale is set to $\Lambda = 1\,\text{TeV}$. The corrected 2σ line is found by using toy experiments and shifting the line until the expected coverage in the toy experiments is reached. It should be noted that the corrected sigma lines are only valid around the WC value that was used for the generation of the toy experiments, which are the uncorrected observed limits. To indicate the range of validity, the corrected sigma lines are only plotted in the range where the approximation is valid.

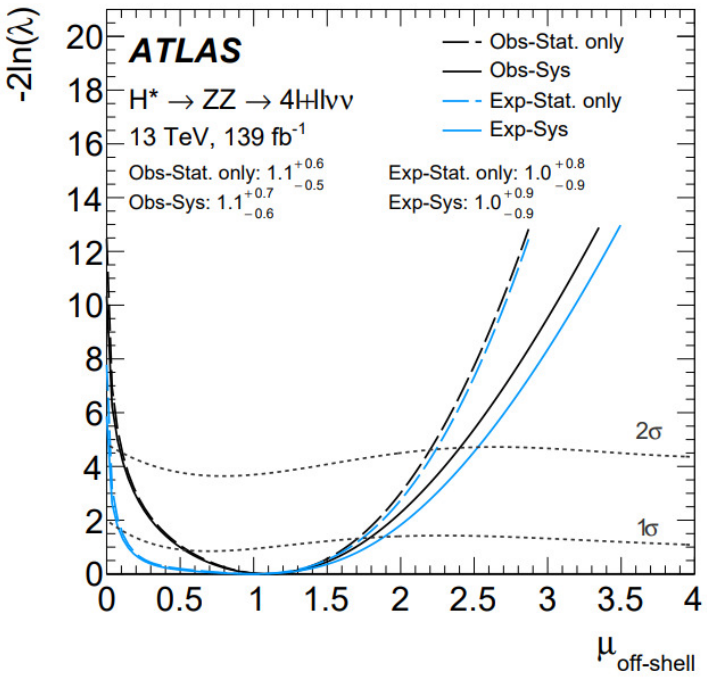

Figure C.2: Example plot from the ATLAS search for off-shell Higgs boson production for a fully corrected 2σ line.

Bibliography

[1] ATLAS Collaboration, *Search for same-charge top-quark pair production in pp collisions at $\sqrt{s} = 13$ TeV with the ATLAS detector*, JHEP **02** (2025) 84, All figures including auxiliary figures are available at https://atlas.web.cern.ch/Atlas/GROUPS/PHYSICS/PAPERS/TOPQ-2021-14/, arXiv: 2409.14982 [hep-ex].

[2] D. Galbraith and C. Burgard, *Diagram of the current standard model of physics*, Accessed: 04 December 2024, 2012, URL: https://texample.net//tikz/examples/model-physics/.

[3] E. Noether, *Invariant variation problems*, Transport Theory and Statistical Physics **1** (1971) 186.

[4] S. Weinberg, *A Model of Leptons*, Phys. Rev. Lett. **19** (21 1967) 1264.

[5] A. Salam, *Weak and Electromagnetic Interactions*, Conf. Proc. C **680519** (1968) 367.

[6] S. L. Glashow, *Partial-symmetries of weak interactions*, Nuclear Physics **22** (1961) 579.

[7] N. Cabibbo, *Unitary Symmetry and Leptonic Decays*, Phys. Rev. Lett. **10** (12 1963) 531.

[8] M. Kobayashi and T. Maskawa, *CP-Violation in the Renormalizable Theory of Weak Interaction*, Progress of Theoretical Physics **49** (1973) 652.

[9] P. W. Higgs, *Broken Symmetries and the Masses of Gauge Bosons*, Phys. Rev. Lett. **13** (16 1964) 508.

[10] F. Englert and R. Brout, *Broken Symmetry and the Mass of Gauge Vector Mesons*, Phys. Rev. Lett. **13** (9 1964) 321.

[11] CMS Collaboration, *Observation of a new boson at a mass of 125 GeV with the CMS experiment at the LHC*, Phys. Lett. B **716** (2012) 30, arXiv: 1207.7235 [hep-ex].

[12] ATLAS Collaboration, *Observation of a new particle in the search for the Standard Model Higgs boson with the ATLAS detector at the LHC*, Phys. Lett. B **716** (2012) 1, arXiv: 1207.7214 [hep-ex].

[13] CDF Collaboration, *Observation of Top Quark Production in $\overline{p}p$ Collisions with the Collider Detector at Fermilab*, Phys. Rev. Lett. **74** (14 1995) 2626, arXiv: hep-ex/9503002 [hep-ex].

[14] D0 Collaboration, *Observation of the Top Quark*,
Phys. Rev. Lett. **74** (14 1995) 2632, arXiv: hep-ex/9503003 [hep-ex].

[15] Particle Data Group, *Review of Particle Physics*,
Phys. Rev. D **110** (3 2024) 030001.

[16] J. A. Aguilar-Saavedra, *Toponium Hunter's Guide*,
arXiv: 2407.20330 [hep-ph].

[17] ATLAS Collaboration,
Top cross section summary plots - April 2024, ATL-PHYS-PUB-2024-006,
URL: https://cds.cern.ch/record/2896104.

[18] S. L. Glashow, J. Iliopoulos, and L. Maiani,
Weak Interactions with Lepton-Hadron Symmetry,
Phys. Rev. D **2** (7 1970) 1285.

[19] L. Canetti, M. Drewes, and M. Shaposhnikov,
Matter and antimatter in the universe,
New Journal of Physics **14** (2012) 095012, arXiv: 1204.4186 [hep-ph].

[20] A. D. Sakharov, *Violation of CP Invariance, C asymmetry, and baryon asymmetry of the universe*, Pisma Zh. Eksp. Teor. Fiz. **5** (1967) 32.

[21] R. D. Peccei, "The Strong CP Problem and Axions,"
In: "Axions: Theory, Cosmology, and Experimental Searches,"
Springer Berlin Heidelberg, 2008 3, ISBN: 9783540735182.

[22] G. Bertone, D. Hooper, and J. Silk,
Particle dark matter: evidence, candidates and constraints,
Physics Reports **405** (2005) 279.

[23] F. Zwicky, *Die Rotverschiebung von extragalaktischen Nebeln*,
Helv. Phys. Acta **6** (1933) 110.

[24] P. Minkowski, $\mu \to e\gamma$ *at a rate of one out of* 10^9 *muon decays?*
Physics Letters B **67** (1977) 421.

[25] E. Fermi, *Versuch einer Theorie der β-Strahlen. 1*, Z. Phys. **88** (1934) 161.

[26] B. Grzadkowski, M. Iskrzyński, M. Misiak, and J. Rosiek,
Dimension-six terms in the Standard Model Lagrangian, JHEP **10** (2010) 85,
arXiv: 1008.4884 [hep-ph].

[27] V. Hirschi and O. Mattelaer,
Automated event generation for loop-induced processes,
arXiv: 1507.00020 [hep-ph].

[28] C. Degrande, J.-M. Gérard, C. Grojean, F. Maltoni, and G. Servant,
An effective approach to same sign top pair production at the LHC and the forward–backward asymmetry at the Tevatron, Phys. Lett. **703** (2011) 306,
arXiv: 1104.1798 [hep-ph].

[29] UTfit Collaboration, *Model-independent constraints on Delta F=2 operators and the scale of New Physics*, JHEP **03** (2008) 049, arXiv: 0707.0636 [hep-ph].

[30] ATLAS Collaboration, *Analysis of events with b-jets and a pair of leptons of the same charge in pp collisions at $\sqrt{s} = 8$ TeV with the ATLAS detector*, JHEP **10** (2015) 150, arXiv: 1504.04605 [hep-ex].

[31] ATLAS Collaboration, *Search for same-charge top-quark pair production in pp collisions at $\sqrt{s} = 13$ TeV with the ATLAS detector (Version 1)*, 2024, URL: https://doi.org/10.17182/hepdata.155341.v1.

[32] ATLAS Collaboration, *Top EFT summary plots April 2024*, ATL-PHYS-PUB-2024-004, URL: https://cds.cern.ch/record/2896020.

[33] I. Brivio et al., *O new physics, where art thou? A global search in the top sector*, JHEP **02** (2020) 131, arXiv: 1910.03606 [hep-ph].

[34] J. J. Ethier et al., *Combined SMEFT interpretation of Higgs, diboson, and top quark data from the LHC*, JHEP **11** (2021) 089, arXiv: 2105.00006 [hep-ph].

[35] L. Evans and P. Bryant, *LHC Machine*, JINST **3** (2008) S08001.

[36] ATLAS Collaboration, *The ATLAS Experiment at the CERN Large Hadron Collider*, JINST **3** (2008) S08003.

[37] CMS Collaboration, *The CMS experiment at the CERN LHC*, JINST **3** (2008) S08004.

[38] ALICE Collaboration, *The ALICE experiment at the CERN LHC*, JINST **3** (2008) S08002.

[39] LHCb Collaboration, *The LHCb Detector at the LHC*, JINST **3** (2008) S08005.

[40] ATLAS Collaboration, *Peak luminosity per fill*, 2018, URL: https://atlas.web.cern.ch/Atlas/GROUPS/DATAPREPARATION/PublicPlots/2018/DataSummary/figs/peakLumiByFill.pdf.

[41] ATLAS Collaboration, *The ATLAS experiment at the CERN Large Hadron Collider: a description of the detector configuration for Run 3*, JINST **19** (2023) P05063, arXiv: 2305.16623 [physics.ins-det].

[42] ATLAS Collaboration, *ATLAS Insertable B-Layer: Technical Design Report*, CERN-LHCC-2010-013, ATLAS-TDR-19, URL: https://cds.cern.ch/record/1291633.

[43] B. Abbott et al.,
Production and integration of the ATLAS Insertable B-Layer,
JINST **13** (2018) T05008, arXiv: 1803.00844 [physics.ins-det].

[44] ATLAS Collaboration, *Performance of the ATLAS trigger system in 2015*,
Eur. Phys. J. C **77** (2017) 317, arXiv: 1611.09661 [hep-ex].

[45] ATLAS Collaboration, *Luminosity determination in pp collisions at $\sqrt{s} = 13$ TeV using the ATLAS detector at the LHC*,
Eur. Phys. J. C **83** (2023) 982, arXiv: 2212.09379 [hep-ex].

[46] ATLAS Collaboration, *The ATLAS Simulation Infrastructure*,
Eur. Phys. J. C **70** (2010) 823, arXiv: 1005.4568 [physics.ins-det].

[47] S. Agostinelli et al., *GEANT4 – a simulation toolkit*,
Nucl. Instrum. Meth. A **506** (2003) 250.

[48] ATLAS Collaboration,
The new Fast Calorimeter Simulation in ATLAS, ATL-SOFT-PUB-2018-002,
URL: https://cds.cern.ch/record/2630434.

[49] T. Sjöstrand, S. Mrenna, and P. Skands, *A brief introduction to PYTHIA 8.1*,
Comput. Phys. Commun. **178** (2008) 852, arXiv: 0710.3820 [hep-ph].

[50] NNPDF Collaboration, R. D. Ball, et al., *Parton distributions with LHC data*,
Nucl. Phys. B **867** (2013) 244, arXiv: 1207.1303 [hep-ph].

[51] ATLAS Collaboration, *The Pythia 8 A3 tune description of ATLAS minimum bias and inelastic measurements incorporating the Donnachie-Landshoff diffractive model*, ATL-PHYS-PUB-2016-017,
URL: https://cds.cern.ch/record/2206965.

[52] D. J. Lange, *The EvtGen particle decay simulation package*,
Nucl. Instrum. Meth. A **462** (2001) 152.

[53] J. Alwall et al.,
The automated computation of tree-level and next-to-leading order differential cross sections, and their matching to parton shower simulations,
JHEP **07** (2014) 079, arXiv: 1405.0301 [hep-ph].

[54] S. Frixione, G. Ridolfi, and P. Nason, *A positive-weight next-to-leading-order Monte Carlo for heavy flavour hadroproduction*, JHEP **09** (2007) 126,
arXiv: 0707.3088 [hep-ph].

[55] E. Re, *Single-top Wt-channel production matched with parton showers using the POWHEG method*, Eur. Phys. J. C **71** (2011) 1547,
arXiv: 1009.2450 [hep-ph].

[56] S. Alioli, P. Nason, C. Oleari, and E. Re, *NLO single-top production matched with shower in POWHEG: s− and t−channel contributions*,
JHEP **09** (2009) 111, arXiv: 0907.4076 [hep-ph].

[57] T. Sjöstrand et al., *An introduction to PYTHIA 8.2*, Comput. Phys. Commun. **191** (2015) 159, arXiv: 1410.3012 [hep-ph].

[58] ATLAS Collaboration, *ATLAS Pythia 8 tunes to 7 TeV data*, ATL-PHYS-PUB-2014-021, URL: https://cds.cern.ch/record/1966419.

[59] M. Bähr et al., *Herwig++ physics and manual*, Eur. Phys. J. C **58** (2008) 639, arXiv: 0803.0883 [hep-ph].

[60] J. Bellm et al., *Herwig 7.0/Herwig++ 3.0 release note*, Eur. Phys. J. C **76** (2016) 196, arXiv: 1512.01178 [hep-ph].

[61] L. A. Harland-Lang, A. D. Martin, P. Motylinski, and R. S. Thorne, *Parton distributions in the LHC era: MMHT 2014 PDFs*, Eur. Phys. J. C **75** (2015) 204, arXiv: 1412.3989 [hep-ph].

[62] E. Bothmann et al., *Event generation with Sherpa 2.2*, SciPost Phys. **7** (2019) 034, arXiv: 1905.09127 [hep-ph].

[63] I. Brivio, Y. Jiang, and M. Trott, *The SMEFTsim package, theory and tools*, JHEP **12** (2017) 070, arXiv: 1709.06492 [hep-ph].

[64] I. Brivio, *SMEFTsim 3.0 — a practical guide*, JHEP **04** (2021) 073, arXiv: 2012.11343 [hep-ph].

[65] A. Alloul, N. D. Christensen, C. Degrande, C. Duhr, and B. Fuks, *FeynRules 2.0 — A complete toolbox for tree-level phenomenology*, Comput. Phys. Commun. **185** (2014) 2250, arXiv: 1310.1921 [hep-ph].

[66] R. D. Ball et al., *Parton distributions for the LHC run II*, JHEP **04** (2015) 040, arXiv: 1410.8849 [hep-ph].

[67] O. Mattelaer, *On the maximal use of Monte Carlo samples: re-weighting events at NLO accuracy*, Eur. Phys. J. C **76** (2016), arXiv: 1607.00763 [hep-ph].

[68] P. Artoisenet, V. Lemaître, F. Maltoni, and O. Mattelaer, *Automation of the matrix element reweighting method*, JHEP **2010** (2010), arXiv: 1007.3300 [hep-ph].

[69] ATLAS Collaboration, *Measurement of the total and differential cross-sections of $t\bar{t}W$ production in pp collisions at $\sqrt{s} = 13$ TeV with the ATLAS detector*, JHEP **05** (2024) 131, arXiv: 2401.05299 [hep-ex].

[70] T. Gleisberg and S. Höche, *Comix, a new matrix element generator*, JHEP **12** (2008) 039, arXiv: 0808.3674 [hep-ph].

[71] S. Schumann and F. Krauss, *A parton shower algorithm based on Catani–Seymour dipole factorisation*, JHEP **03** (2008) 038, arXiv: 0709.1027 [hep-ph].

[72] S. Höche, F. Krauss, M. Schönherr, and F. Siegert, *A critical appraisal of NLO+PS matching methods*, JHEP **09** (2012) 049, arXiv: 1111.1220 [hep-ph].

[73] S. Höche, F. Krauss, M. Schönherr, and F. Siegert, *QCD matrix elements + parton showers. The NLO case*, JHEP **04** (2013) 027, arXiv: 1207.5030 [hep-ph].

[74] S. Catani, F. Krauss, B. R. Webber, and R. Kuhn, *QCD Matrix Elements + Parton Showers*, JHEP **11** (2001) 063, arXiv: hep-ph/0109231 [hep-ph].

[75] S. Höche, F. Krauss, S. Schumann, and F. Siegert, *QCD matrix elements and truncated showers*, JHEP **05** (2009) 053, arXiv: 0903.1219 [hep-ph].

[76] F. Buccioni et al., *OpenLoops 2*, Eur. Phys. J. C **79** (2019) 866, arXiv: 1907.13071 [hep-ph].

[77] F. Cascioli, P. Maierhöfer, and S. Pozzorini, *Scattering Amplitudes with Open Loops*, Phys. Rev. Lett. **108** (2012) 111601, arXiv: 1111.5206 [hep-ph].

[78] A. Denner, S. Dittmaier, and L. Hofer, *Collier: A fortran-based complex one-loop library in extended regularizations*, Comput. Phys. Commun. **212** (2017) 220, arXiv: 1604.06792 [hep-ph].

[79] R. Frederix and I. Tsinikos, *On improving NLO merging for $t\bar{t}W$ production*, JHEP **11** (2021) 029, arXiv: 2108.07826 [hep-ph].

[80] D. de Florian et al., *Handbook of LHC Higgs Cross Sections: 4. Deciphering the Nature of the Higgs Sector*, (2017), arXiv: 1610.07922 [hep-ph].

[81] P. Nason, *A new method for combining NLO QCD with shower Monte Carlo algorithms*, JHEP **11** (2004) 040, arXiv: hep-ph/0409146 [hep-ph].

[82] S. Frixione, P. Nason, and C. Oleari, *Matching NLO QCD computations with parton shower simulations: the POWHEG method*, JHEP **11** (2007) 070, arXiv: 0709.2092 [hep-ph].

[83] S. Alioli, P. Nason, C. Oleari, and E. Re, *A general framework for implementing NLO calculations in shower Monte Carlo programs: the POWHEG BOX*, JHEP **06** (2010) 043, arXiv: 1002.2581 [hep-ph].

[84] H. B. Hartanto, B. Jäger, L. Reina, and D. Wackeroth, *Higgs boson production in association with top quarks in the POWHEG BOX*, Phys. Rev. D **91** (2015) 094003, arXiv: 1501.04498 [hep-ph].

[85] M. Beneke, P. Falgari, S. Klein, and C. Schwinn,
Hadronic top-quark pair production with NNLL threshold resummation,
Nucl. Phys. B **855** (2012) 695, arXiv: 1109.1536 [hep-ph].

[86] M. Cacciari, M. Czakon, M. Mangano, A. Mitov, and P. Nason,
Top-pair production at hadron colliders with next-to-next-to-leading logarithmic soft-gluon resummation, Phys. Lett. B **710** (2012) 612,
arXiv: 1111.5869 [hep-ph].

[87] P. Bärnreuther, M. Czakon, and A. Mitov,
Percent-Level-Precision Physics at the Tevatron: Next-to-Next-to-Leading Order QCD Corrections to $q\bar{q} \to t\bar{t} + X$, Phys. Rev. Lett. **109** (2012) 132001,
arXiv: 1204.5201 [hep-ph].

[88] M. Czakon and A. Mitov, *NNLO corrections to top-pair production at hadron colliders: the all-fermionic scattering channels*, JHEP **12** (2012) 054,
arXiv: 1207.0236 [hep-ph].

[89] M. Czakon and A. Mitov, *NNLO corrections to top pair production at hadron colliders: the quark-gluon reaction*, JHEP **01** (2013) 080,
arXiv: 1210.6832 [hep-ph].

[90] M. Czakon, P. Fiedler, and A. Mitov, *Total Top-Quark Pair-Production Cross Section at Hadron Colliders Through $\mathcal{O}(\alpha_S^4)$*,
Phys. Rev. Lett. **110** (2013) 252004, arXiv: 1303.6254 [hep-ph].

[91] M. Czakon and A. Mitov, *Top++: A program for the calculation of the top-pair cross-section at hadron colliders*,
Comput. Phys. Commun. **185** (2014) 2930, arXiv: 1112.5675 [hep-ph].

[92] ATLAS Collaboration, *Studies on top-quark Monte Carlo modelling for Top2016*, ATL-PHYS-PUB-2016-020,
URL: https://cds.cern.ch/record/2216168.

[93] S. Frixione, E. Laenen, P. Motylinski, C. White, and B. R. Webber,
Single-top hadroproduction in association with a W boson,
JHEP **07** (2008) 029, arXiv: 0805.3067 [hep-ph].

[94] N. Kidonakis, *Two-loop soft anomalous dimensions for single top quark associated production with a W^- or H^-*, Phys. Rev. D **82** (2010) 054018,
arXiv: 1005.4451 [hep-ph].

[95] M. Aliev et al.,
HATHOR – HAdronic Top and Heavy quarks crOss section calculatoR,
Comput. Phys. Commun. **182** (2011) 1034, arXiv: 1007.1327 [hep-ph].

[96] P. Kant et al.,
HatHor for single top-quark production: Updated predictions and uncertainty estimates for single top-quark production in hadronic collisions,
Comput. Phys. Commun. **191** (2015) 74, arXiv: 1406.4403 [hep-ph].

[97] ATLAS Collaboration, *Measurement of the Z/γ^* boson transverse momentum distribution in pp collisions at $\sqrt{s} = 7$ TeV with the ATLAS detector*, JHEP **09** (2014) 145, arXiv: 1406.3660 [hep-ex].

[98] ATLAS Collaboration, *Performance of the ATLAS muon triggers in Run 2*, JINST **15** (2020) P09015, arXiv: 2004.13447 [physics.ins-det].

[99] ATLAS Collaboration, *Performance of electron and photon triggers in ATLAS during LHC Run 2*, Eur. Phys. J. C **80** (2020) 47, arXiv: 1909.00761 [hep-ex].

[100] ATLAS Collaboration, *Vertex Reconstruction Performance of the ATLAS Detector at $\sqrt{s} = 13$ TeV*, ATL-PHYS-PUB-2015-026, URL: https://cds.cern.ch/record/2037717.

[101] ATLAS Collaboration, *Electron and photon performance measurements with the ATLAS detector using the 2015–2017 LHC proton–proton collision data*, JINST **14** (2019) P12006, arXiv: 1908.00005 [hep-ex].

[102] ATLAS Collaboration, *Muon reconstruction and identification efficiency in ATLAS using the full Run 2 pp collision data set at $\sqrt{s} = 13$ TeV*, Eur. Phys. J. C **81** (2021) 578, arXiv: 2012.00578 [hep-ex].

[103] ATLAS Collaboration, *Evidence for the associated production of the Higgs boson and a top quark pair with the ATLAS detector*, Phys. Rev. D **97** (2018) 072003, arXiv: 1712.08891 [hep-ex].

[104] ATLAS Collaboration, *Jet reconstruction and performance using particle flow with the ATLAS Detector*, Eur. Phys. J. C **77** (2017) 466, arXiv: 1703.10485 [hep-ex].

[105] M. Cacciari, G. P. Salam, and G. Soyez, *The anti-k_t jet clustering algorithm*, JHEP **04** (2008) 063, arXiv: 0802.1189 [hep-ph].

[106] M. Cacciari, G. P. Salam, and G. Soyez, *FastJet user manual*, Eur. Phys. J. C **72** (2012) 1896, arXiv: 1111.6097 [hep-ph].

[107] ATLAS Collaboration, *Jet energy scale and resolution measured in proton–proton collisions at $\sqrt{s} = 13$ TeV with the ATLAS detector*, Eur. Phys. J. C **81** (2021) 689, arXiv: 2007.02645 [hep-ex].

[108] ATLAS Collaboration, *The performance of missing transverse momentum reconstruction and its significance with the ATLAS detector using 140 fb^{-1} of $\sqrt{s} = 13$ TeV pp collisions*, (2024), arXiv: 2402.05858 [hep-ex].

[109] ATLAS Collaboration, *ATLAS flavour-tagging algorithms for the LHC Run 2 pp collision dataset*, Eur. Phys. J. C **83** (2023) 681, arXiv: 2211.16345 [physics.data-an].

[110] ATLAS Collaboration, *Search for new phenomena with top quark pairs in final states with one lepton, jets, and missing transverse momentum in pp collisions at $\sqrt{s} = 13$ TeV with the ATLAS detector*, JHEP **04** (2021) 174, arXiv: 2012.03799 [hep-ex].

[111] F. Chollet et al., *Keras*, 2015, URL: https://keras.io.

[112] *TensorFlow: Large-Scale Machine Learning on Heterogeneous Systems*, Software available from tensorflow.org.

[113] V. Nair and G. E. Hinton,
"Rectified linear units improve restricted boltzmann machines,"
In: "Proceedings of the 27th International Conference on International Conference on Machine Learning," Omnipress, 2010 807,
ISBN: 9781605589077.

[114] D. E. Rumelhart, G. E. Hinton, and R. J. Williams,
Learning representations by back-propagating errors, Nature **323** (1986) 533.

[115] D. P. Kingma and J. Ba, *Adam: A Method for Stochastic Optimization*, 2017, arXiv: 1412.6980 [cs.LG].

[116] A. Y. Ng,
"Feature selection, L1 vs. L2 regularization, and rotational invariance,"
In: "Proceedings of the 21th International Conference on Machine Learning,"
Association for Computing Machinery, 2004 78, ISBN: 1581138385.

[117] F. Pedregosa et al., *Scikit-learn: Machine Learning in Python*, (2018), arXiv: 1201.0490 [cs.LG].

[118] A. Altmann, L. Toloşi, O. Sander, and T. Lengauer,
Permutation importance: a corrected feature importance measure,
Bioinformatics **26** (2010) 1340.

[119] ATLAS Collaboration,
Search for heavy Higgs bosons with flavour-violating couplings in multi-lepton plus b-jets final states in pp collisions at 13 TeV with the ATLAS detector,
JHEP **12** (2023) 081, arXiv: 2307.14759 [hep-ex].

[120] W. Verkerke and D. Kirkby, *The RooFit toolkit for data modeling*, (2003), arXiv: physics/0306116 [physics.data-an].

[121] ROOT Collaboration, *HistFactory: A tool for creating statistical models for use with RooFit and RooStats*, CERN-OPEN-2012-016 (2012).

[122] G. Cowan, K. Cranmer, E. Gross, and O. Vitells,
Asymptotic formulae for likelihood-based tests of new physics,
The European Physical Journal C **71** (2011), arXiv: 1007.1727 [hep-ph].

[123] G. Avoni et al., *The new LUCID-2 detector for luminosity measurement and monitoring in ATLAS*, JINST **13** (2018) P07017.

[124] ATLAS Collaboration, *Measurement of the Inelastic Proton–Proton Cross Section at $\sqrt{s} = 13$ TeV with the ATLAS Detector at the LHC*, Phys. Rev. Lett. **117** (2016) 182002, arXiv: 1606.02625 [hep-ex].

[125] ATLAS Collaboration, *Studies of the muon momentum calibration and performance of the ATLAS detector with pp collisions at $\sqrt{s} = 13$ TeV*, Eur. Phys. J. C **83** (2023) 686, arXiv: 2212.07338 [hep-ex].

[126] ATLAS Collaboration, *Electron and photon efficiencies in LHC Run 2 with the ATLAS experiment*, JHEP **05** (2024) 162, arXiv: 2308.13362 [hep-ex].

[127] ATLAS Collaboration, *Performance of pile-up mitigation techniques for jets in pp collisions at $\sqrt{s} = 8$ TeV using the ATLAS detector*, Eur. Phys. J. C **76** (2016) 581, arXiv: 1510.03823 [hep-ex].

[128] ATLAS Collaboration, *ATLAS b-jet identification performance and efficiency measurement with $t\bar{t}$ events in pp collisions at $\sqrt{s} = 13$ TeV*, Eur. Phys. J. C **79** (2019) 970, arXiv: 1907.05120 [hep-ex].

[129] ATLAS Collaboration, *Measurement of the c-jet mistagging efficiency in $t\bar{t}$ events using pp collision data at $\sqrt{s} = 13$ TeV collected with the ATLAS detector*, Eur. Phys. J. C **82** (2022) 95, arXiv: 2109.10627 [hep-ex].

[130] ATLAS Collaboration, *Calibration of the light-flavour jet mistagging efficiency of the b-tagging algorithms with Z+jets events using 139 fb^{-1} of ATLAS proton–proton collision data at $\sqrt{s} = 13$ TeV*, Eur. Phys. J. C **83** (2023) 728, arXiv: 2301.06319 [hep-ex].

[131] M. K. F. Febres Cordero and L. Reina, *Top-quark pair production in association with a $W^{\pm}$ gauge boson in the POWHEG-BOX*, Phys. Rev. D **103** (2021) 094014, arXiv: 2101.11808 [hep-ph].

[132] R. Frederix, D. Pagani, and M. Zaro, *Large NLO corrections in $t\bar{t}W^{\pm}$ and $t\bar{t}t\bar{t}$ hadroproduction from supposedly subleading EW contributions*, JHEP **02** (2018) 031, arXiv: 1711.02116 [hep-ph].

[133] ATLAS Collaboration, *Observation of the associated production of a top quark and a Z boson in pp collisions at $\sqrt{s} = 13$ TeV with the ATLAS detector*, JHEP **07** (2020) 124, arXiv: 2002.07546 [hep-ex].

[134] ATLAS Collaboration, *Observation of four-top-quark production in the multilepton final state with the ATLAS detector*, Eur. Phys. J. C **83** (2023) 496, arXiv: 2303.15061 [hep-ex].

[135] S. Dulat et al., *New parton distribution functions from a global analysis of quantum chromodynamics*, Phys. Rev. D **93** (2016) 033006, arXiv: 1506.07443 [hep-ph].

[136] CMS Collaboration,
Measurement of the cross section of top quark-antiquark pair production in association with a W boson in proton-proton collisions at $\sqrt{s}$ = 13 TeV,
JHEP **07** (2023) 219, arXiv: 2208.06485 [hep-ex].

[137] L. Buonocore et al., *Precise Predictions for the Associated Production of a W Boson with a Top-Antitop Quark Pair at the LHC*,
Phys. Rev. Lett. **131** (23 2023) 231901, arXiv: 2306.16311 [hep-ph].

[138] S. S. Wilks, *The Large-Sample Distribution of the Likelihood Ratio for Testing Composite Hypotheses*,
The Annals of Mathematical Statistics **9** (1938) 60.

[139] F. U. Bernlochner, D. C. Fry, S. B. Menary, and E. Persson,
Cover your bases: asymptotic distributions of the profile likelihood ratio when constraining effective field theories in high-energy physics,
SciPost Phys. Core **6** (2023) 013, arXiv: 2207.01350 [physics.data-an].

Acknowledgements

What a journey it has been! I have met countless people, learned so much, and had the opportunity to conduct fundamental research in one of the most exciting fields of physics. In what follows, I would like to thank everyone who has supported me along the way.

Firstly, I would like to thank my supervisor, Prof. Dr. Kevin Kröninger, for giving me the opportunity to work on this project, for his continuous support, and for serving as the primary referee. Secondly, I would like to thank Prof. Dr. Maximilliano Sioli for welcoming me to Bologna with open arms and for handling all the bureaucratic matters on the Bologna side. Next, I would like to thank Prof. Dr. Angelo Carbone for serving as the second referee. Also, big thanks to our secretary, Andrea Teichmann, who takes care of all the administrative matters that I encountered during my time as a PhD student in an organized and efficient manner.

Furthermore, I would like to thank Dr. Andrea Helen Knue for her supervision and support. Her insightful discussions and constructive feedback were crucial to the success of the analysis team and helped smooth the rocky road to the publication of this work. I am truly grateful for the opportunity to work with you, and I appreciate that you were always available to help me, even though you had many other responsibilities as the ATLAS top convener.

However, this analysis would not have been possible without the rest of the analysis team. I would like to thank all of you for the excellent collaboration, engaging discussions, and support. Specifically, I would like to thank Noemi Cavalli and Nazlim Merve Agras for initiating this analysis and introducing me to all the technical details. Next, I would like to thank Matteo Negrini and Aurelio Juste for their invaluable support throughout the journey to publication. Finally, I would like to thank the newest member of the analysis team, Tomas Dado, for his technical assistance among the challenges of debugging and developing the code for the analysis. Beyond the analysis team, I would also like to thank the many other individuals who have supported me or contributed indirectly to this work as part of the ATLAS collaboration.

I would also like to thank all the members of AG Kröninger in Dortmund. Thank you, Benedikt, Lucas, Salvo, Michi, Nils, Lars, Christopher, Donna, and Carsten, for the wonderful times we shared. It was a pleasure working with all of you.

Although my family might not agree, they undoubtedly deserve credit for this achievement. I especially want to thank my father for guiding me toward physics when I was about to choose a different path. I never imagined that I would earn a PhD in particle physics, but I am extremely grateful that I did. Furthermore, I also

want to thank my mother for always being there for me, for supporting me in every decision, and for being the best mother one could wish for. Finally, I want to thank my siblings for their guidance and support as I grew up. I would never have become the ambitious person I am today without you. I am very grateful to have such a wonderful and loving family.

While many names have been mentioned, there are countless others who have supported me throughout my journey. I am extremely grateful to have two exceptional groups of friends: my childhood friends and my ever-thirsty *Stammtisch*. I am delighted to have you all in my life and look forward to many more years of friendship and incredible memories.

Last but not least, I want to thank my girlfriend, best friend, and future wife for her love, support, and understanding throughout my PhD. You were always there for me when I needed you, supporting me during my lowest moments, and celebrating my successes. I am deeply grateful to have you in my life, making this journey so much more enjoyable. I could not have done it without you, and I look forward to the next chapter of our lives together.